Form and Function in the Heart and Placenta: Quantitative Vascular MRI

By

Daniel P. Seiter

A dissertation submitted in partial fulfillment of
the requirements for the degree of

Doctor of Philosophy
(Medical Physics)

at the
UNIVERSITY OF WISCONSIN-MADISON
2023

Date of final oral examination: 05/31/2023

This dissertation is approved by the following members of the Final Oral Committee:

Oliver Wieben, Professor, Medical Physics
Kevin M. Johnson, Assistant Professor, Medical Physics
Diego Hernando, Assistant Professor, Medical Physics
Farhan Raza, Associate Professor, Medicine
Thaddeus G. Golos, Professor, Reproductive Sciences

For my parents, who laid the foundation of my education.

Acknowledgements

Graduate school is hard. Long hours, complicated experiments, and critical reviewers all contributed to the challenging but rewarding last 5 years of my life. The work presented in this dissertation would not have been possible without the support of many people, a few of whom I will recognize here. First, my thesis advisor Oliver, who was never too busy to ask how I was doing. While others may have discouraged extracurricular activities, he was always supportive and excited to hear about my experiences around Madison. Oliver set an example of "work hard, play hard", and always encouraged group outings to the terrace or retreats to his cabin. I would be a fraction of the scientist and person I am today without his guidance.

Second, my lab mates and collaborators, with whom I shared this incredible experience. Special thanks to Kelli Hellenbrand for her tireless work coordinating my MRI scans and supplying me with snacks over the years. When I visited graduate schools in 2018, Oliver's group stood above the rest as a friendly, collaborative environment. After joining, I saw firsthand that Wieben Lab is a unique collection of kind, motivated, and extremely talented individuals. Thank you all for being my most valued resource - past members Jacob MacDonald, who was always willing to chat about life, Phil Corrado, for teaching me so much about cardiovascular MRI, and Grant Roberts, who was always willing to brainstorm and rarely (if ever) did not know the answer to my technical questions. I would also like to thank the current members of the lab: Ruiming Chen, Alma Spahic, Tarun Naren, Ruo-Yu Liu, and Timothy Houston. Thank you all for your help, feedback, and friendship.

Third, my good friends in the Medical Physics department student body – too many to name, but so many brilliant and kind people with whom I've shared lunches, late nights, barbeques, and several wonderful holiday parties. I'd like to especially thank Victor Fernandes for being my

friend, confidant, and barber through the many ups and downs of the last five years. I'd also like to thank Joe Whitehead for his friendship from the very first day of the program, as well as his incredible creativity – I fondly remember long hours discussing your ideas. Thank you both for amazing memories and studying for the qualifier with me.

Fourth and finally, I owe a great deal of my success and happiness in life to the love and support of my family. I thank my parents, who gave me a love for learning and taught me the value of hard work. Finally, I can't thank my fiancée Sarah enough for her tireless encouragement, countless hours studying with me, and always being willing to discuss science and medicine.

Thank you.

Form and Function in the Heart and Placenta: Quantitative Vascular MRI

Daniel P. Seiter

Under the supervision of Professor Oliver Wieben

At the University of Wisconsin-Madison

Abstract

Magnetic Resonance Imaging (MRI) is a powerful diagnostic modality, able to capture both functional and anatomical data noninvasively. The aim of this dissertation was to develop and assess novel MRI methodology in acquisition, reconstruction, and post-processing to advance in-vivo assessment of disease in two regions of the body: 1) the placenta and 2) the heart.

1) The placenta plays a critical role in the development and long-term health of both fetus and mother; the ability to adequately quantify placental function in vivo, especially in early pregnancy could be a powerful tool for clinical decision making and therapeutic monitoring yet is currently not available. Ultrasound is commonly used in prenatal care, but its value to assess placental function is limited by a narrow field of view and poor contrast between uterus and placenta. Here, the value of dynamic contrast enhanced MRI for identifying underlying placental structures, quantifying their volumes and functional parameters associated with contrast bolus passage, and assessing their changes with pathology is demonstrated in a Rhesus Macaque model of zika virus, potentially laying the foundation for feasibility studies in humans. A promising alternative to flow associated functional analysis without the need for a contrast agent is velocity selective arterial spin labelling (VS-ASL) MRI; we present a large human study of normal and high body mass index (BMI) patients and report perfusion heterogeneity and trends that offer insight into placental development.

2) Heart disease is the leading cause of death in the United States. Imaging approaches that quantify changes in cardiovascular form and function can aid early detection and guide treatment and cardiovascular MRI plays an important role in clinical decision making. Heart failure with preserved ejection fraction (HFpEF) is a common disorder accounting for nearly half of all heart failure patients, and while cardiac function may appear normal, HFpEF often leads to secondary pulmonary hypertension (PH). PH leads to rising pressures in the pulmonary circulation and can lead to abnormal remodeling and right heart failure if left untreated. The current gold standard of HFpEF and PH diagnosis is invasive right heart catheterization which is associated with significant risk and discomfort for the patient, motivating a need for noninvasive evaluation of the effects of elevated pressure on the cardiopulmonary system. The potential value of 4D Flow MRI to quantify rising pressures in a swine model of PH is also discussed in this dissertation. The use of a flow compartment analysis to classify intra-ventricular flow patterns in the left and right ventricle in this novel swine model is discussed, offering greater information on the efficiency of ventricle contraction.

Physiological exercise is desired to reveal underlying symptoms of HFpEF and PH, but exercise in the MR bore is challenging and requires advances in acquisition, reconstruction, and postprocessing to achieve fast imaging capable of visualizing the heart during exercise and minimizing motion artefacts. The viability of ‘real-time’ exercise cardiovascular MR that can capture beat-to-beat variations is demonstrated in this dissertation along with methodology required to achieve the necessary temporal resolution. The potential value of the technique is then shown in a cohort of normal controls and heart disease patients.

The techniques and tools presented in this dissertation demonstrate and advance the ability of MRI to characterize several disease states: from the irregular perfusion of the placenta to poor

cardiac adaptation to exercise. From development *in utero* to end of life, these techniques have the potential to advance diagnosis and prognosis in affected subjects.

Table of Contents

List of Figures

Chapter 1: Introduction

1.1 **Motivation**

Magnetic Resonance Imaging (MRI) is a valuable tool for diagnostic medical imaging. By measuring the response of magnetic moments inherent to hydrogen atoms in the body, MRI acquires images with excellent soft tissue contrast [1]. In addition to anatomical imaging, MRI can also be sensitized to a vast array of functional information. For example, MRI is capable of measuring perfusion [2] and flow [3] by exploiting gradient magnetic fields to encode movement into images [2][3]. The potential for capturing functional and anatomical imaging in the same scan session along with the lack of ionizing radiation makes MRI a compelling alternative to computed tomography (CT) and positron emission tomography (PET), especially for longitudinal studies and use in sensitive populations like children and pregnant patients.

The overarching goal of this thesis is to describe advances in quantitative vascular MRI post processing tools and their use in studying dysfunction of 1) the placenta and 2) the heart.

The human placenta not only affects the health of the mother and fetus during pregnancy, but also lifelong health. Yet it is the least understood, and least studied, of all human organs [4,5]. Current clinical practices, including ultrasound, lack noninvasive tools that can track placental development and function throughout pregnancy. The availability of such tools could help in the early diagnosis of intra-uterine growth restrictions (IUGR)or preeclampsia. This work extends and demonstrates the value of automated placenta cotyledon tracking including flow quantification of individual cotyledons in a zika virus rhesus macaque model. It also presents results of assessing placental perfusion with a velocity selective arterial spin labeling (VS ALS) approach developed at UW early in pregnancy in a large human cohort.

In the heart, diagnosis of pulmonary circulation disease relies on invasive catheter measurements in the right heart during exercise. This work reports on the implementation of novel flow and function analysis at rest and during exercise in the MRI bore for the assessment of cardiopulmonary disease in swine and humans.

The chapters of this dissertation are organized as follows:

Chapter 2: The disease physiology studied in this work is briefly discussed, along with current clinical treatment approaches and their shortcomings. The solutions proposed in this work are then introduced.

Chapter 3: A novel DCE MRI processing technique is applied to a Rhesus Macaque model and compared with pathology from time of delivery. The tool is demonstrated to be accurate to underlying biology and able to separate healthy pregnancies from those infected with zika virus. Placental physiology and the fundamentals of DCE MRI are presented. This work was presented as an oral presentation at the International Society of Magnetic Resonance in Medicine (ISMRM) 2020, a poster at In Utero 2020, and was published in Biology of Reproduction in December 2022.

Chapter 4: Placental perfusion in a large human population is quantified using a state-of-the-art VS-ASL pulse sequence developed at the UW that covers the entire organ. Pros and cons of placental perfusion techniques are discussed alongside the current data from literature. The techniques in this chapter were presented as an oral presentation at the Human Placenta Project (HPP) conference at the NIH in 2020, an oral presentation and awarded Magna Cum Laude at ISMRM 2021, an oral presentation at the Society of

Reproductive Investigation (SRI) 2021. This work has been submitted to Placenta as a full manuscript.

Chapter 5: explores the feasibility of using 4D Flow MRI to evaluate a novel surgical model of induced PH by banding of the pulmonary veins in a swine model. Plots of longitudinal changes in blood flow are presented along with novel flow compartment analysis of the ventricles combining 4D Flow MRI with clinical cine CMR. The material from this chapter was presented as an oral presentation at SMRA 2021, SCMR 2022, and as a poster at ISMRM 2022.

Chapter 6: Advanced real-time CMR techniques are developed and applied to characterize ventricular volumes during simultaneous exercise and imaging. Results are shown comparing the novel technique with established clinical measures as well as comparisons between patients (heart failure with preserved ejection fraction, pulmonary arterial hypertension) and healthy controls. The material from this chapter will be presented as an oral presentation at ISMRM 2023 and is being prepared for submission to JCMR as a full manuscript.

Chapter 7: This final chapter summarizes conclusion contributions and discusses potential future work related to this dissertation.

Chapter 2: Background

2.1 Principles of Magnetic Resonance Imaging

Magnetic Resonance Imaging (MRI) is a powerful diagnostic modality, allowing noninvasive assessment of function and anatomy. MRI is especially valuable because it probes tissue properties without using ionizing radiation. Instead, MRI uses magnetic fields to induce and probe a net magnetization formed by nuclear spins within the body. After introducing the relevant clinical topics, the applications of MRI to quantitative vascular imaging of the application are described in this chapter. A comprehensive description of the fundamental physics and principles of MRI can be found elsewhere [1].

2.2 Placental Physiology and Imaging

2.2.1 Basic Placental Physiology

The human placenta is a crucial organ which develops during pregnancy, acting as a mediator between mother and fetus. Maternal and fetal blood never mix; instead, the placenta allows exchange of nutrients, gas, and waste across its barriers. Maternal blood supply undergoes extensive remodeling during pregnancy to compensate for increased circulation demands. Blood from the maternal circulation is carried through the uterine and ovarian arteries to the radial and spiral arteries of the uterus before finally entering the placenta's intervillous space and functional cotyledons, see Figure 1. Characterized by septa separation, functional cotyledons have also been loosely termed functional domains when noninvasively seen on imaging.

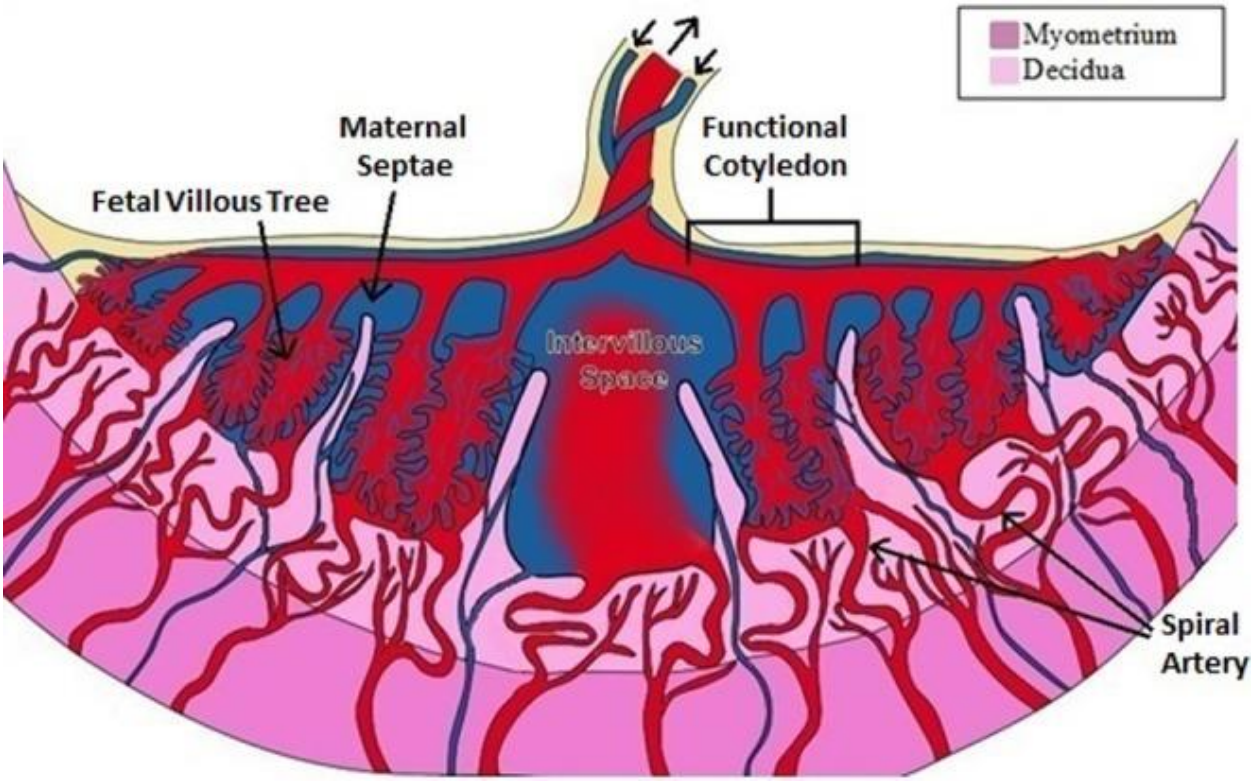

Figure 1: Illustration of placental circulation. Maternal blood enters from the remodeled spiral arteries and bathes the fetal villous trees where nutrient/waste/gas exchange occurs. Reproduced from Denger, Magness, and Shah, Reprod Sci, 2016

2.2.2 Placental Dysfunction

The life-giving exchange that takes place at the placenta is delicate; any maladaptation on maternal or fetal side can result in life threatening complications. Insufficient vascular adaptation and reduced placental perfusion can lead to fetal growth restriction [6–8]. Low uteroplacental blood flow has also been linked to adverse pregnancy outcomes including intra-uterine growth restrictions, pre-eclampsia, preterm birth, and stillbirth. [9–11] Reduced placental perfusion seems to precede several pregnancy complications - non-invasive measures of placental vascular function could aid early diagnosis and guide treatment.

2.2.3 Current Tools and Techniques

Ultrasound is commonly used to evaluate pregnancy but does not provide adequate resolution for the identification of most placental pathology [12–15]. Placental pathology is often focal rather than homogeneous throughout the tissue [16–19], further hampering identification of pathology through the narrow ultrasound view.

The effects of disease often manifest as histopathological changes in the placental tissue, which generally cannot be studied until after delivery. While important for understanding placental dysfunction, term placental histopathology cannot offer information about the development of pathology or inform clinical decisions during pregnancy. Identification of placental dysfunction early in pregnancy with non-invasive imaging could be a valuable tool for assessing maternal and fetal risk [5].

Radiography, computed tomography (CT), and nuclear medicine techniques use ionizing radiation and are usually only used during pregnancy in extreme circumstances when clinically necessary. In most routine cases, they are not worth the increased risk of potential injury to the fetus.

2.2.4 Dynamic Contrast-Enhanced (DCE) MRI

Recent work indicates dynamic contrast enhanced (DCE) magnetic resonance imaging (MRI) can be a powerful tool for interrogating placenta health [20,21]. DCE MRI uses a venously injected contrast agent to obtain functional images with high resolution. As the contrast bolus enters the imaging volume, tissue perfusion can be visualized and quantified. Identifying regions of high or low perfusion can offer insight into the physiological environment, and early identification of placental dysfunction could facilitate heightened surveillance of fetal well-being by ultrasound or placental function by (for example) assessment of soluble biomarkers. Gadolinium based (Gd)

contrast agents are most common for DCE MRI, and this approach has been used in animal model placenta studies [19,22–24]. However, common Gd chelates cross the placenta into the fetus in detectable amounts [25], and there is uncertainty regarding the long-term consequences of Gd exposure in utero [26–29].

2.2.5 Arterial Spin Labeling (ASL) MRI

ASL MRI is a promising method for measuring placental perfusion throughout gestation without the need for exogenous contrast agents.[30] ASL uses specially designed radiofrequency (RF) pulses with image post-processing to highlight magnetization differences of inflowing blood. Several studies have demonstrated feasibility and investigated correlation of ASL perfusion measures with adverse pregnancy outcomes.[31–37] In all forms of ASL, blood is magnetically 'labeled' using RF excitation followed by a post-label delay, allowing magnetized blood to perfuse into the tissue of interest, followed by image acquisition.[38] Most ASL techniques spatially tag blood outside of the imaging volume, relying on the blood inflow from the labeled region into the imaging volume to measure perfusion. This approach faces challenges in the placenta, where the maternal blood supply follows a highly convoluted path from several feeding arteries to an organ with variable shape and location. Additional scans may be needed to locate the inflowing vessels and multiple tagging slices are needed. Such ASL techniques are also degraded by the extended time it takes from the blood to travel from the tagged location to the placenta tissue bed,[38] which is characterized by extraordinarily slow flow, causing differences in arrival times on the order of 10s of seconds throughout the organ.[39,40]

Motion-based ASL tagging, such as velocity-selective (VS)-ASL [38], uses selective RF saturation and flow-sensitive gradients to tag blood based on its velocity rather than spatial location. VS techniques benefit from reduced sensitivity to inflow transit time since blood tagging

is performed within the imaging volume proximal to the tissue itself. VS-ASL has been favored for placental applications due to the ability to simultaneously tag the multiple vessels supplying blood to the placenta without the complications of identifying and placing labelling planes on these vessels.[37,41]

2.3 Cardiovascular MRI in Heart Failure with Preserved Ejection Fraction (HFpEF) and Pulmonary Hypertension

2.3.1 HFpEF

HFpEF is a common disorder with a marked lack of treatment options, and diagnosis is challenging even with invasive measures.[42] As much as half of all heart failure patients have a preserved ejection fraction, and evidence suggests the fraction is increasing over time.[43] An aging population combined with rising incidence of comorbidities such as obesity indicates that HFpEF will increase in prevalence to epidemic levels in coming years. [44] HFpEF often leads to atrial and ventricular dysfunction as well as pulmonary hypertension (PH). PH is a disease state which is characterized by a rise in pulmonary circulation pressure. Both HFpEF and PH present symptoms in advanced stage of disease, resulting in delayed diagnosis. [45]

2.3.2 Pulmonary Hypertension

PH is defined as the buildup of pressure in the pulmonary circulation. The right ventricle (RV) has relatively thin and less muscular walls compared with the left ventricle (LV) and is poorly prepared to push against pressures rising from pathology. All forms of PH result in elevated pressure in the pulmonary circulation but differ in the location and cause of disease. The most common form of PH is postcapillary PH, in which high pressures in the left heart combine with vascular adaptations to increase pulmonary vascular resistance (PVR). In comparison, pulmonary arterial hypertension (PAH), also known as precapillary PH occurs due to pulmonary arterial

disease and mainly affects the RV, resulting in especially elevated PVR. [46,47] Combined pre- and post- capillary PH (CPC-PH) is associated with increased mean pulmonary artery pressure (mPAP), pulmonary capillary wedge pressure (PCWP), as well as vascular changes that lead to increased pulmonary vascular resistance (PVR). As the disease progresses from isolated post-capillary to combined post- and pre-capillary PH (Cpc-PH), mortality rate rises due to right heart failure. PH presents nonspecific symptoms such as shortness of breath or fatigue and is often diagnosed at a late stage as a result. [48] Left heart failure is thought to be responsible for most PH cases [49,50]

2.3.3 Current Tools and Techniques

The current gold standard of HFpEF and PH diagnosis is invasive cardiopulmonary exercise testing with right heart catheterization (iCPET-RHC). During iCPET procedures, the catheter is guided from the jugular vein down the superior vena cava and into the right heart using fluoroscopic imaging. The clinician then measures mean pulmonary artery pressure (mPAP) and pulmonary capillary wedge pressure (PCWP) using the catheter – first with the patient at rest, then during exercise in a recumbent position as they pedal a cycle ergometer.

While a valuable tool for diagnosis and treatment planning, iCPET-RHC carries the risk of being an invasive procedure and requires ionizing radiation during imaging guidance. Cardiovascular MRI (CMR) offers a compelling noninvasive and nonionizing imaging alternative. By averaging data across several heartbeats while the patient holds their breath at expiration, clinical standard CMR achieves excellent (sub millimeter) spatial and temporal (variable, as low as 10s of ms) resolution.[51] Ventricular volume measurements have shown great value in assessing cardiovascular health, and CMR has been established as the gold standard of ventricle

assessment. [52] MRI can also be used to measure blood velocity and volumetric flow [53]; a powerful noninvasive option in assessing PH.

2.3.4 Phase Contrast and 4D Flow MRI

Phase Contrast (PC) MRI is a unique application of MRI using gradients to encode motion of moving blood spins. A relationship fundamental to MR technique is that the precessional frequency of a magnetic spin is proportional to the local strength of the magnetic field. Bipolar gradients are used along the motion encoding direction, which first applies a 'positive' gradient and then a 'negative' gradient of equal but opposite area. The result on the net phase accumulation is that stationary spins have a zero net phase, but moving spins accumulate phase directly proportional to their velocity along the motion encoding direction [53]. Since MR images also have unpredictable background phase, e.g. from magnetic susceptibility or acquisition imperfections, 2 measurements, e.g. one with and one without motion encoding, are necessary to separate the phase contribution from motion. This principle can be applied to all 3 spatial directions in subsequent measurements.

Because of its slow data acquisition, clinical PC MRI is commonly conducted as a 2D breath held scan which exploit cardiac gating to acquire and subsequently 'bin' data for a reconstruction of a 'cine' time series, that contains data from multiple heart beats displayed as a single beat. [54] . This principle can be expanded to so called 4D flow MRI with volumetric coverage and velocity encoding in all 3 directions. [55,56] This powerful technique is most simply implemented as a flow sensitive acquisition along x, y, and z, with a nulled flow reference image. Due to the large amount of data required to sample a 3D volume with 3-directional velocity encoding, often accompanied with respiratory gating, 4D flow acquisitions can have long (10+

min) acquisition times. Breath holding becomes impossible, so prospective or retrospective respiratory gating is generally used.

Reconstruction and post processing of 4D flow data can unlock a wealth of diagnostic information – from basic angiograms, velocity, and flow in arbitrary vessels to advanced parameters such as kinetic energy, vorticity, helicity, wall shear stress, pressure gradient, and flow compartments in the ventricles. [55]

2.3.5 Exercise MRI

Symptoms for PH are usually exertional, thus studies performed at rest may not fully capture the changes in cardiovascular function caused by the disease. Pharmacological testing offers a controlled method of inducing stress, but if the patient is mobile, exercise testing is preferred for its ability to provoke greater physiological stress. [57] Exercise stress testing can reveal underlying symptoms by recreating the patient's symptoms by simulating the exertions of everyday life, aiding diagnosis and prognosis.

Exercise is a critical component of patient evaluation but presents a logistical challenge for MRI. The most recognized and established clinical protocols for exercise testing use an upright treadmill but require patient transfer to the scanner, resulting in heart rate decay at the time of measurement. Equipment within the 5 Gauss line of the scanner must not have any ferromagnetic parts for the sake of safety and to avoid interference with imaging. Most published research uses aluminum, stainless steel or plastic equipment to allow supine exercise while the patient is in the bore of the magnet. Supine exercise does change the inherent nature of stress compared with the upright position. Differences include reduced maximal heart rate (approx. 60%), reduced pVO2, less skeletal muscle recruitment, and increased local leg fatigue.[58–60] Despite the differences, supine exercise in MRI has been shown to be feasible and effective at effecting physiological stress

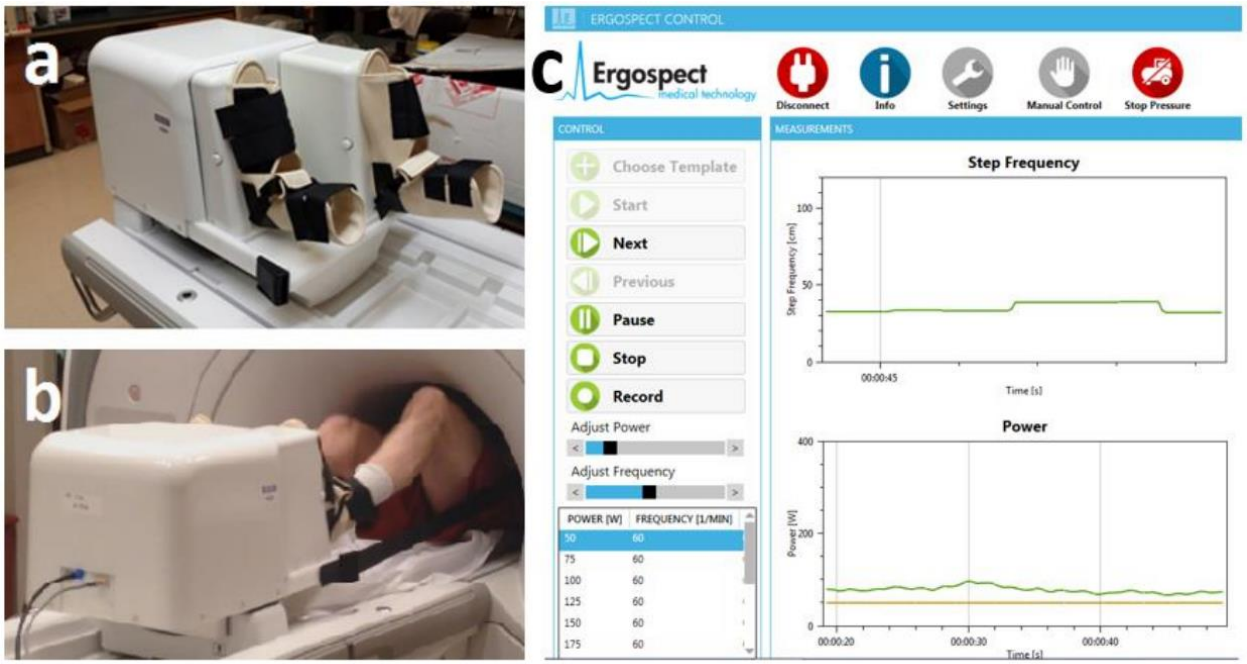

Figure 2 Pneumatic Ergospect stepper. a) shows the boots to strap the subject's feet in place, b) shows the stepper on the scanner table during exercise. c) shows part of the control software tracking step frequency and estimated output power. Figure courtesy of Jacob Macdonald.

in patients. [61] Published MR-compatible exercise options include bicycle ergometers, handgrip dynamometer, static leg lifts using ankle weights, and pneumatic stepping devices.[62] The stepper device used for our studies is shown in Figure 2, featuring fiber optic communication allowing live adjustment of the workload from the scanner control room.

2.3.6 'Real-Time' CMR

Another logistical challenge to CMR during exercise is the increase in motion – both due to elevated heart rate but also from faster breathing and patient torso motion. Traditional CMR uses expiration breath holding along with cine acquitions that 'bin' data across cardiac cycles to improve image quality. Breath-held acquisitions during a pause in exercise have been investigated, but the patient's heart rate will start to recover toward rest immediately. [63,64] Instead, free breathing real-time acquisitions exploit very rapid acquisitions along with advanced reconstructions to image while the patient continues to exercise. Parallel imaging [65,66]

combined with compressed sensing [67] enable reconstruction of vastly undersampled data, saving acquisition time and allowing high temporal resolution reconstructions. Many real-time cardiac approaches also employ radial or spiral sampling trajectories to reconstruct images with incoherent aliasing artifacts. [68–70] In this context, a golden angle or tiny golden angle rotation pattern allows retrospective reconstruction with an arbitrary number of spokes, allowing optimization of spatial and temporal resolution.[68,69,71,72]

The remainder of this dissertation will present the development of tools and techniques to improve quantitative vascular MRI to overcome limitations of current tools and techniques in the patient populations described above.

Chapter 3: Ferumoxytol Dynamic Contrast Enhanced Magnetic Resonance Imaging Identifies Altered Placental Cotyledon Perfusion in Rhesus Macaques

This work has been previously published in the journal *Biology of Reproduction*. See: Seiter DP, et. al., Biol Reprod. 2022 Dec 10;107(6):1517-1527. doi: 10.1093/biolre/ioac168. PMID: 36018823; PMCID: PMC9752971.

3.1 **Introduction**

Placental development plays a crucial role in a successful pregnancy. If the fetus does not receive sufficient oxygen and nutrients via the placenta, the pregnancy may result in fetal growth restriction, preterm birth, or miscarriage [8,73–75]. One cause of placental insufficiency is impaired flow of maternal blood to the placental intervillous space [76]. Placental disease or injury during pregnancy can impair blood flow, limiting oxygen and nutrient exchange with the fetus [77,78]. The effects of disease often manifest as histopathological changes in the placental tissue, which generally cannot be studied until after delivery. While important for understanding placental dysfunction, term placental histopathology cannot offer information about the development of pathology or inform clinical decisions during pregnancy. Identification of placental dysfunction early in pregnancy with non-invasive imaging could be a valuable tool for assessing maternal and fetal risk [5].

Ultrasound is commonly used to evaluate pregnancy but does not provide adequate resolution for the identification of most placental pathology [12–15]. Placental pathology is often focal rather than homogeneous throughout the tissue [16–19], further hampering identification of pathology through the narrow ultrasound view. Recent work indicates dynamic contrast enhanced (DCE)

magnetic resonance imaging (MRI) can be a powerful tool for interrogating placenta health [20,21]. DCE MRI uses a venously injected contrast agent to obtain functional images with high resolution. As the contrast bolus enters the imaging volume, tissue perfusion can be visualized and quantified. Identifying regions of high or low perfusion can offer insight into the physiological environment, and early identification of placental dysfunction could facilitate heightened surveillance of fetal well-being by ultrasound or placental function by (for example) assessment of soluble biomarkers. Gadolinium based (Gd) contrast agents are most common for DCE MRI, and this approach has been used in animal model placenta studies [19,22–24]. However, common Gd chelates cross the placenta into the fetus in detectable amounts [25], and there is uncertainty regarding the long-term consequences of Gd exposure in utero [26–29].

Instead, the current study used a ferumoxytol contrast agent. Ferumoxytol is a superparamagnetic iron oxide nanoparticle (SPION) used in the treatment of anemia in adults with renal insufficiency [Feraheme®, AMAG Pharmaceuticals, Waltham, MA]. Ferumoxytol has been used before as an off-label DCE MRI contrast agent and is considered safe [79–81] by obstetricians to treat iron deficiency anemia in pregnant women [82]. Previous studies demonstrate the feasibility of ferumoxytol imaging in a healthy rhesus macaque model [83–86]. and document its promising ability to quantify perfusion domains thought to represent placental cotyledons [40]. Cotyledons are the functional units of the placenta where maternal blood enters the intervillous space and bathes the fetal chorionic villi, allowing exchange of oxygen, nutrients, and wastes [87,88]. The rhesus macaque placenta has many structural and functional similarities to that of humans, including a hemochorial villous structure segmented into cotyledons [87]. These similarities make the rhesus macaque pregnancy model an excellent option for study of potential applications in human maternal-fetal medicine. We hypothesize that ferumoxytol DCE MRI of the pregnant

rhesus macaque can detect changes in placental structure and function associated with pathology by assessing intervillous perfusion throughout gestation. In this work, we present novel data matching perfusion domain maps generated with ferumoxytol DCE to histopathological analysis of cotyledons in term macaque placentae. Furthermore, we demonstrate trends in placenta structure associated with pathology throughout gestation.

3.2 **Materials and Methods**

3.2.1 Care and Use of Macaques

This study was approved by the University of Wisconsin-Madison College of Letters and Sciences and Vice Chancellor Office for Research and Graduate Education Institutional Animal Care and Use Committee, protocols G005401, G005691 and G005263. Wisconsin National Primate Research Center (WNPRC) female rhesus macaques were housed with compatible males and monitored for breeding and menses. Date of conception was determined (+/- 2 days) based on initiation of the menstrual cycle, observation of copulation and presence of ejaculate, and ultrasound measurements of fetus and gestational sac [38]. Full term in Rhesus Macaques is approximately 165 days [89]. Macaques were cared for by WNPRC staff as outlined in the Animal Welfare Act and the Guide for the Care and Use of Laboratory Animals.

3.2.2 Zika Virus Infection Models

Zika virus (ZIKV)-inoculated animals from two separate experiments were recruited for this MRI study. All animals received Puerto Rican Zika virus/H.sapiens-tc/PUR/2015/PRVABC59_v3c2 (PR ZIKV) or mock inoculation with sterile saline but differed in inoculation method. A total of 14 animals were imaged for this study. A summary flow chart of their treatments is shown in Figure 3. Six animals received injections into the amniotic sac at gestational age (GA) day 55. Of these, two animals received 1x10^4 PR ZIKV (n=2), one received 1x10^5 PR ZIKV (n=1), and

three controls received a saline injection (n=3). The eight remaining animals received 10^4 PR ZIKV by subcutaneous injection at ~GA45, followed by either no intervention (n=1), intravenous infusions over 2-3 minutes of 50mg/kg Zika-specific human immunoglobulin (n=4) or nonspecific human immunoglobulin (n=3) at 1- and 5-days post-infection. Specific details about this latter study and fetal outcomes are reported in further detail elsewhere [40]. Briefly, although all dams experienced productive infection, there were no significant fetal anomalies noted in and no evidence of vertical transmission.

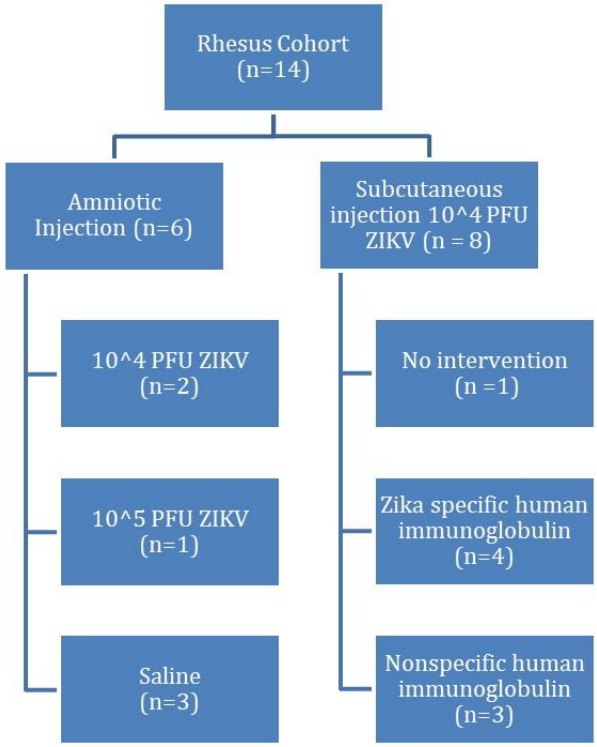

Figure 3 Rhesus Macaque Treatment Cohorts.

3.2.3 Magnetic Resonance Imaging

All animals were imaged up to three times, at GA65 (±1.33 d), GA100 (±2.43 d), and GA145 (±0.92 d), with 10 of the 14 receiving all three scans, and 13 of the 14 receiving the GA145 scan enabling the matching of MRI data to placental tissue pathology from delivery at GA155. Cesarean sections were done before term to ensure placenta recovery for histological analyses since some animals may deliver early and consume the placenta. Animals were food deprived 4-20 hours prior to sedation for the imaging procedure. Sedation was completed by injection of up to 10 mg/kg ketamine followed by intubation and maintenance anesthesia by inhalation of a mixture of oxygen and 1.5% isoflurane. Imaging was conducted in the right-lateral position and respiratory bellows were used to compensate for respiratory motion.

MR images were acquired on a clinical 3.0T MRI system (Discovery MR750, GE Healthcare, Waukesha, WI) using a 32-channel torso coil (Neocoil, Pewaukee, WI). Four-dimensional (4D) DCE data sets were acquired before and during ferumoxytol infusion using a dynamic, 50% efficiency respiratory-gated T_1-weighted spoiled gradient echo product sequence (DISCO, TR=4.8ms, TE=1.82ms, 2.4ms, spatial res. = 0.86×0.86×1.00 mm^3, temporal resolution=5.48s, flip angle=12^o) [40]. Ferumoxytol was diluted 5:1 with saline and administered at 4 mg/kg body weight over a 20 second interval followed by a 20 ml saline flush at the same rate.

3.2.4 Calculation of Perfusion Domain Maps

The placenta was segmented in Mimics (Materialise, NV) using time averaged DCE images to visualize the full extent of contrast enhancement in the tissue (Figure 4A). Subsequently, the segmented DCE data was processed with customized in-house tools (Matlab, Mathworks, Natick, MA) similar to previous reports [22,40]. As shown in Figure 4B, the average signal intensity of all placenta voxels is roughly sigmoidal. However, maximum voxel intensity and time of enhancement can vary widely across the placenta depending on proximity to blood inflow. Our algorithm used a per-voxel thresholding approach, calculating the contrast arrival time for each pixel as the time point when the signal intensity exceeded an empirically determined threshold of 22 times the standard deviation of the signal at initial time points, considered to be background noise without enhancement. The threshold was chosen by checking the intersection of threshold and average enhancement curve. Intersection at approximately 50% enhancement reliably produced the best results by rejecting noisy pixels but accepting inflow areas with proper sigmoid enhancement. The initial time points were determined using the enhancement inflection point of the entire placenta's average enhancement. The resulting arrival time map is shown in Figure 4C. Finally, a watershed algorithm was applied to automatically segment perfusion domains, shown in

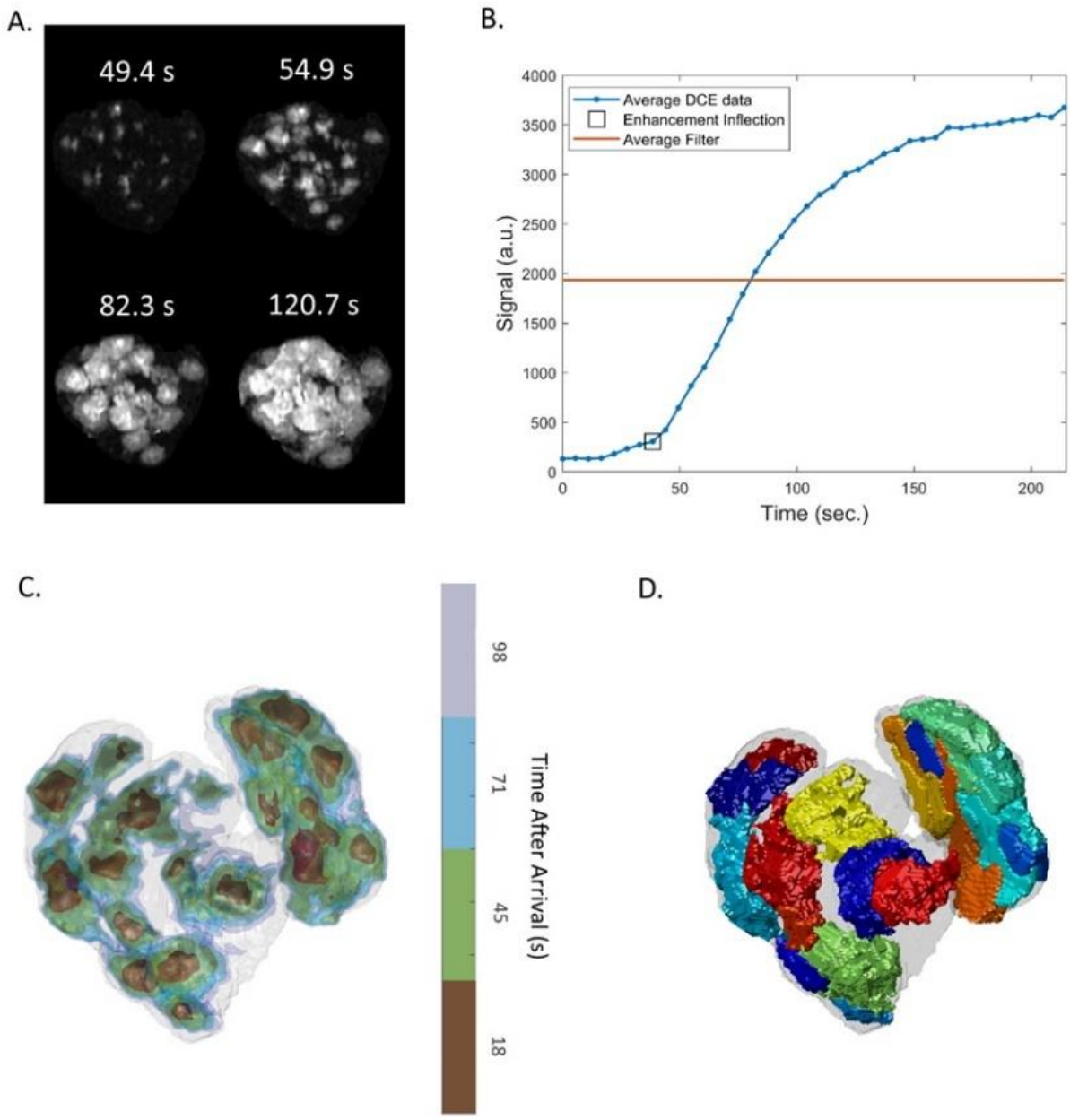

Figure 4 Image Processing Workflow A) Representative example of contrast inflow during a ferumoxytol DCE MRI scan in the rhesus macaque placenta at GA145, shown as maximum intensity projection (MIP) images at four time points relative to the start of the scan. (B). The signal intensity from DCE data averaged across the entire placenta with estimated contrast arrival time (enhancement inflection). After finding the average inflection, the standard deviation of signal in prior frames is used to estimate background noise per voxel. The threshold ($22 \times \sigma_{bkgd}$) is optimal for formation of the arrival time map (C), plotted with isovalues at 18, 45, 71, and 98 seconds (after inflection; shown as color guide on the right of panel C) to visualize the inflow and spreading of blood into the placenta. The perfusion domain map (D) shows the resulting segmentation of perfusion domains based on MRI signal, with a lower volume threshold of 0.5 cm^3. Distinct colors represent distinct functional domains.

and blood flow rate (mL/min) for each placenta. Blood flow to each perfusion domain was calculated using a linear fit of the cumulative total volume of enhanced voxels over time.

3.2.5 Placental Dissection

At GA155, macaques were intubated and sedated and the fetoplacental unit of each animal was collected via cesarean section.

The placenta was photographed and dissected. The photograph of the placenta was annotated electronically to identify the placental cotyledons, as determined visually upon inspection of the chorionic plate. The cotyledons were then dissected, and full-thickness sections (from chorionic plate to decidua) were collected. These sections were laid in tissue cassettes labeled to match the tissue biopsy with the annotated photograph. Tissues were fixed in 4% paraformaldehyde for 24 hours before being placed in 70% EtOH until embedding in paraffin blocks. The paraffin embedded tissues were sectioned at 5μm and stained with hematoxylin and eosin.

3.2.6 Histopathological Analysis

Placental tissue was assessed by an experienced placental histopathologist (TKM) blinded to treatment and imaging data. Hematoxylin & eosin-stained cotyledon sections from all placentas in this study were evaluated for the presence of chronic histiocytic intervillositis (CHIV), placental infarctions (PI), and maternal decidual vasculitis (MDV) according to published criteria [90]. Example images of pathology are shown in Figure 5. The presence or absence of CHIV, PI, MDV, and their combinations in each cotyledon was recorded for the purpose of creating pathological rankings between the assessed placentas (Supplemental Table 1). To aid analysis between

monkeys, an average pathology score per placenta was calculated by adding the total number of pathologies (0-3) in all placental cotyledons and dividing by the total number of cotyledons. This

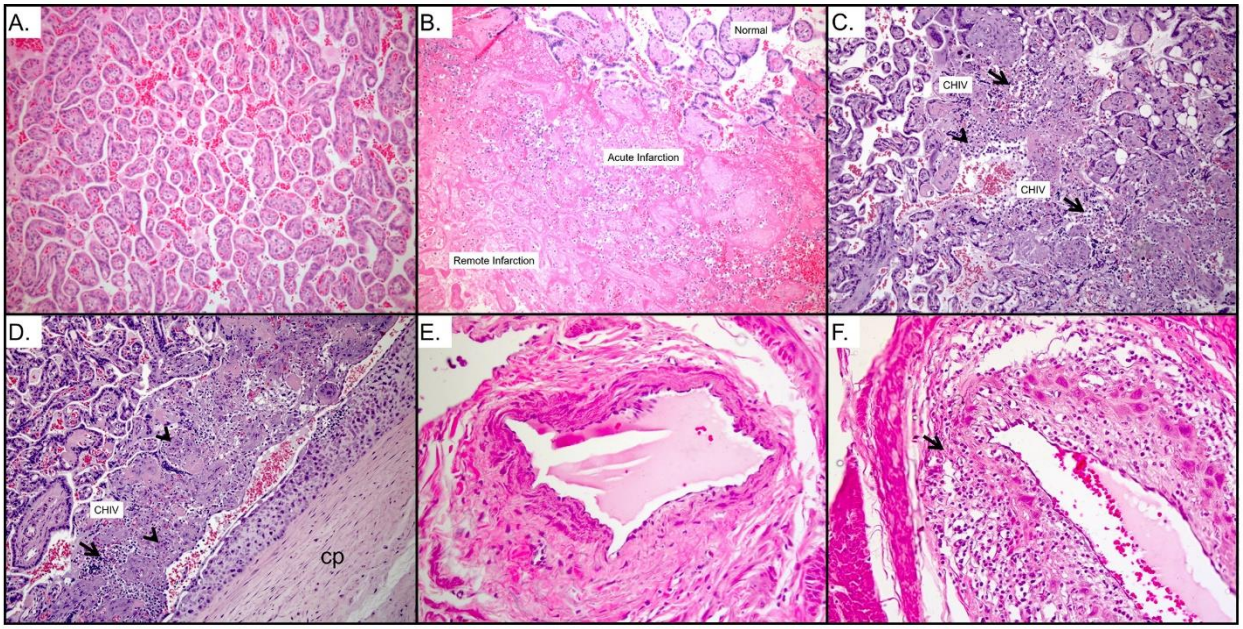

Figure 5 Examples of Chronic Histiocytic Intervillositis (CHIV), Infarctions, and Leukocytoclastic Vasculitis at the Uteroplacental Interface. A) Normal chorionic villi near term compared with cases infected with ZIKV that had more areas of remote infarction (B) and patchy areas of CHIV involving floating villi (C) and beneath the sub-chorionic plate (D) that is unusual for TORCH infections. Compared with normal maternal decidual arteries (E), ZIKV-infected cases occasionally had leukocytoclastic vasculitis (F) with a mixture of infiltrating lymphocytes, neutrophils, plasma cells, and a few eosinophils (arrow).

value provided a useful ranking of the relative degree of pathology between placentas. The three saline injected monkeys scored very low for pathology: 0, 0.08, and 0.09. The level of pathology varied substantially in Zika virus-exposed animals, ranging from 0 to 1.4. There were no statistically significant differences in average pathology score among the groups. For this reason, we did not compare MRI data from Zika with control (saline) pregnancies, but rather binned by pathology score to compare MRI data. Three cotyledons from one animal (Animal 5 on Supplemental Table 1) were lost during processing; data on this tissue is not reported.

3.2.7 Matching Term Tissue and MRI Data

The annotated photos of the placentas were matched with the MRI perfusion domain map developed for the same placenta at the GA145 scan based on organ shape and location of large and

small functional groups (Figure 6). One animal was not included in this comparison since it was not scanned at GA145. If a perfusion domain identified on MRI corresponded to multiple

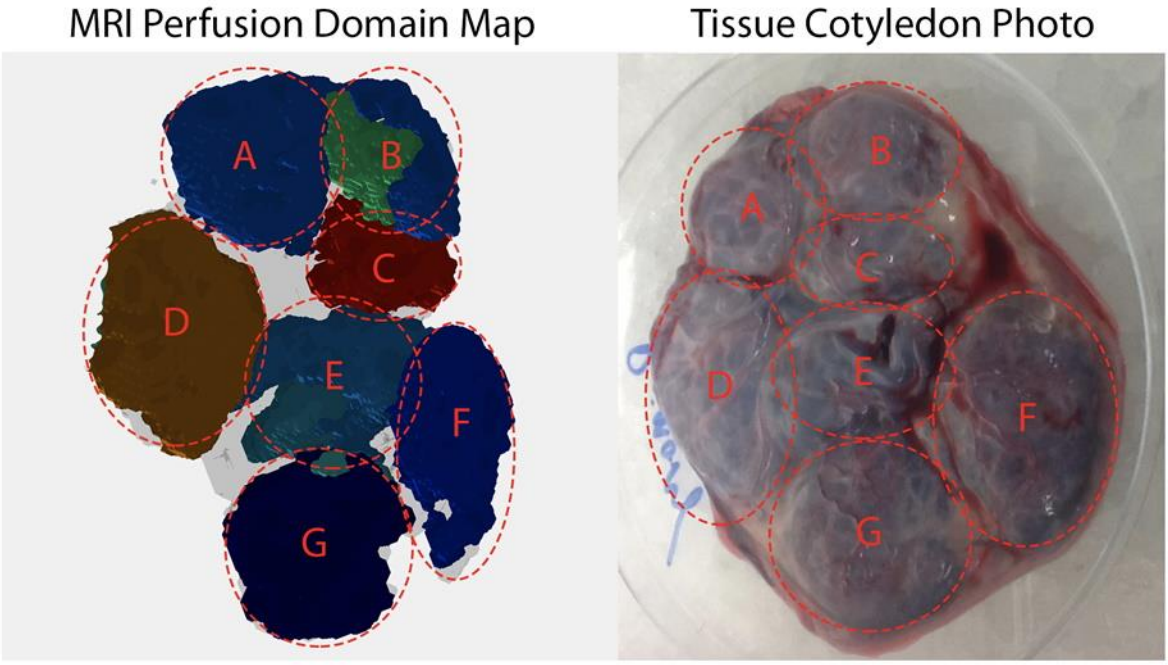

Figure 6 Example of a Perfusion Domain Map Matched to Fresh Placental Tissue. Good agreement is seen between the perfusion domain map at GA145 (left) and the photo of the chorionic plate of a term placenta collected at GA155 (right) of a particular animal in the same orientation. Perfusion domains on the left image are circled in red and labeled with red letters to match the cotyledons circled and labeled in red on the right image.

cotyledons, total volume was summed or distributed to the cotyledons based on their estimated size relative to one another. Once all perfusion domain data were matched to cotyledons, volume data were associated with the appropriate cotyledon pathological scoring as assessed by the pathologist (Supplemental Table 1). Flow rate data was not split according to matching since the flow rate is often not homogeneous within the perfusion domain.

3.2.8 Statistical Analysis: Individual Placenta Comparisons

Only animals that received the GA145 MRI scan were included in this analysis (n=13). After matching cotyledons with perfusion domains, volume values from pathological cotyledons were compared with cotyledons in the same animal without that pathology. Comparison between the

pathological and non-pathological cotyledons was completed by two-way ANOVA, with factors of pathology and animal.

3.2.9 Statistical Analysis: Grouped Animal Comparisons

To test the impact of pathology on perfusion domain flow and volume, individual DCE MRI flow rates and volume values were compared between high and low pathology monkey placentas. Comparisons were made by binning animals into two groups using the total pathology score calculated from histopathological analyses. A term total average pathology score of ≥0.5 was defined to indicate high pathology placentas (n=5) while <0.5 denoted low pathology placentas (n=8). A pathology score of 0.5 was chosen because it indicates, on average, half of the dissected cotyledons contained one of the three possible pathologies. The flow rate and volume values of the two bins were compared using a Wilcoxon rank sum test.

The average volume of matched cotyledons per monkey were also compared between high and low pathology cases using Wilcoxon rank sum test. Use of matched cotyledon data allowed analysis of placenta cotyledon volume grouped by specific pathologies and their combinations. The pathology score cutoff for pathological placentas in the individual pathology analyses was based on the median individual pathology score value instead of 0.5 due to few monkeys being compared. Selecting the cutoff by median ensured more than half of the cotyledons analyzed had that pathology score or lower.

Finally, regression analysis was performed to investigate the dependence of DCE MRI outputs on gestational age. Only monkeys scanned three times were included (n=10) with data separated into high and low pathology groups according to the pathology score cutoff of 0.5. The relationship of perfusion domain number, volume, and total placental blood flow to gestational age was analyzed.

3.3 **Results**

Parameters from analysis of the ferumoxytol DCE-MRI data including number of perfusion domains, their volume, and blood flow at each gestational age, binned by pathology score, are summarized in Table 1. After matching perfusion domains with dissection cotyledon data, the low pathology bin had an error (mean±sd) of 2.4±3.6 segmented domains. On average, the algorithm overestimated the number of domains (as compared with the number observed with dissection at cesarean section) in low pathology placentas. Error for the high pathology bin was 0.0±2.1 segmented domains, thus on average, the number of domains was correctly estimated. Matched domain data and pathology for all subjects are detailed in Supplemental Table 1. All ferumoxytol DCE MRI perfusion domain analysis throughout gestation is detailed in Supplemental Table 2.

3.3.1 Comparisons Across Gestation Binned by Pathology

To test if perfusion domain volume and flow were different in placentas with higher pathology, placentas were binned by pathology score and compared at all three scan timepoints. A statistically significant decrease in perfusion domain volume (Figure 7) at all gestational ages with pathology was measured (50% decrease in median volume at GA65, $p=0.015$, 62% decrease at GA100, $p<0.01$, and 49% decrease at GA145, $p<0.01$). Individual perfusion domain flow comparisons (not shown) demonstrated a statistically significant decrease in flow with pathology at GA100 (33% decrease in median flow, $p<0.01$) and GA145 (36% decrease, $p<0.01$), but not GA65 ($p=0.42$). See Supplemental Table 2 for individual perfusion domain flow and volume values.

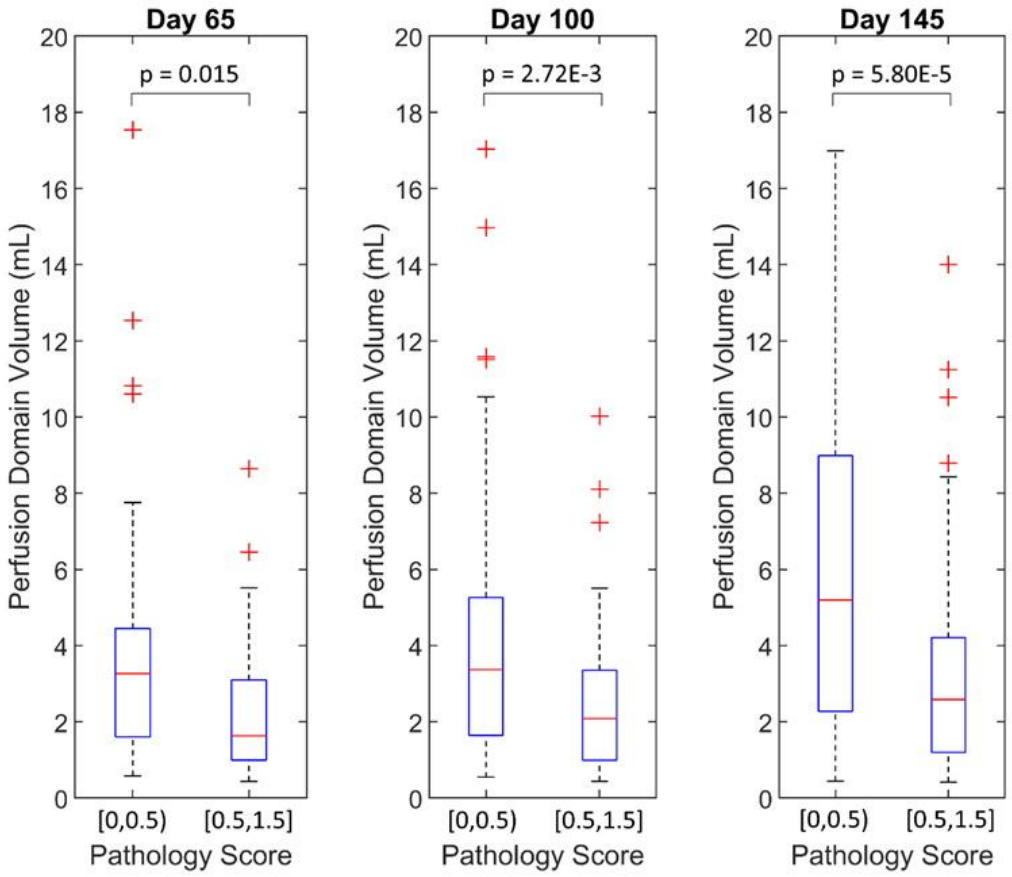

Figure 7 Box-and-whisker plots illustrating the statistically significant decrease in perfusion domain volume with pathology between high and low pathology bins at all three gestational stages. Analysis revealed a 50% decrease in median volume at GA65, p=0.015, 62% decrease at GA100, p<0.01, and 49% decrease at GA145, p<0.01. Domain volumes are separated into two bins by binning monkeys according to pathology score, with one plot per gestational age. A bracket indicates that number is included in the range.

3.3.2 Placental Function with Gestation

To test the dependence of total placental flow rate, perfusion domain volume, and number of perfusion domains on GA, linear regression analysis was performed. Figure 8 illustrates the statistically significant dependence of the total placental blood flow rate (Figure 8A) and number of cotyledons (Figure 8B) on gestational age. Flow, volume, and number all increase as the fetus grows: monkeys below the 0.5 pathology score cutoff exhibited strong correlation of perfusion

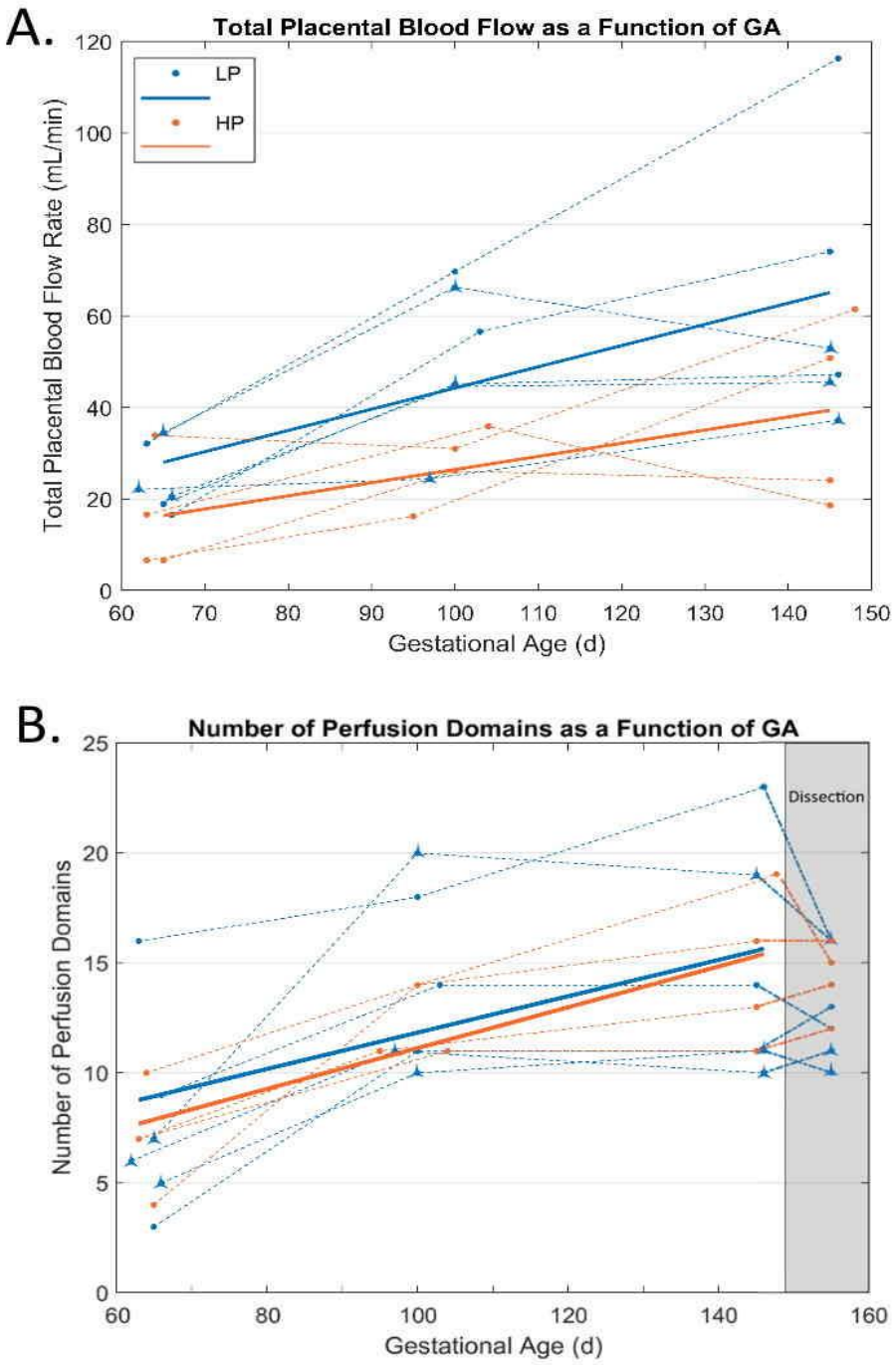

Figure 8 A. Regression analysis showing the statistically significant increase in total blood flow with gestation for both low pathology bin (R2=0.403, p=<0.01) and the high pathology bin (R2=0.369, p=0.03). monkeys (binned using the 0.5 pathology score cutoff). B. Statistically significant increase in number of perfusion domain with gestational data: HP: R2=0.614, p=2.58E-3, LP: R2=0.268, p=0.028. The dashed lines show trends per subject. The points at GA155 are cotyledons counted during dissection for comparison with the final scan at GA145. In both plots, saline injected controls are represented by triangles.

domain volume with gestation (R^2=0.067, p<0.01) and number of perfusion domains with

gestation (R^2=0.268, p=0.028). High pathology placentas had weaker dependence on volume (R^2=0.040, p=0.020) but stronger response to the number of cotyledons (R^2=0.614, p<0.01). Total blood flow rate increased with gestation for both the low pathology bin (R^2=0.403, p=<0.01) and the high pathology bin (R^2=0.369, p=0.03).

3.3.3 Term Matched Perfusion Domain Volumes by Specific Pathology

To investigate whether specific pathologies led to detectable decreases in average cotyledon volume, matched cotyledons were binned by pathology. Figure 9 shows statistically significant evidence for a decrease in cotyledon volume with pathology (p=0.011). When comparisons were split by specific pathology, only PI showed evidence for a similar decrease (p=0.008). All other matched comparisons by pathology at term were non-significant.

Finally, we assessed whether pathological cotyledon volume was different from healthy cotyledons in the same placenta. No statistically significant evidence was found in any of the

individual placentas for any of the pathologies or their combinations when factors of animal and pathology score were used.

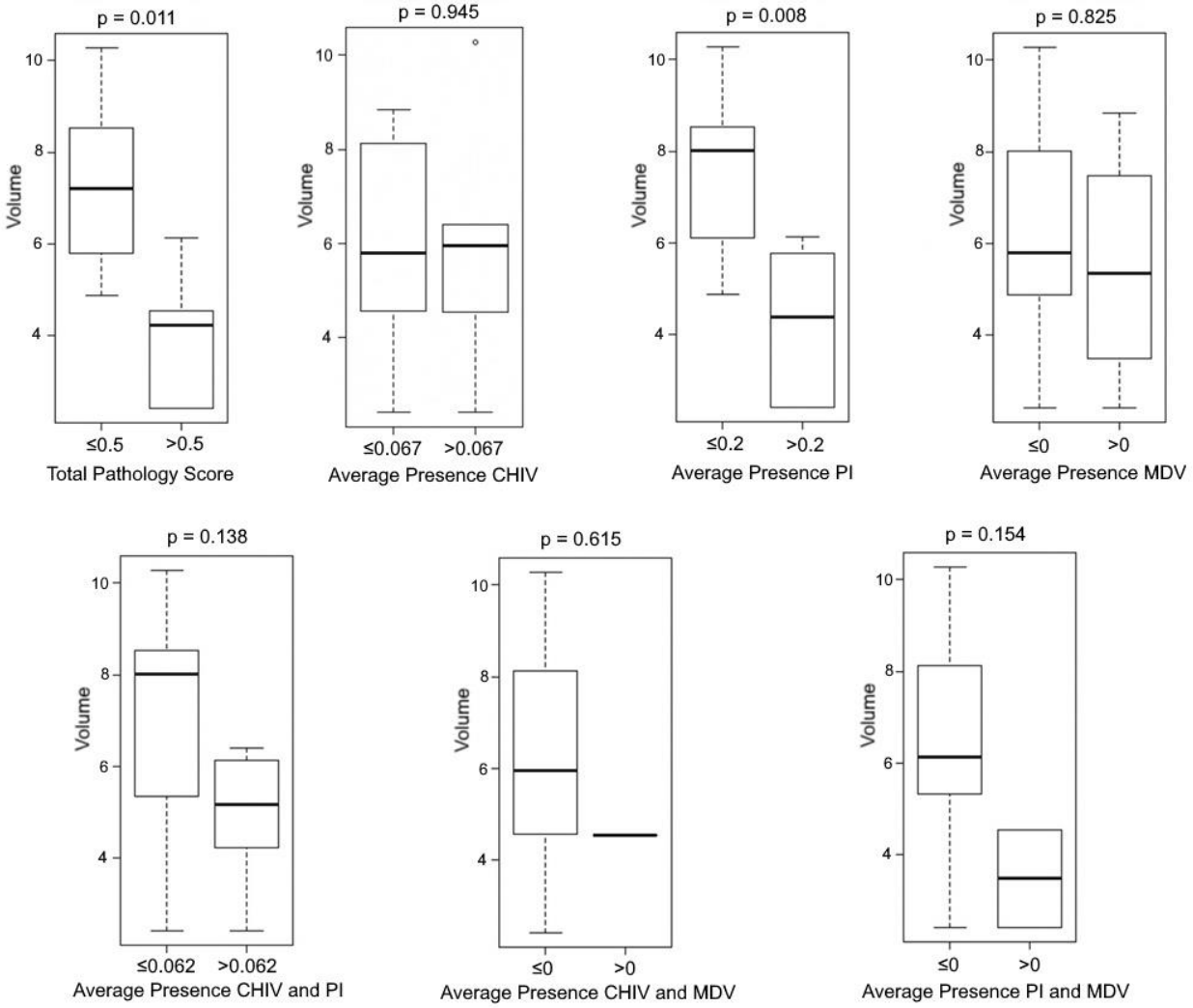

Figure 9 Grouped perfusion domain volume (mL) analysis sorted by specific pathology. Perfusion domain volume values at GA145 were averaged per animal and compared in animals with a pathology against those without. Analysis was completed for each pathology separately: Total pathology score, CHIV, PI, MDV, CHIV and PI, CHIV and MDV, and PI and MDV. Total pathology score is denoted as pathological when above 0.5. All other pathologies have cutoffs based on median volume value. p-values are specific to the pathology listed.

3.4 **Discussion**

In this study, we used dynamic contrast enhanced MRI with Ferumoxytol to non-invasively track rhesus macaque placental structure and function at multiple gestational time points and correlated these measures with pathology in the late third trimester placenta. Zika virus infection produced a varied level of pathology between cases, but our use of a quantitative pathology score allowed

comparisons by severity of effect on the placenta. MRI enabled the assessment of volume and blood flow rate of placental perfusion domains, both of which increased through gestation. The number of perfusion domains from late gestation MRI (GA145) analysis favorably matched with the number of cotyledons confirmed in late preterm dissection (GA155). It was notable that a statistically significant decrease in rhesus macaque placental perfusion domain volume associated with overall pathology identified at the end of gestation is detectable via MRI as early as day 65 of gestation. Such an early difference post infection suggests that physiological or histopathological changes that occur early in gestation persist through gestation to term and can alter future development of histopathology in the perfusion domains. The decrease in blood flow to cotyledons was found to be significant only at day 100 and 145, suggesting changes in cotyledon volume which may occur before the effects on flow are manifest. When the analysis was limited to specific pathologies, only placental infarctions demonstrated a statistically significant association with reduced perfusion domain volume. These results show that the presence of infarctions contribute to factors which alter cotyledon volume in the placenta.

Imaging-based assessment of perfusion domains allows the tracking of placental functional units in vivo through gestation, thereby providing novel insights into placental development and health. Values of cotyledon volume and number of cotyledons are similar to published data using Gd DCE MRI (Table 1), giving confidence in the reproducibility of this approach regardless of contrast agent used [19,22,40,91]. Our perfusion domain flow rate calculation used a simple linear fit of enhanced voxels over time in order to avoid uncertainties introduced by estimation of spiral artery location and contrast wavefront surface area. Our calculated total placenta flow rates are significantly smaller than reported values using an alternative fitting method (Controls: 63.5 $\pm$ 24.6mL/min at GA145 versus 559$\pm$190 mL/min at GA135) [92], but match 4D flow MRI

estimates of macaque uterine blood supply [84]. Calculation of placental flow is highly model dependent, affected by both segmentation and flow fitting method. Differences in pulse sequence and contrast agent may also contribute to the difference in flow rate estimate. Further study is needed.

This pilot study provides insight into the capabilities of DCE MRI applied to the identification of placental pathology. Many factors affect placental function and development, such as diabetes, obesity, and fetal sex [93,94]. Although the modest sample size in the current study did not allow assessment of these factors, we provided evidence that pathology may be linked to cotyledon blood flow and volume. To be clinically useful, additional data are needed to define the range of normal average cotyledon flow and volume throughout gestation. Ultimately, extending similar observations to the human placenta will be needed to confirm the utility of these imaging approaches for potentially considering development of future therapeutic interventions.

To our knowledge, this is the first study to report the increase in cotyledon number and volume through gestation. By allowing noninvasive characterization of blood flow, Ferumoxytol DCE MRI may be useful in future investigations of the physiology underpinning placental development and pathology. One insight provided by this study is that the number of perfusion domains (cotyledons) increased in all placentas between GA65 and GA100, but then was generally unchanged between GA100 and GA145. One possibility is that this represents morphological development of the placenta in relation to the architecture of perfusion and growth of cotyledons that have an optimal perfusion environment. Further studies with additional imaging time points may provide some insight into this question. We have previously shown that there was no impact of ferumoxytol imaging on placental or fetal histopathology or fetal growth [83], or evidence of ferumoxytol accumulation in fetal tissues as detected by MRI [83,85] or by histochemical analyses

or fetal iron content [83], supporting its potential for human use. One limitation of our experiment was the use of two different infection cohorts, amniotic vs. subcutaneous injection. This may have influenced outcomes, however evaluating the actual pathology in each cotyledon provides insight into the mechanisms of disease regardless of source.

3.5 **Conclusions**

In summary, our study provides evidence that pathology caused by early gestation infection decreases cotyledon blood flow and volume in the rhesus macaque placenta. Currently, MRI in pregnancy is reserved for clinical indications where the benefit outweighs the possible risks (e.g., diagnosis of appendicitis, delivery planning for certain fetal anomalies). Ferumoxytol DCE MRI holds great potential and may be useful to noninvasively identify the effects of placental pathologies before irreparable damage has occurred to placenta, fetus, or mother. This assessment may provide additional clinical information to assess the risk to pregnancy or may determine the need for further intervention or management through additional antenatal monitoring or delivery of the fetus. Most pregnancies require supplemental iron regardless of anemia status; since ferumoxytol is already used as a large dose iron supplement to treat anemia during human pregnancy and as an off-label MRI contrast agent, future transition of this work to human pregnancy may be possible.

Chapter 4: Velocity-Selective Arterial Spin Labeling Perfusion Measurements in 2nd Trimester Human Placenta with Varying BMI

This work is being prepared for submission as a full manuscript to Placenta.

4.1 **Introduction**

Placental health plays a critical role during pregnancy and in the long-term health of the fetus [95]. During gestation, complex vascular remodeling occurs to link the maternal blood supply to the developing placenta, allowing for exchange of gas, nutrients, and waste between the mother and fetus. To meet the functional demands of fetal and placental growth, substantial increases in blood flow and vascularization of the uterus occur during gestation. Insufficient vascular adaptation and reduced placental perfusion can lead to fetal growth restriction [6–8]. Low uteroplacental blood flow has also been linked to adverse pregnancy outcomes including preeclampsia, preterm birth, and stillbirth [9–11].

Despite the critical importance of the placenta in fetal development, noninvasive evaluation of the placental perfusion and its function remains challenging. Ultrasound can measure correlates to blood flow such as velocity and pulsatility in the uterine and umbilical arteries, but these measures do not directly probe total uterine blood flow or tissue level perfusion. Further, the measures in large vessels do not provide regional depictions of perfusion which more directly impacts nutrient and gas exchange within the placenta [96,97]. The ability to noninvasively characterize the vascular changes and function in placental tissue could aid in early detection of dysfunction, potentially predict outcomes, and provide potential targets for interventions [4]. Magnetic resonance imaging (MRI) is a non-ionizing, non-invasive imaging modality with excellent soft tissue contrast and the ability to capture both structural and functional information

of entire organs. MRI is increasingly being used as a perinatal diagnostic tool and holds potential for placental evaluation, including perfusion quantification.

Arterial spin labeling (ASL) MRI is a promising method for measuring placental perfusion throughout gestation without the need for exogenous contrast agents [30]. ASL uses specially designed radiofrequency (RF) pulses with image post-processing to highlight magnetization differences of inflowing blood. Several studies have demonstrated feasibility and investigated correlation of ASL perfusion measures with adverse pregnancy outcomes [31–37]. In all forms of ASL, blood is magnetically 'labeled' using RF excitation followed by a post-label delay, allowing magnetized blood to perfuse into the tissue of interest, followed by image acquisition [38]. Most ASL techniques spatially tag blood outside of the imaging volume, relying on the blood inflow from the labeled region into the imaging volume to measure perfusion. This approach faces challenges in the placenta, where the maternal blood supply follows a highly convoluted path from several feeding arteries to an organ with variable shape and location. Additional scans may be needed to locate the inflowing vessels and multiple tagging slices are needed. Such ASL techniques are also degraded by the extended time it takes from the blood to travel from the tagged location to the placenta tissue bed [38], which is characterized by slower flow than other organs commonly imaged with ASL. The arrival time delay between feeding large arteries is on the order of 10s of seconds and heterogenous within the placenta [39,40]. This contrasts with the human brain, most commonly images with ASL, where the arrival times are 1-2 seconds.

Motion-based ASL tagging, such as velocity-selective (VS) ASL [38], uses selective RF saturation and flow-sensitive gradients to tag blood based on its velocity rather than spatial location. VS techniques benefit from reduced sensitivity to inflow transit time since blood tagging is performed within the imaging volume proximal to the tissue itself. VS-ASL has been favored

for placental applications due to the ability to simultaneously tag the multiple vessels supplying blood to the placenta without the complications of identifying and placing labelling planes on these vessels [37,41].

Prior studies have investigated the effect of perfusion on pregnancy outcomes, such as birth weight and IUGR [31,98], but have not fully explored the effect of known maternal risk factors on perfusion, such as obesity. Maternal obesity is increasingly prevalent and is associated with increased risk of hypertensive disorder/pre-eclampsia [99,100] and stillbirth [101]. The mechanisms through which obesity affects fetal outcomes are poorly understood. The purpose of this work is to investigate the relationship between maternal body mass index (BMI) and placental perfusion through an MRI imaging study of obese and non-obese mothers. In these subjects, placental perfusion was collected with an efficient 2D multi-slice VS-ASL sequence that covers the entire placenta with images collected at two gestational ages.

4.2 **Methods**

This prospective study was Health Insurance Portability and Accountability Act compliant and approved by the Institutional Review Board at the University of Wisconsin-Madison.

4.2.1 Subjects:

A total of 97 (24 with BMI≥30) pregnant participants were recruited. Inclusion criteria for this study included: 1. Women with singleton, low–risk pregnancies, 2. Gravida 1 (first pregnancy); or Gravida 2 (second pregnancy with first pregnancy carried to term or miscarried prior to 14 weeks or terminated); or Gravida 3 (third pregnancy with first and second pregnancies carried to term or one previous pregnancy carried to term and the other previous pregnancy miscarried prior to 14 weeks or terminated), 3. Ultrasound confirmed pregnancy dating prior to 14

weeks gestation, 4. Designation of non-obese (BMI 18.5-29.9 kg/M2) or Obese (Class I BMI 30-34.9 kg/M2 or Class II BMI 35-39.9 kg/M2) was based on pre-gravid BMI.

Exclusion Criteria were: 1. Known fetal chromosome abnormality, structural malformation or syndromes in current pregnancy, 2. Tobacco or alcohol or drug use in current pregnancy, 3. Pre-existing autoimmune conditions or other maternal chronic diseases like renal diseases, chronic hypertension, thrombophilia, type I or II diabetes or any vasculopathy, 4. History of sickle cell anemia or sickle cell trait, 5. Patients with clinical factors that places them at high-risk for developing following conditions during pregnancy or developing listed complications like gestational hypertension, pre-eclampsia, HELLP syndrome, fetal growth restriction, abruptio placentae secondary to hypertension or pre-eclampsia, and/or stillbirth/intrauterine fetal death.

Clinical data such as BMI, blood pressure, and pregnancy outcomes were included from prospectively collected routine clinical measures. Adverse outcomes during and after pregnancy were noted: fetal growth restriction (FGR), preterm delivery (PreT), preeclampsia (PreEc), gestational diabetes (GD), or gestational hypertension (GH). Patients with FGR, PreT, and PreEc were grouped for comparison due to similar placental lesions thought responsible for development of these conditions.

4.2.2 Imaging:

Participants received MRI scans at early 2nd trimester and mid-2nd trimester, gestational age (GA) 14- and 20- weeks. MRI was performed on a clinical 1.5T wide-bore scanner (Optima MR450w, GE Healthcare, Waukesha, WI) with a 48-channel phased array torso coil. Participants were imaged in supine position. All participants had the ability to communicate with research MRI staff and to interrupt the study in the event of symptoms of supine hypotension. The pulse sequence diagram for the newly developed VS-ASL perfusion sequence is shown in Figure 10. Two

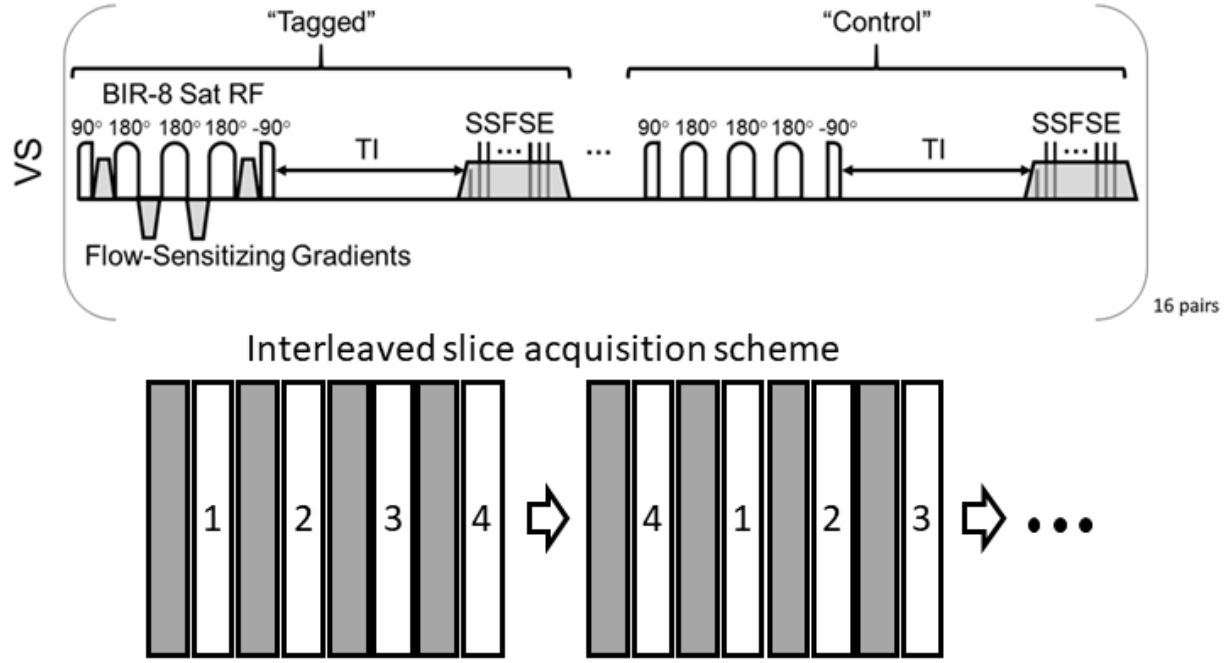

Figure 10 The VS-ASL pulse sequence used for this study. Two interleaved sets of four slices were acquired. Each slice had one proton density image acquired before sixteen pairs of tagged and control images. The order of slice acquisition was rotated as shown between each pair to avoid post label delay bias.

interleaved acquisitions of four, 8 mm sagittal slices each with 16 tag/control pairs using a 2D single-shot fast spin echo (SSFSE) readout were used for full placenta coverage. The acquisition order of the four slices was permuted after each tag/control pair to avoid post label delay bias using the following scan parameters: repetition time TR = 6-7 sec (dependent on placental volume), echo time (TE) = 50.1 msec, acquired matrix size = 128×64, in-plane spatial resolution = 3.28×5.25 mm^2, and total scan time of ~7 min 48 sec. VS-ASL imaging was performed with a 1.2 second post label delay, symmetric BIR-8 VS-ASL preparation[102], a velocity cutoff of V_c = 2.4 cm/sec and R/L velocity encoding. Background suppression was applied using two inversion pulses placed prior to VS-ASL preparation. This provided incomplete background suppression but maintained a small level of signal for image registration. A single proton density reference image was collected for each slice using an identical acquisition without VS-ASL or background suppression pulses.

4.2.3 Data Processing:

Individual tag and control images were registered to the proton density (M_0) reference image using the open source Elastix toolbox.[103] To calculate placental perfusion, acquired ASL tagged and control images (16 pairs) were separately averaged then subtracted to create an ASL difference image (ΔM). Placental blood perfusion (f, mL/100g/min) was then quantified using Buxton's general kinetic model.[104] The resulting eight slices were manually segmented to delineate a 'mask' of the placenta tissue using the M_0 reference image in FIJI.[105] Regional statistical measures of perfusion within the placenta tissue only were then calculated from the perfusion maps and placental tissue masks. Heterogeneity analysis was performed by binning all voxels by increasing perfusion, then for each bin, calculating the percentage of volume receiving that amount or less. These data allow easy comparison of the percent flow contribution from a given percent volume between cases. Subjects that only had a single ASL scan or in which one or both ASL scans suffered from severe motion artefacts or general low image quality were excluded from the analysis.

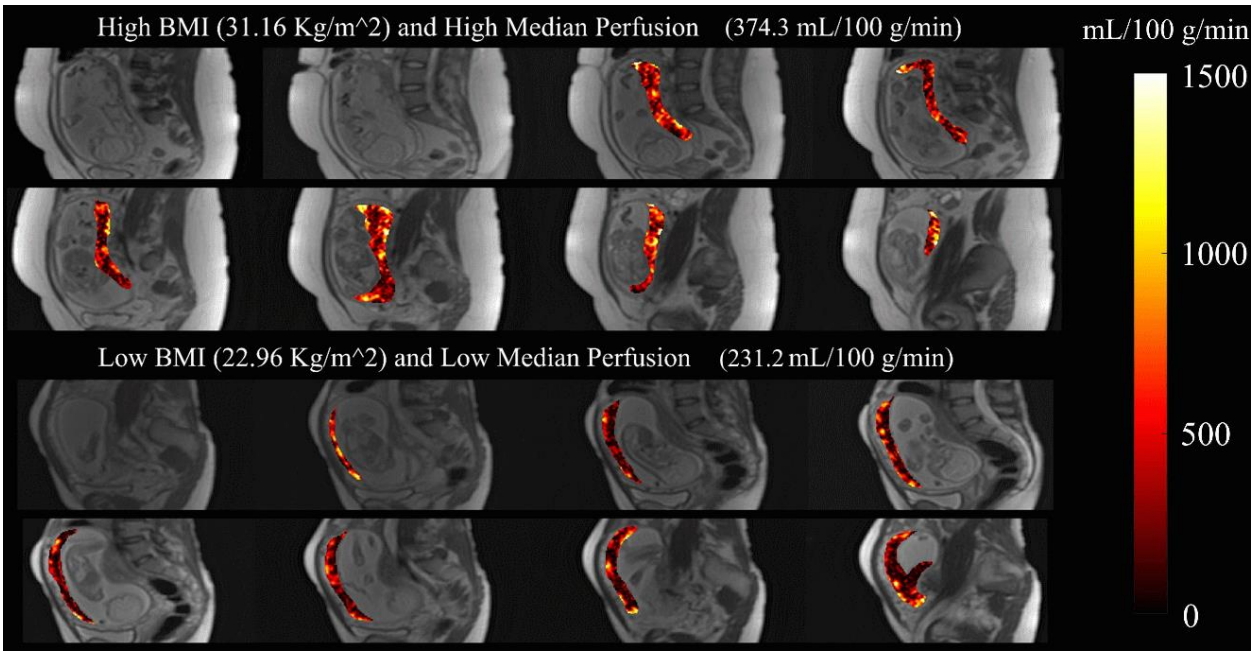

Figure 11 Representative placental perfusion maps are overlaid onto the reference proton density scans for two subjects at 20 weeks GA, illustrating the difference between low median perfusion with low BMI (bottom, 231.2 mL/100 mg/min, BMI = 22.96 kg/m2) and high median perfusion with high BMI (top, 374.3 mL/100 mg/min, BMI = 31.16 kg/m2)

4.2.4 Statistics:

A Student's t-test was used to test differences in patient cohort age and BMI. Linear regression was performed to analyze the response of median placental perfusion to several predictors including fetal weight, maternal BMI, and placental volume. A paired Student's t-test was used to evaluate change in median perfusion with gestational age. A Wilcoxon rank-sum test was used to compare the distributions of median perfusion and heterogeneity between controls and obese subjects at 14- and 20- weeks. A p value less than or equal to 0.05 was defined as statistical significance.

Table 1 Cohort attributes, scans, and outcomes

	BMI<30	**BMI≥30**	**p-values**
Age (years)	29.7±3.7	29.6±2.9	p=0.93
Average Enrollment BMI (kg/m^2)	23.9±2.5	33.3±2.6	p<0.0001
N total	73	24	

N Scanned at 14 and 20 weeks	46	14	
N Adverse (any: GH, GD, PreEc, PreT, FGR)	12	4	
N Fetal Growth Restriction (FGR)	*1*	*0*	
N Preterm (PreT)	*2*	*0*	
N Preeclampsia (PreEc)	*1*	*0*	
N Gestational Diabetes (GD)	*0*	*3*	
N Gestational Hypertension (GH)	*7*	*1*	
N GD & GH	*1*	*0*	

4.3 **Results**

The null hypothesis was accepted for patient cohort age but rejected for patient cohort BMI. A total of 73 patients with BMI < 30 were recruited and 24 patients with a BMI ≥ 30. A total of 16 patients across cohorts experienced adverse outcomes: FGR=1, PreT=2, PreEc=1, GD=3, GH=8, or GD&GH=1. Scans with severe motion artifacts or acquisition errors, were excluded from analysis, leaving, 60 patients (BMI < 30, N = 46) with suitable perfusion data at both imaging timepoints. Table 1 summarizes the cohort attributes, scans, and outcomes. Average median perfusion values from subjects scanned twice are shown in Table 2.

Table 2 Average median placenta perfusion values for subjects scanned twice.

	Wk14 Median Perfusion (mL/100 g/min)	Wk20 Median Perfusion (mL/100 g/min)
Low BMI	216±69	257±67
High BMI	249±86	336±84
Low BMI Adverse	196±75	190±51

Median perfusion values averaged across subjects rose from 216±69 to 257±67 mL/100 g/min in the low BMI cohort between GA 14 and 20 weeks. The high BMI cohort perfusion rose from 249±86 to 336±84 mL/100 g/min, and the group of adverse outcomes stayed constant - 196±75 to 190±51 mL/100 g/min over the same period (Table 2). Example perfusion images overlaid on their representative M_0 reference images from a high and low BMI participants at GA week 20 scans are shown in Figure 11. These images demonstrate heterogenous perfusion across the placental tissue with localized areas of hyper perfusion, presumably from inflowing spiral arteries. Regression analysis in pregnancies without adverse outcomes revealed a statistically significant positive relationship between perfusion and BMI at 20 weeks, see Figure 12 ($R^2 = 0.12$, $p < 0.01$). While a similar trend between median perfusion and BMI was observed in participants with adverse pregnancy outcomes, the relationship was not significant ($R^2 = 0.35$, $p = 0.29$). Regression with fetal weight (14 weeks: $R^2 = 0.01$ $p = 0.37$, 20 weeks: $R^2 = 0.00$ $p = 0.91$) and placental volume (14 weeks: $R^2 = 0.00$ $p = 0.82$, 20 weeks: $R^2 = 0.00$ $p = 0.66$) as predictors were not statistically significant at either time point for either group.

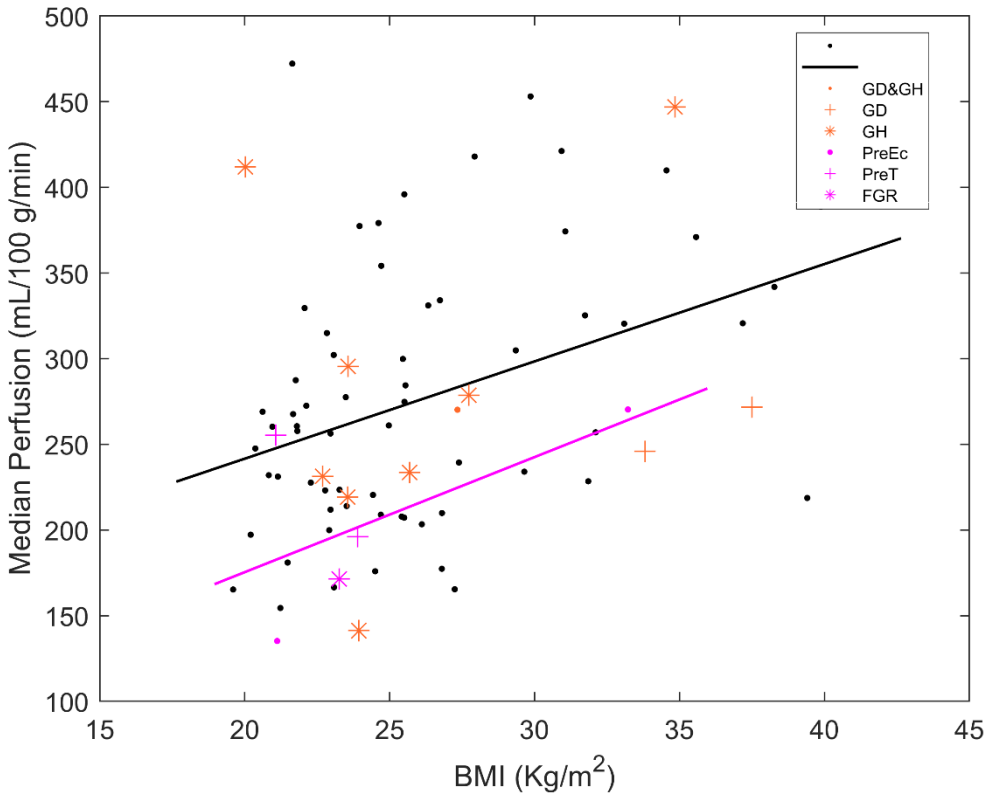

Figure 12 Regression analysis of median perfusion and BMI at 20 weeks gestation, demonstrating a statistically significant positive relationship in the non-adverse pregnancy group. (R2 = 0.12, p < 0.01). No evidence was found for the adverse pregnancy group in purple (R2 = 0.35, p = 0.29). Adverse maternal outcomes are marked: Gestational diabetes (GD), gestational hypertension (GH), preeclampsia (PrE), preterm labor (preterm), and fetal growth restriction (FGR).

As shown in Figure 13, median perfusion increased between GA 14- and 20- weeks for both BMI categories (BMI < 30: $R^2 = 0.086$, $p < 0.05$, BMI > 30: $R^2 = 0.220$, $p < 0.05$). This correlation was not significant in the patients with adverse outcomes ($R^2 = 0.003$, $p = 0.896$). Box plots of median perfusion for both cohorts at GA 14- and 20- weeks are shown in Figure 14, illustrating an increase in median perfusion with BMI relative to both low BMI (31% increase) and adverse outcome pregnancies (76% increase) at GA 20 weeks ($p < 0.01$). Furthermore, we observed a 26% decrease in perfusion in adverse outcome pregnancies relative to low BMI pregnancies ($p < 0.05$). No evidence was found for a difference in whole placental perfusion at GA 14 weeks.

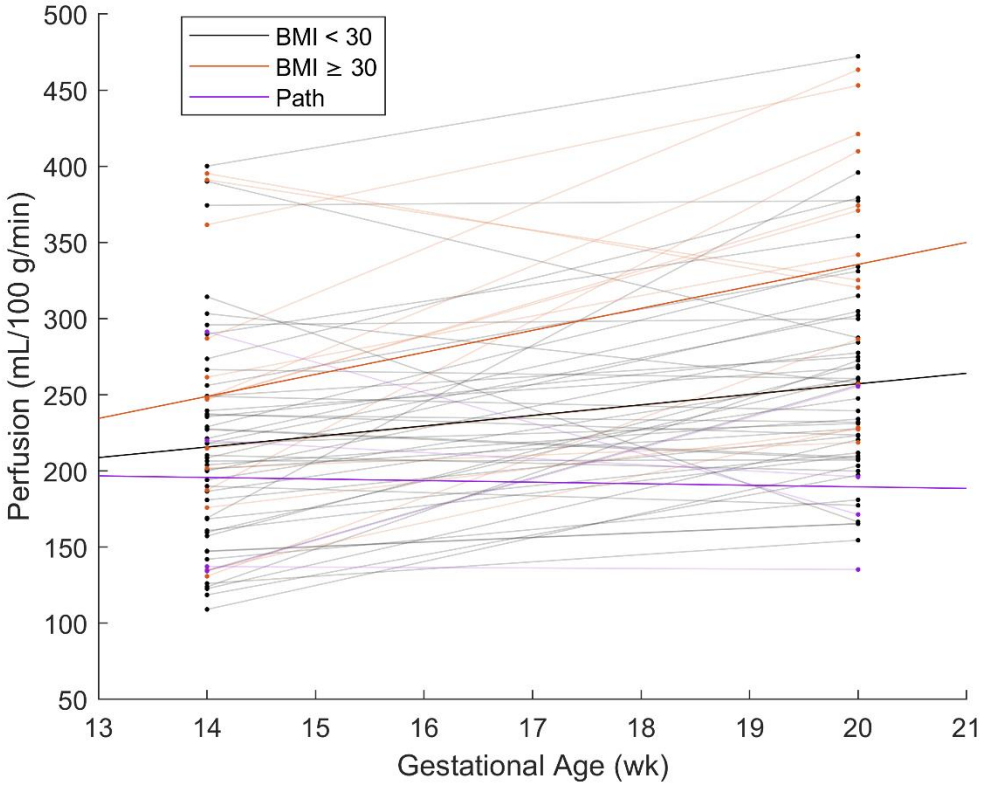

Figure 13 Median perfusion as a function of gestational age for sixty-four subjects scanned at both 14 weeks GA and 20 weeks GA. The subjects with no adverse pregnancy diagnosed and BMI < 30 are indicated by black dots (N=46). The subjects with BMI >= 30 are indicated by orange dots (N=14). The subjects with adverse pregnancy were indicated by purple dots (N=4, FGR, PreEc, PreT). Regression trendlines are shown: (BMI < 30: R2 = 0.086, p < 0.05, BMI >= 30: R2 = 0.220, p < 0.05, adverse: R2 = 0.003, p = 0.896).

Heterogeneity analysis is visualized in Figure 15 with the percentage of volume plotted against the perfusion percentage contributed. A decrease in perfusion heterogeneity with BMI at GA 20 weeks was observed ($p < 0.05$), but not 14 weeks. The curves shown are visibly different between high and low BMI cases, illustrating the statistical evidence that low BMI placentas receive a greater fraction of the total perfusion from a smaller fraction of the placenta volume.

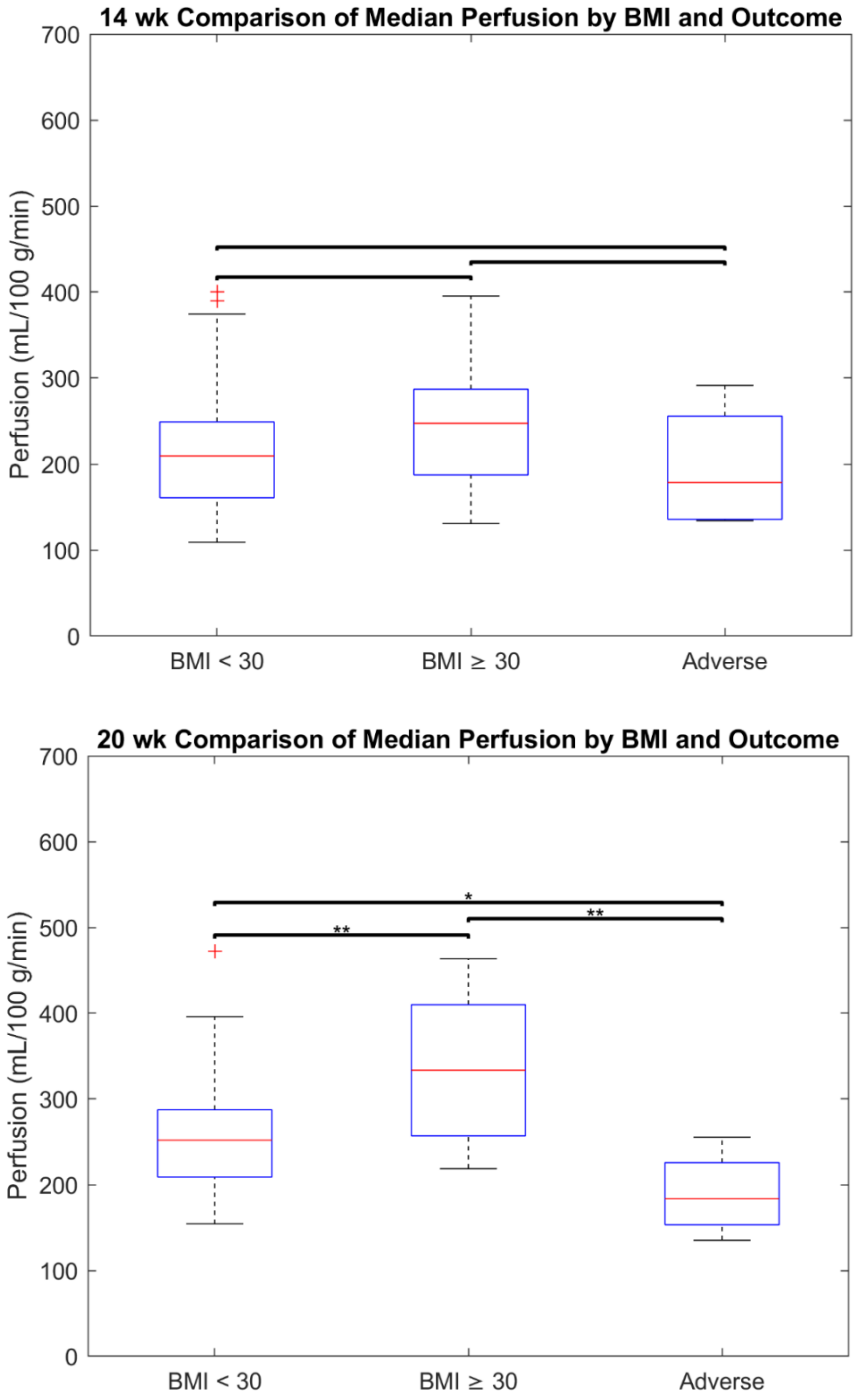

Figure 14 A visualization of the spread of data at each gestational age for each cohort: BMI<30 (N = 46), BMI >= 30 (N = 14), and adverse outcomes (PreEc, PreT, or FGR, N = 4, all BMI<30). Comparisons using a Wilcoxon Rank-Sum test show statistical evidence for an increase in perfusion with BMI relative to both low BMI and adverse pregnancies at GA 20 weeks ($p < 0.01$). Statistical evidence is also shown for a further decrease in perfusion of adverse relative to low BMI pregnancies ($p < 0.05$). No evidence was found for a difference at GA 14 weeks.

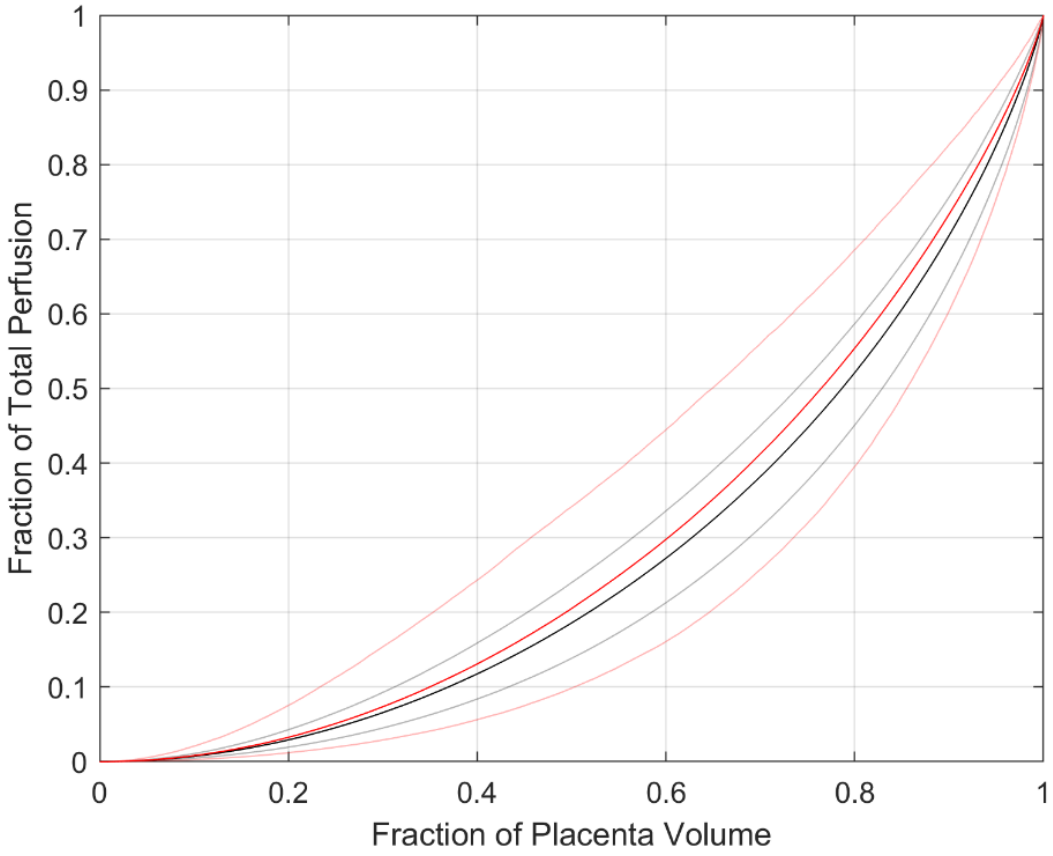

Figure 15 A plot of placenta heterogeneity comparing the relative contributions of a given fraction of placental volume to total perfusion. Red lines are subjects with BMI >= 30. Statistical evidence exists for a decrease in heterogeneity with BMI at 20 weeks gestation. ($p < 0.05$) This is easily seen at the 70% volume mark, from which low BMI subjects receive ~35% of placental flow while high BMI subjects receive ~40%. In other words, low BMI subjects receive a larger fraction of placental flow from a smaller fraction of total volume.

4.4 **Discussion/Conclusion**

This study used VS-ASL to tag blood in the intervillous space along with the multiple tortuous vessels that supply the placenta. Acquired images were used to measure placental perfusion in low and high BMI participants. Perfusion across the entire placenta was measured using a newly designed VS-ASL sequence with 2 interleaved multislice acquisitions and rotating order slice encoding to vary the delay times. By labelling all blood moving above the cutoff velocity within the imaging volume, VS-ASL provides the means to tag the blood in multiple

tortuous vessels that supply the placenta, removing the need for multiple tagging planes with complex plane placement and mitigating errors from delayed vascular filling [31]. To our knowledge, this is the earliest measurement of VS-ASL perfusion in the human placenta in on-going gestations. Our analysis provides evidence that median perfusion increases with BMI, suggesting obesity may not be associated with reduced placental perfusion at these early gestational time points. There are multiple possible explanations including (1) the risks associated with obese pregnancy are not vascular but due to other factors (e.g. metabolic); (2) the increase in perfusion is compensatory to other placental restrictions (e.g. oxygen exchange); (3) median VS-ASL may not fully account for the growth of the placenta; possible development of perfusion deficit later in gestation and/or (4) the VS-ASL measure itself is biased by body habitus [31]. This study also presents statistical evidence for an increase in normal and high BMI subject placental perfusion between 14- and 20-week gestation. Other studies have also measured an increase in perfusion with gestational age during a similar time span [33,36].

Healthy participants in this study were measured to have an average median perfusion at 20 weeks gestation of 257 ± 67 mL/100g/min (BMI < 30, N = 46) and 336 ± 84 mL/100g/min (BMI $\geq$ 30, N = 14). For comparison, in healthy participants of 20–40-week gestation, Gowland et al. measured a placental perfusion rate of 176±24 mL/100g/min and Duncan et al. measured 209 mL/100g/min using a 2D FAIR sequence [34,35]. Similarly, Zun et al. utilized a 3D VS ASL sequence to measure a placental perfusion of 188±44 mL/100g/min at 21-39 gestational weeks [31]. An alternative 3D ASL technique known as pseudo-continuous ASL (pCASL) demonstrated lower perfusion values (106±27 mL/100g/min at 14–16-week gestation and 117±26 mL/100g/min at 19-22 gestation week) [36]. As pointed out by Duncan et al. [34], the expected perfusion at term (40-week gestational age for humans) is 110 mL/100g/min assuming a maternal blood flow of 600

mL/min and an average placental mass of 550 g. Harteveld et. al published evidence for the dependence of measured placental perfusion on VS-ASL metrics such as velocity encoding direction, velocity cutoff value, and inflow time [32,106]. VS-ASL perfusion is a measure of blood delivered from both the maternal and fetal circulations, while other ASL sequences (e.g., pCASL) solely measure maternal blood to the placenta. Thus, the measures of VS-ASL may lead to overestimation of placental perfusion if the perfusion is assumed to be solely maternal. Depending on encoding direction, VS-ASL may label bulk fetal or maternal motion, making perfusion image inspection important during anatomical segmentation. Harteveld's paper showed that placental VS-ASL perfusion measurement is sensitive to chosen parameters, a factor which may contribute to the difference between reported values and literature. Despite these confounding factors, overall trends should remain the same between groups, such as the increase in perfusion with gestational age and BMI. Our study specifically found a positive association between BMI and ASL perfusion measures.

Heterogeneity of placental perfusion has been investigated previously and has been linked to deposition of fibrin by Hutter et al [107]. In more recent work Liu et al [108] and Janzen et al [109] focused on quantifying regions of high placental perfusion in a single pCASL slice to estimate heterogeneity. Their metric has shown promise and may predict ischemic placental disease but is limited without volumetric coverage. Placental perfusion is undeniably heterogeneous – volumetric or multislice approaches offer the greatest likelihood of capturing variation across the entire placenta. Although overall perfusion increased with BMI, we also report evidence for a decrease in perfusion heterogeneity with BMI. The cause of this change is unknown: it is possible obesity reduces placental fibrin, reducing heterogeneity while improving overall

perfusion. It is also possible that the VS-ASL is biased by increased noise or B1 variability that occurs in obese subjects.

There are several limitations to this study that warrant further investigation. One limitation is the small number of subjects with adverse outcomes. This is inherent to the prospective recruitment of at-risk individuals and larger or more targeted study may be needed to identify differential BMI and perfusion interactions in cases of adverse outcomes. Further work is also needed to correlate the MRI based perfusion measures to other MRI measures and those measurable from ultrasound. In future studies it may be beneficial to measure VS-ASL perfusion at later gestational time points to identify how durable the level of increased perfusion remains.

In conclusion, this study provides evidence for an increase in overall placental perfusion but decrease in perfusion heterogeneity with BMI. Further work is needed to evaluate these factors and compare them to alternative methods, such as dynamic contrast enhanced MRI. Validation of the true placental perfusion values using VS-ASL is still needed against a "gold-standard" perfusion measurement technique such as xenon computed tomography [39], or [^{15}O] water positron emission tomography [110], likely only possible in animal models.

Acknowledgements

We gratefully acknowledge GE Healthcare for research support of UW-Madison, and funding support from the NIH Human Placenta Project (U01-HD087216).

Chapter 5: 4D Flow MRI Analysis of Flow, Velocity, and Cardiac Flow Compartments in a Swine Model of Pulmonary Hypertension

5.1 Introduction

Pulmonary hypertension (PH) is a common consequence of left heart failure (LHF) and is usually identified from elevated pulmonary artery (PA) pressure. All forms of PH result in elevated pressure in the pulmonary circulation but differ in the location and cause of disease. The most common form of PH is postcapillary PH, in which high pressures in the left heart combine with vascular adaptations to increase pulmonary vascular resistance (PVR). Precapillary PH is generally due to lung disease, and results in especially elevated PVR. Combined pre- and post- capillary PH (CPC-PH) is associated with increased mean pulmonary artery pressure (mPAP), pulmonary capillary wedge pressure (PCWP), as well as vascular changes that lead to increased pulmonary vascular resistance (PVR). As the disease progresses from isolated post-capillary to combined post- and pre-capillary PH (Cpc-PH), mortality rate rises due to right heart failure. PH presents nonspecific symptoms such as shortness of breath or fatigue and is often diagnosed at a late stage as a result. [48] Left heart failure may be responsible for the majority of PH cases [49,50]

The development of PH is an active area of study and is not well understood due to the many forms of disease and lack of early detection. Imaging approaches which assess both RV and PA show promise for aiding early detection and guiding treatment but require further study. An animal model inducing high mPAP and PVR without damaging the left heart may be the simplest way to obtain insight into disease progression. In this work, we build upon methodology introduced by Pereda et al [111], banding the inferior pulmonary vein in swine to induce severe pulmonary hypertension while preserving the left heart. The disease severity is confirmed using

RHC, the current gold standard for diagnosis of PH. All of the primary diagnostic metrics can be measured using invasive right heart catheterization (RHC): mPAP, PVR, PCWP, and TPG [112,113]. However, this invasive procedure requires surgical intervention and ionizing radiation for guidance, introducing inherent risk and complicating its role in follow-up procedures. While echocardiography is accessible and convenient for screening, volumetric imaging to assess the entire cardiopulmonary system is desired.

Magnetic Resonance Imaging (MRI) offers a compelling non-invasive and non-ionizing option and has grown in popularity as the imaging modality used to evaluate and guide treatment of PH. Cardiac MRI is the gold standard for quantifying ventricular volumes and their function and can capture blood flow and velocity data during the same exam. Additionally, evaluation of the pulmonary venous structure, flow, and velocity are all possible with a single scan using 4D Flow MRI. 4D flow scans can retrospectively provide measurements through virtually any cut planes of interest within the scan field of view and has shown great value in applications throughout the body.[55,56] MRI is perfect for clinical trials and follow-up scans after treatment.

In this study, we evaluate severe PH independent of left heart failure in a swine model using cardiovascular MRI techniques aimed at characterizing pulmonary vascular and right heart effects of Cpc-PH.

5.2 **Methods**

Invasive pulmonary vein banding (PVB) [111] was performed in nine white swine (9.78±0.9kg) using a non-occlusive banding of the inferior pulmonary venous (IPV) confluence. A sham operation without band placement was performed on four swine. Each swine was scanned 12-16 weeks after banding using cine bSSFP for cardiac function, CE MRA for vascular anatomy, and radially undersampled 4D flow MRI [114] (3.0 T MRI scanner [Discovery MR750, GE Healthcare, Waukesha, WI], TR=6.3ms, TE=2.1ms, isotropic resolution=1.95mm^3, flip=8^o, total scan time=13min).

Swine PVB02, PVB04, and Sham 2 were scanned additionally one to two more times between 8-16 weeks post-surgery, to facilitate longitudinal analysis.

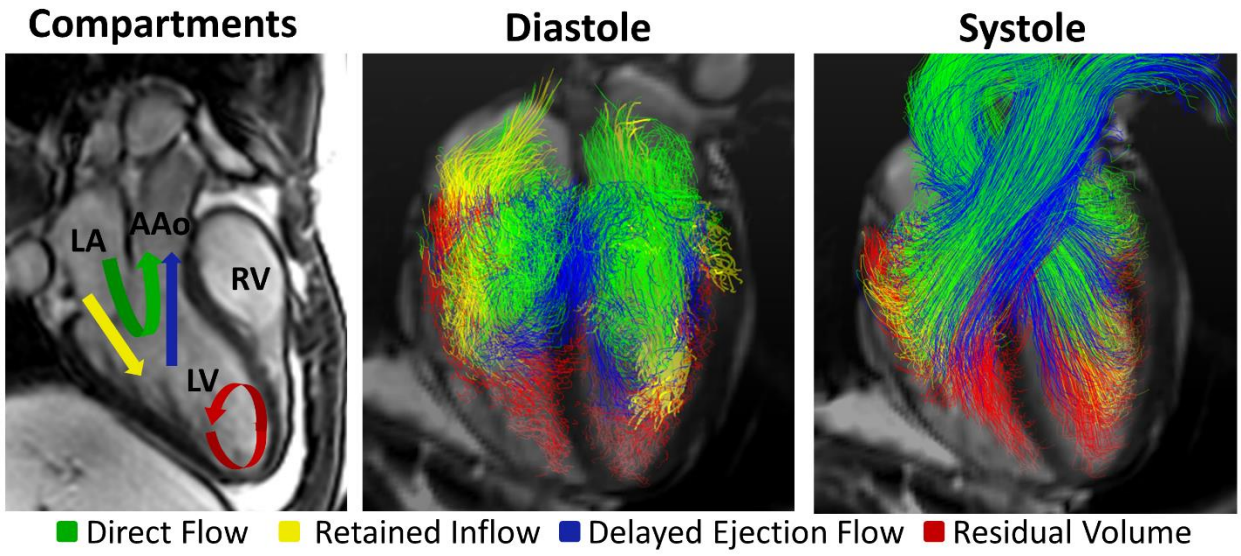

Figure 16 Illustration of the flow compartment analysis with direct flow, retained inflow, delayed ejection flow, and residual volume visualized. Courtesy of Phil Corrado, Ph.D.

Cut planes were placed to measure velocities and flow in the vessels of interest using Ensight (Ansys, Canonsburg PA) and processed using custom software in Matlab (Mathworks, Natick MA). Flow pathline visualizations were also created in Ensight. RHC was performed within hours of each MRI exam. Cardiac flow compartment analysis[115],[116] was performed by segmenting

both ventricles in bSSFP cine images from 16 weeks post-surgery across all cardiac phases. After registering the ventricle segmentations with 4D Flow magnitude data using ITK-SNAP, in house scripts were used for flow pathline generation and classification into 1) direct flow – enters and leaves the ventricle in one cardiac cycle, 2) delayed ejection flow – starts within but leaves the ventricle during systole, 3) retained inflow – enters during diastole and remains in the ventricle during systole, and 4) residual volume – starts within and remains in the ventricle. These categories are visualized in Figure 16.

5.3 **Results**

Four swine were banded at the confluence of left and right inferior pulmonary veins (LIPV, RIPV) and five swine had a band placed on the RIPV alone. Swine body weights and standard deviations at scanning intervals are reported in Table 3, demonstrating an increase with growth in all three cohorts.

Table 3 Swine treatment, number, weights, and right heart pressures at MR scanning intervals post operation.

	n	kg	σ	mPAP (mmHg)	σ	PVR (mmHg·min/l)	σ
8 Weeks							
Sham	1	31.6	~	18.8	~	1.8	~
IPV	3	37.4	2.0	27.7	3.5	2.1	0.4
RIPV	5	31.2	7.8	20.5	4.8	1.9	0.5
12 Weeks							
Sham	0	~	~	~	~	~	~
IPV	1	30.9	~	51.0	~	11.0	~
RIPV	2	37.1	2.1	18.4	0.4	1.5	0.1
16 Weeks							
Sham	4	57.2	1.6	22.0	2.9	1.4	0.5
IPV	3	60.2	5.1	32.8	8.7	1.8	0.8
RIPV	4	60.0	13.0	29.6	4.3	1.8	0.4

Cardiac volumes and standard deviations at the scanning intervals are shown in Table 4.

Table 4 Swine cardiac volumes from invasive right heart catheterization at the scanning intervals post operation.

	n	RVSV (mL)	σ	LVSV (mL)	σ	RVEF (%)	σ	LVEF (%)	σ
8 Weeks									
Sham	1	19.0	~	27.0	~	53.0	~	53.0	~
IPV	3	23.3	7.3	33.0	6.7	48.0	14.2	49.3	12.7
RIPV	5	17.0	4.6	29.5	5.4	50.3	14.5	56.8	13.7
12 Weeks									
Sham	0	~	~	~	~	~	~	~	~
IPV	1	19.5	~	41.6	~	29.0	~	55.0	~
RIPV	2	28.0	4.0	29.5	7.5	66.5	1.5	56.5	6.5
16 Weeks									
Sham	4	41.5	5.0	38.0	4.9	65.3	5.8	51.5	12.1
IPV	3	42.3	9.4	47.3	9.7	56.3	2.6	48.3	2.1
RIPV	4	41.0	13.3	50.2	10.0	54.0	12.4	59.5	6.5

Flow pathline visualization is shown in Figure 17, illustrating the effects of the band in each placement compared with sham. The banded vessel is visibly narrowed, and a velocity jet is especially seen in PVB01 with the band placed on the IPV confluence.

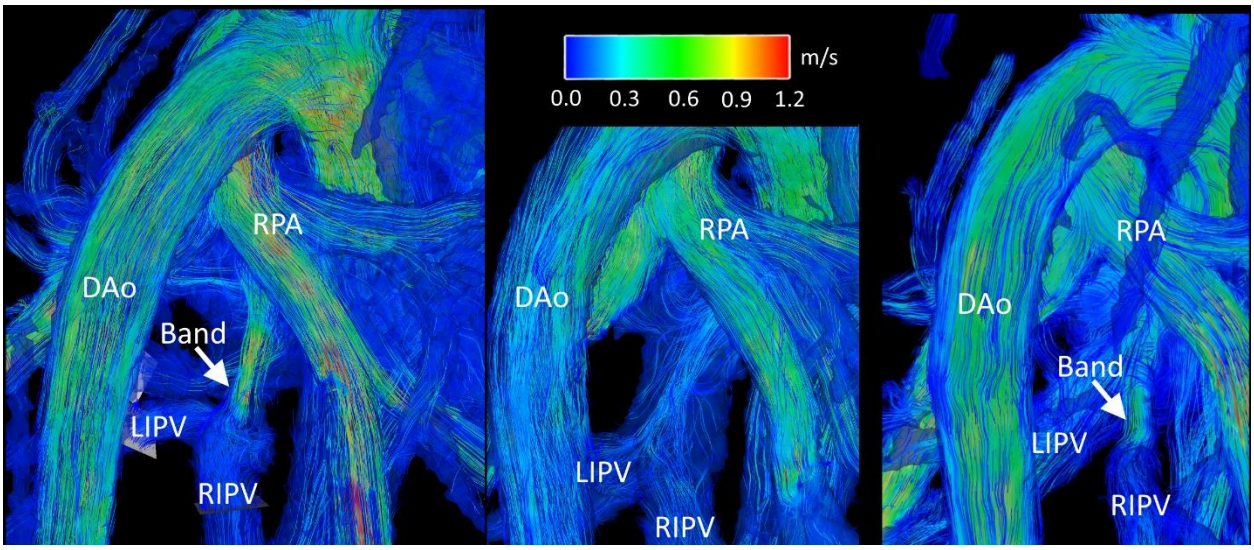

Figure 17 Flow pathline visualization of PVB01 banded on the IPV confluence (Left), Sham 1 (center), and PVB03 banded on the RIPV only (Right). Descending aorta (DAo), Right Pulmonary Artery (RPA), and Left and Right Inferior Pulmonary Veins (LIPV, RIPV) are labelled for reference. Band placement is shown.

Figure 18 Flow data for minor and major vessels in the three cohorts, illustrating the redirection of blood away from the band in the case of swine banded on the RIPV alone. Figure 18 presents flow data from the major and minor vessels of the heart combining the 12- and 16-week timepoints.

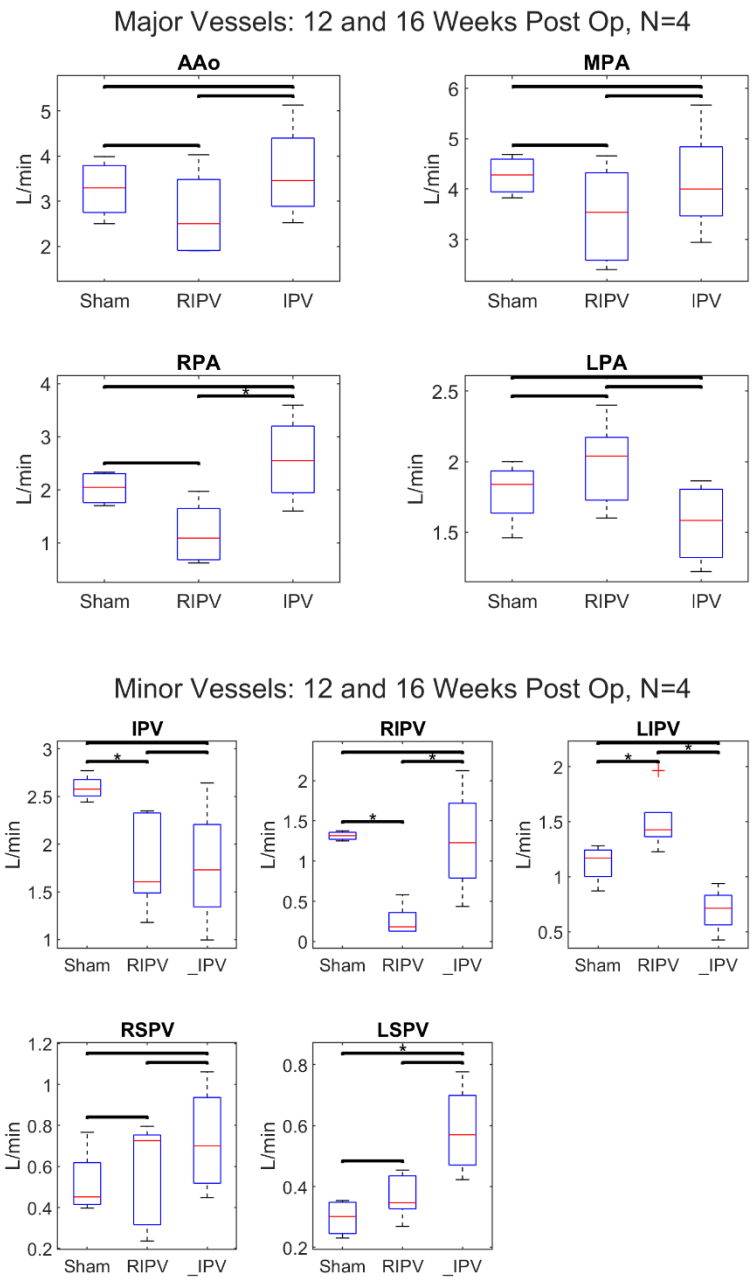

Figure 18 Flow data for minor and major vessels in the three cohorts, illustrating the redirection of blood away from the band in the case of swine banded on the RIPV alone.

Of the swine with scans at 16 weeks post-surgery, at least 2 from each group had sufficient image quality to analyze at least one of the ventricles using flow compartment analysis. Three swine were excluded from RV analysis due to motion or unforeseen fiber optic catheter guide wire artifacts. Pie charts reporting compartment analysis are shown in Figure 19, illustrating a potential decrease in RV direct flow (7%) between sham and banded swine.

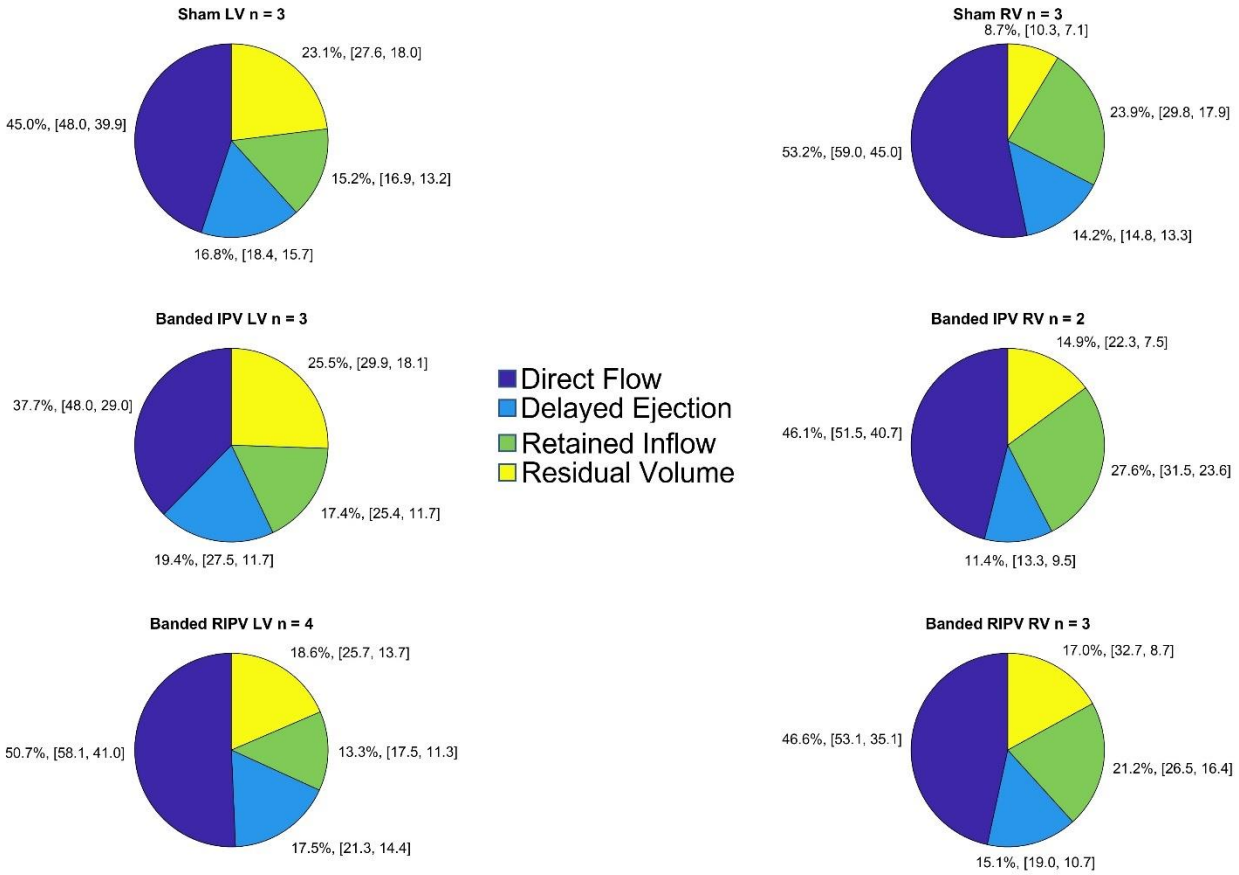

Figure 19 Flow compartment analysis for LV and RV compared between sham and banded swine. Banded swine exhibit a decrease in RV direct flow (7%). In addition to mean values, [min, max] values are overlaid on the pie chart.

5.4 **Discussion**

In this study, we used 4D Flow MRI to evaluate a novel swine model of severe PH independent of left heart failure. While the IPV confluence was targeted for banding, placement on the RIPV in five swine provided a unique banding of half the pulmonary return circulation for comparison. The surgical banding procedure is challenging, involving working through a small (~5-6 cm) incision to locate and band the vessels: 4D Flow MRI allowed confirmation of success and location of the difficult procedure and quantification of blood flow and velocity.

Catheter pressures indicate mild response to banding – a consequence of the erroneous banding on RIPV resulted in a low number of subjects per banding group, precluding statistical analysis. Values reported in Table 3 indicate mPAP may rise due to banding, but PVR does not appear different between the groups. This may indicate that simple postcapillary PH was achieved by banding instead of the desired pre- and post-capillary PH.

Swine with RIPV bands were able to partially compensate for reduced RIPV flow through the LIPV. Both banded cohorts show a trend of redirecting blood to the superior PVs compared with shams. While RV stroke volumes are similar between the cohorts, ejection fraction and flow compartment analysis may reveal underlying inefficiencies in the RV function. Registering the 4D Flow and bSSFP images may offer greater information into disease progression than a simple ejection fraction.

The banding model causes PH to develop over time, offering unique opportunity for insight into disease progression. While more swine are needed to validate the value of flow compartment analysis in this model, similar increased LV direct flow percentages have been reported in healthy swine during dobutamine stress tests. [117] To our knowledge, this is the first use of RV flow compartment analysis in a swine model.

5.5 **Conclusion**

In this study, we used 4D flow MRI to evaluate a swine model of induced Cpc-PH without left heart failure, enabling exclusive study of vascular and right heart changes with PH.

5.6 **Acknowledgments**

We gratefully acknowledge GE Healthcare for research support of UW-Madison, and funding support from NIH R01HL147590. Dr. Oechtering receives funding from the German Research Foundation (OE 746/1-1).

Chapter 6: Real Time Cardiovascular MR During Exercise in Heart Failure with Preserved Ejection Fraction and Pulmonary Hypertension

The animal model described demonstrated the value of 4D flow MRI for assessing PH but lacks an exercise component which has been shown to improve diagnosis and prognosis. This final study presents my work developing and testing high temporal resolution cardiac imaging (referred to as 'real time' CMR). Multistep exercise challenges are recorded in healthy subjects, and results are compared with single step submaximal exercise imaging in a HFpEF and PH patient population.

6.1 **Introduction**

Heart failure with preserved ejection fraction (HFpEF) and pulmonary arterial hypertension (PAH) are two specific cardiopulmonary diseases in which exercise intolerance is defined by cardiac reserve.[118,119] While pathophysiology in these two diseases differs, identifying left and right ventricular contractile reserve with exercise can provide insights into mechanisms of exercise intolerance and disease prognosis.[118,119] The epidemiological burden for both diseases is significant and with improving therapies, it is imperative to diagnose and stratify these patients according to risk early in disease.[46,120] Heart failure with preserved ejection fraction (HFpEF) is a common disorder accounting for nearly half of all heart failure patients.[43] An aging population combined with rising incidence of comorbidities such as obesity indicates that HFpEF will increase in prevalence to epidemic levels in coming years.[44] As a primary left ventricular (LV) diastolic disease, HFpEF often leads to secondary post-capillary pulmonary hypertension (PH) and right ventricular (RV) dysfunction.[45,121,122] In comparison,

pulmonary arterial hypertension (PAH) occurs due to pulmonary arterial disease and mainly affects the RV.[46,47] Both diseases suffer from delayed diagnosis due to vague symptoms of dyspnea and exercise intolerance.[46,120] Moreover, a common diagnostic feature for both diseases is need for invasive right heart catheterization (RHC) to measure cardiopulmonary pressures, ideally with exercise.[45,123–125] However, facilities for invasive exercise testing are not widely available and there is desire for non-invasive exercise testing to minimize risk of invasive testing.[45] Echocardiogram offers a noninvasive alternative, but echocardiography is considered unreliable for HFpEF identification, and image quality suffers significantly during exercise.[45,123]

Cardiac magnetic resonance (CMR) is non-invasive, is the gold standard for measures of global cardiac function[126], and its value to characterize HFpEF and PH is an active area of research.[127,128] Current clinical cardiac MRI requires breath holds, which may conceal early symptoms at rest-only images, and cine reconstructions, which require good cardiac gating and constant heart rate. These requirements conflict with the desire for physiologic exercise to phenotype PH and HFpEF.[129] Exercise compromises ECG gating and exacerbates motion artifacts, impairing cine reconstructions. Thanks to improvements in hardware, fast acquisition techniques, and reconstruction algorithms, real-time (RT) cardiovascular MR imaging (CMR) with high temporal resolution has become possible.[130–136] RT CMR can reduce or eliminate the need for ECG and breath holding. Exercise CMR in healthy controls is feasible and shows value, but best practices remain uncertain.[62,137] We hypothesize that RT CMR exercise imaging is feasible and can offer a noninvasive alternative to RHC in assessing exercise-induced changes in heart function caused by HFpEF and PAH, exploiting the images themselves to extract gating metrics. Here we present cardiac MRI data obtained with a newly implemented real-time

acquisition, reconstruction, and postprocessing pipeline, comparing data trends from controls with HFpEF and PAH patients from rest to submaximal exercise.

6.2 **Methods**

Twelve adult patients reporting symptoms of NYHA class II dyspnea were prospectively enrolled for two-step exercise procedure in the cardiac catheterization laboratory: invasive cardiopulmonary exercise testing (iCPET) followed by RV pressure-volume loops, both in a semi-recumbent position. This was followed by exercise CMR on the same day. Eight controls without a history of dyspnea were enrolled for exercise CMR only.

iCPET and Pressure-volume loop data:

The iCPET protocol has been previously described in detail.[125,138] After a 15–30-minute rest period post-iCPET, all subjects underwent real-time RV pressure-volume (PV) loop acquisition at rest, stages of exercise (every 25 watts), and recovery. These methods are also previously described.[139] Briefly, the RV PV-loop measurements were obtained with a high-fidelity conductance catheter (CD Leycom, Zoetermeer, the Netherlands) and rest volumes were calibrated later to cardiac MRI-based RV volumes. Averaged end-systolic and end-diastolic volumes (ESV, EDV) were acquired from 10 to 35 pressure-volume loops for each subject at rest, exercise stages, and recovery. Right ventricular: pulmonary arterial coupling was defined as ratio of end-systolic: arterial elastance.[139,140]

Exercise protocol

Patients and controls were imaged on a 3T scanner (Discovery MR750, GE Healthcare, Waukesha, WI) with an 8-channel cardiac coil at rest and during exercise with a pneumatic MRI-compatible exercise stepper (Cardio Step Module; Ergospect, Innsbruck, Austria) with stepping resistance automatically adjusted to maintain a target exercise power. Patients referred from RHC exercised for a single step with power adjusted as needed to increase HR to reach 70% of maximal HR measured during iCPET. The controls exercised at increasing increments of 50W to a maximum of 100-250W depending on perceived difficulty. Controls were then allowed to rest for 5 min before repeating rest imaging followed by a second 100W exercise step to test repeatability. All subjects exercised for 3-5 minutes to reach steady state heart rate (HR) before imaging.

Magnetic Resonance Imaging Protocol

To minimize field inhomogeneity around the heart, volume-selective standard shimming was used. Localization scans at the transverse, two-chamber, and four-chamber view of the LV were acquired to localize short-axis planes. Short axis slices were acquired across the whole heart during rest and exercise. Participants were scanned at rest using a breath held balanced steady state free precession (bSSFP) cine product sequence reconstructed at 40 cardiac phases: TR/TE/Δz=3.3 ms,1.27ms,7mm, spatial resolution=0.78x0.78mm^2. A 2D multislice radially undersampled bSSFP RT sequence was used for real-time imaging at rest and during exercise: 3,000 projections acquired continuously with 326 samples per spoke and a 0.75 fractional echo readout: TR/TE/Δz=2.9 ms,1.1ms,8mm. Radial RT acquisitions were reconstructed using an ungated RT reconstruction. After binning projections for RT reconstructions with 10 spokes/frame (Δt=29 ms), images were reconstructed to a matrix of 160x160 for a spatial resolution=2.25x2.25mm^2 using parallel imaging and compressed sensing (with temporal total variation and spatial wavelet L1-norm penalties) via

the BART[141] toolbox using coil sensitivity maps determined by ESPIRiT.[66] The penalty weights were qualitatively chosen: λ_{TV}=0.008 and $\lambda_{wavelet}$=0.004.

Image analysis

The ungated RT reconstruction of data produces a large number of images – 300 per slice. In order to facilitate analysis, respiratory and cardiac motion was extracted from the images. Respiratory motion was calculated by manually drawing a line from left lung into the dome of the diaphragm when visible in SA slices closer to the apex, then from the right lung into the liver in SA slices near the base of the heart when the diaphragm was no longer visible. The edge of the diaphragm was tracked over time and used to automatically extract expiratory frames. Heart rate was calculated from semiautomatic segmentation of the left ventricle using Otsu's method[142] on an image stack closely cropped around the left ventricle (Figure *20*). Expiration end diastole (ED) and end systole (ES) frames for both the right ventricle (RV) and left ventricle (LV) were manually segmented and used to calculate stroke volume (SV) and ejection fractions (EF). Cine reconstructions were analyzed in Segment,[143] while expiration RT ED/ES frames were identified visually and segmented in the ImageJ[144] segmentation editor. Slice limits were used to improve reproducibility and consistency in SA segmentation: the most apical slice must have a visible blood pool at ES, while the most basal slice must not show outflow tract at any part of the cardiac cycle.[127] Finally, RV volumes obtained with RT MRI and with catheter lab PV loop were compared for rest and during exercise.

Statistical Analysis

MATLAB (Mathworks, Natick, MA) was used for all statistical analysis. Pearson's correlation was used for comparison of metrics measured with the clinical gold standard cine method and the estimations from real-time imaging at rest as well as for comparing the repeated real-time acquisitions. Linear regression using groups as fixed categorical variables without interaction was used to test the relationship between heart rate and ventricle volumes. Finally, correlation was calculated between the pressure-volume (PV) loop volumes and real-time volumes during rest and exercise. Bland Altman analysis was performed, and the mean difference was calculated to estimate the bias between the measurements.

6.3 **Results**

Twelve patients (6 Females) underwent iCPET and MRI. Based on the iCPET results, six patients were classified as HFpEF, five as PAH, and one as no PH. Baseline clinical and exercise invasive hemodynamics of HFpEF and PAH groups are summarized in Table 1. Both groups had similar age and BMI. With invasive hemodynamics, severity of pulmonary hypertension (mPAP and mPAP/CO slope) was similar. Although not statistically significant, HFpEF subjects had a lower heart rate response with exercise (chronotropic incompetence, well-documented phenomenon in HFpEF) [145]. With pressure-volume data, RV volumes increased with exercise with a blunted stroke volume response, hence the RVEF declined with exercise. Eight additional healthy controls were scanned, of which the majority (n=7, 5 Females) had an average age of 28 ± 4.2 years and weighed 67 ± 8.4 kgs, while one subject was 70 years old (F, 52 kgs).

An example central SA slice RT reconstruction from systole to diastole during exercise is presented in Figure *21*. Multiple dyspnea patients struggled with breath holds (n=3), corrupting slices of the clinical cine SA images. Ventricle volumes could be segmented in all real-time scans at rest and exercise except for three late-stage (one 150W and two 100W repeated) RT exercise

scans that had banding artifacts impairing ventricle segmentation. Heart rate and respiratory phase could be extracted from all RT scans. With exercise, ECG uncertainty increased to the point of becoming unreliable during exercise. Given at rest, the RT HR estimation had a reasonable comparison with ECG-based heart rate (an average error of 5 ± 4 BPM), this increased confidence in exercise heart rate with RT exercise gating results. Due to lack of validation of power (in watts) between stationary ergometer in catheterization laboratory and MRI-stepper, we present analysis of data based on heart rate achieved as a surrogate of exercise stage. The volumes measured from the free breathing real-time acquisition correlated significantly with the volumes measured from the clinical cine gold standard scans. (Figure 22) Test-retest correlation of the healthy control rest real-time volumes at rest was significant ($p<0.05$, $n=8$), but only end diastolic volumes were statistically significant in exercise repeatability correlation ($n=6$).

As mentioned above and described in Figure *20*, we used heart rate as an indicator of exercise stage. To further estimate stroke volume and ejection fraction responses with exercise, we performed regression analyses using exercise heart rate as a reference. Regression of stroke volume (SV) and heart rate are shown in Figure 23 with statistics and fit values shown in Table 5. Statistical evidence exists for an increase in healthy control LV SV with HR, but no evidence of the same relationship was found for PAH or HFpEF patients. Trends are shown but no statistical evidence exists for a relationship between RV SV with HR in controls, PAH, or HFpEF.

Regression of EF with heart rate was not significant for either ventricle for any cohorts (Table 5). While most relationships were not statistically significant due to small sample size, we noted interesting trends with physiological significance. The slopes of these relationships indicate that stroke volume (LV and RV) increase with exercise in normal controls, while the opposite

occurs in HFpEF which may indicate biventricular limitation. Interestingly in PH, the slope for RV stroke volume was negative while LV stroke volume had a positive slope.

Table 5 Regression data of ventricle stroke volumes with heart rate as a surrogate of exercise stage. An asterisk * indicates $p<0.05$.

	LV SV				RV SV			
	R^2	p value	Slope (mL/BPM)	Intercept (mL)	R^2	p value	Slope (mL/BPM)	Intercept (mL)
Ctrls	0.10	**0.03***	0.25	30.83	0.07	0.08	0.19	8.16
PAH	0.03	0.66	0.15	33.93	0.01	0.83	-0.05	22.92
HFpEF	0.05	0.60	-0.17	49.29	0.46	0.06	-0.42	48.03

	LV EF				RV EF			
	R^2	p value	Slope (%/BPM)	Intercept (mL)	R^2	p value	Slope (%/BPM)	Intercept (mL)
Ctrls	0.04	0.19	0.08	56.95	0.04	0.20	0.13	47.82
PAH	0.04	0.56	0.16	60.36	0.36	0.07	0.74	-8.29
HFpEF	0.00	0.93	0.03	67.17	0.00	0.99	0.00	51.29

Comparison of RT RV volumes (EDV, ESV, and SV) with catheter lab PV loop data provided strong statistical evidence ($p<<0.05$) for correlation between the two estimations, see Table 6. All CMR volumes were smaller than PV loop estimations as shown in the ‘Mean Difference’ column, RT minus PV loop.

Table 6 Correlation and mean difference (RT minus PV loop) for PV loop estimations of RV volumes compared with MRI measurements at rest (Clinical Cine, RT) and during exercise (RT only). P values: * = <0.05, ** = <0.01, *** = <0.001.

	Rest			Exercise		
	Correlation Coef.	p value	Mean Difference	Correlation Coef.	p value	Mean Difference
HR (BPM)	0.53	*	-5	0.54	0.13	-5
EDV (mL)	0.79	***	-78	0.88	**	-95
ESV (mL)	0.87	***	-28	0.93	***	-48
SV (mL)	0.48	*	-61	0.72	*	-65

Table 7 **Clinical and Invasive hemodynamic data**

	HFpEF, n=6	**PAH, n=5**	**Controls, n=9** *(1 subject via cath lab, 8 others via MRI)*	**p-value** (b/w HFpEF and PAH only)
Age, years	66.4±7.8	59.5±16.7	64	0.19
Female sex, n (%)	2 (33%)	4 (80%)	1	0.17
Weight (Kg)	91.9±16.3	81.6±20.8	78.8	0.18
Height (m)	1.76±0.09	1.64±0.10	1.64	0.04
BSA	2.11±0.21	1.92±0.29	1.83	0.12
BMI	30.9±4.5	29.9±6.4	33.9	0.39
Comorbidities				
- HTN	5 (83%)	3 (60%)	1	0.42
- DM	3 (50%)	1 (40%)	0	0.34

- Afib	3 (50%)	0	0	0.12
- CAD	3 (50%)	2 (40%)	0	0.50
- Sleep apnea	2 (33%)	1 (20%)	0	0.57
- Scleroderma	0	2 (40%)	0	-
- Chronic PE	0	2 (40%)	0	-
iCPET data				
mPAP – rest	32±12	33±8	18	0.43
mPAP – exercise	55±9	51±6	37	0.20
Cardiac Output – rest	5.07±1.34	4.68±1.25	6.03	0.32
Cardiac Output - exercise	8.78±4.00	9.14±3.60	12.6	0.39
Heart rate – rest	64±11	72±9	88	0.09
Heart rate – exercise	94±17	108±28	144	0.16
Stroke volume – rest	66.6±32.0	65.0±16.9	68.6	0.46
Stroke volume - exercise	87.4±29.3	85.7±28.4	87.5	0.21
mPAP/CO slope	6.7±4.1	5.1±3.3	2.8	0.10
Maximum workload (Watts)	69±35	67±35	125	0.46
Peak VO_2 (mL/Kg/min)	9.1±3.0	8.9±1.5	14.3	0.80
Right ventricular Pressure-Volume Loop data				
EDV - rest	110.4±39.0	124.8±63.3	135.0	0.33

EDV – exercise	155.7±42.5	143.6±71.4	143.8	0.37
ESV – rest	44.7±17.7	63.3±50.8	52.1	0.21
ESV - exercise	87.0±29.1	79.9±60.2	44.6	0.40
RVEF – rest	59.8±6.8	52.7±12.9	61.4	0.14
RVEF – exercise	44.8±5.8	46.8±13.4	69.0	0.37
Ees:Ea – rest	1.14±0.41	0.58±0.22	1.17	0.01
Ees:Ea – exercise	0.63±0.24	0.60±0.16	1.25	0.41

ABBREVIATIONS: HFpEF: heart failure with preserved ejection fraction, PAH: pulmonary arterial hypertension, BSA: body surface area, BMI: body mass index, HTN: hypertension, DM: diabetes, Afib: atrial fibrillation, CAD: coronary artery disease, PE: pulmonary embolism, mPAP: mean pulmonary artery pressure, CO: cardiac output, VO_2: oxygen consumption, EDV: end-diastolic volume, ESV: end-systolic volume, RVEF: right ventricular ejection fraction, Ees:Ea: end-systolic to arterial elastance ratio

6.4 **Discussion**

Clinical cine CMR at rest is well established as the gold standard for ventricle volume measurement and has a developing role in HFpEF and PH evaluation. Published literature on HFpEF and PAH exercise cardiac mechanics is limited but suggests that functional exercise is desired as a key method for uncovering underlying symptoms of HFpEF. Exercise is challenging to combine with traditional CMR - this study sought to investigate the value of free breathing real-time CMR volume measurement during exercise. Our work provides evidence that exercise stress CMR to evaluate ventricle volume changes with exercise correlates well with clinical cine volumes and is repeatable at rest, increasing confidence in the method.

Previous work at rest in the LV reported automatic respiratory and cardiac gating from LV segmentation using a low pass filter, but this approach fails at higher respiratory rates.[146] This study used a manually drawn synthetic navigator to successfully sort images by respiratory phase, allowing segmentation of expiratory SA slices. Automatic segmentation of the left ventricle using Otsu's method was sufficient to estimate RR intervals, correlating significantly with ECG measures at rest and allowing estimation of HR more reliably than ECG during exercise.

Previous work suggests that SV and EF should increase with exercise in the healthy heart.[72] This study measured statistical evidence for the increase of SV with exercise in healthy controls, while suggesting an inability to augment SV in HFpEF/PAH. Correlation of HFpEF SV with HR was not statistically significant but both RVSV and LVSV had negative relationship with HR. HFpEF is primarily a disease of left heart dysfunction which can lead to more serious right heart problems if left untreated; the decreasing RV SV trend may indicate our HFpEF patients already suffer from right heart involvement. In contrast, PAH patients had a positive relationship in LVSV but negative RVSV with HR. These results are also not statistically significant but agree with the current beliefs that PAH mainly affects the right heart, leaving the left heart unaffected. We recorded a slight increasing trend but did not find statistical evidence for an increase in EF with exercise, but EF is known to be the parameter with largest uncertainty due to error propagation and may not be a reliable metric to assess exercise related changes with MRI.

Healthy subject repeatability during exercise was statistically significant only for the EDVs. The large variability in repeated exercise is likely due to bulk motion due to exhaustion from the first round of exercise (increments of 50W to a max of 150-250W) which took 25-50 mins. Subjects breathed more rapidly and moved their torsos more after resting and then repeating the 100W exercise level . This analysis suffered from low n=6 and warrants further study.

Strong statistical evidence was found for a correlation between MR and PV loop RV volumes at rest and during exercise, but MR volumes were much smaller on average. This bias is likely due to both PV loop overestimations of volume and underestimation of true CMR volumes due to slice limits in segmentation. PV loop volumes are based on volume conductance estimations. The slice limits used during segmentation of the SA images were important to improving consistency across imaging methods, but defining the most basal slice as that which does not have visible outflow tract in any phase results in some ventricle volume near the outflow tract not being segmented, resulting in an underestimation of the 'true' ventricle volume.

Study Limitations

As the heartbeat increases with exercise, the number of real-time images captured per RR interval decreases. The exact moments of systole and diastole thus may be blurred with adjacent frames, leading to underestimation of EDV or overestimation of ESV. End-expiration rarely coincides exactly with ED or ES at rest, a problem that only worsens with rapid breathing caused during exercise. This misalignment is likely small but may contribute to error. Furthermore, patient LV papillary muscles were much larger than healthy controls and became impossible to distinguish from the ventricle wall in both cine and RT SA images. As a result, LVES volume was smaller than if papillary muscles had been included in segmentation, leading to an unrealistically high EF (Figure 22). Therefore, these ventricle values should only be compared with others measured in the same way or analyzed in terms of trends instead of absolute volume.

Cine reconstructions during exercise are challenging due to poor gating quality caused by the magnetohydrodynamic effect[147] or loose leads distorting the ECG trace. Gating metrics derived from a high temporal resolution reconstruction as described here could allow higher

quality cine reconstructions. Such reconstructions would likely struggle in the presence of irregular RR interval and rapid breathing.

Comparison between cardiovascular metrics measured in a supine position and a semi-recumbent position may not fully account for some physiological variations due to the changes in circulatory pressure and muscle activation.[148] Furthermore, fully supine exercise may not be possible if the patient suffers from orthopnea.

Patients in this study exhibited a limited heart rate increase in response to exercise – further study is needed to determine optimal workloads that allow exercise protocol completion while elevating heart rate sufficiently for diagnosis.

6.5 **Conclusion**

In this study, we presented preliminary RT CMR exercise imaging data from HFpEF patients and healthy controls during submaximal exercise. Heart volumes were measurable during exercise in healthy controls as well as HFpEF/PAH patients and correlated significantly with invasively measured PV loop data. While sample size is modest, an increase in left and right ventricle SV with exercise appears to exist in healthy controls. In contrast, a decrease in SV with exercise (HFpEF: both LVSV and RVSV, PAH: RVSV only) may exist in PAH and HFpEF patients.

6.6 **Acknowledgments:**

The University of Wisconsin-Madison receives research support from GE Healthcare. This study was supported by the UW-Madison Department of Medicine pilot fund (233-AAH9756) and the UW-Madison Department of Radiology Research and Development fund.

Figures and Tables

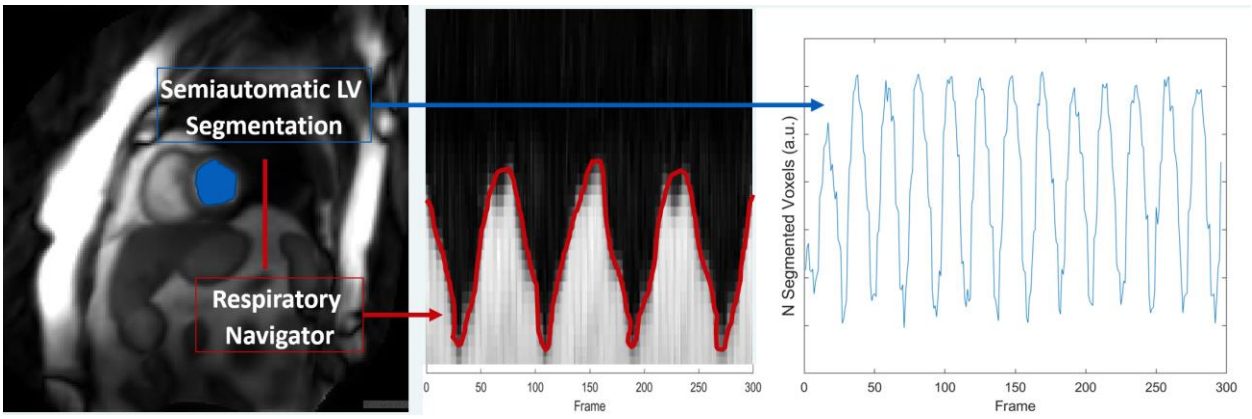

Figure 20: Extraction of respiratory and cardiac motion from the images: an image stack cropped around the LV was automatically segmented using Otsu's method (blue) and tracked over 300 frames (29 ms per frame). Peaks are detected and used to calculate RR intervals. A synthetic navigator was also drawn from the lung into the diaphragm (red), and edge detection applied through time to extract respiratory motion.

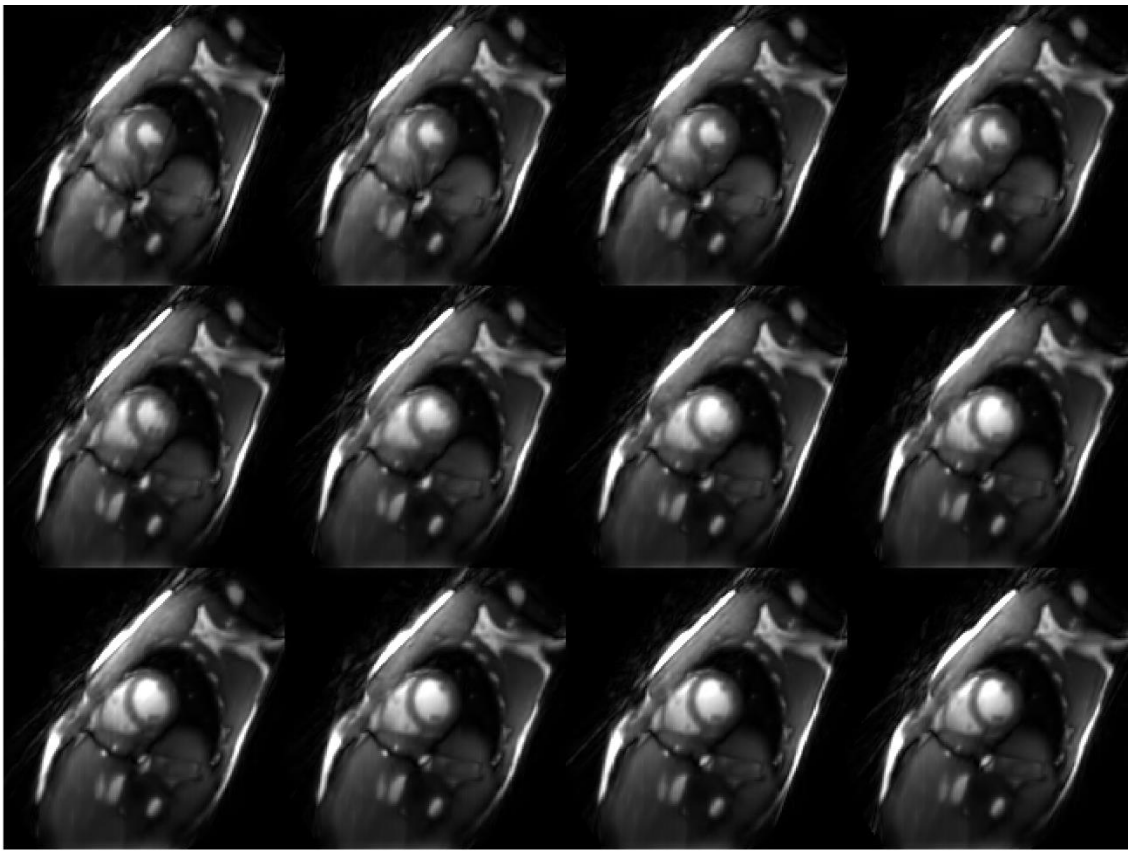

Figure 21: A representative radial acquisition real-time reconstruction central slice series from end systole to end diastole in Ctrl #2 during exercise. HR = 77 BPM, Δt = 29ms.

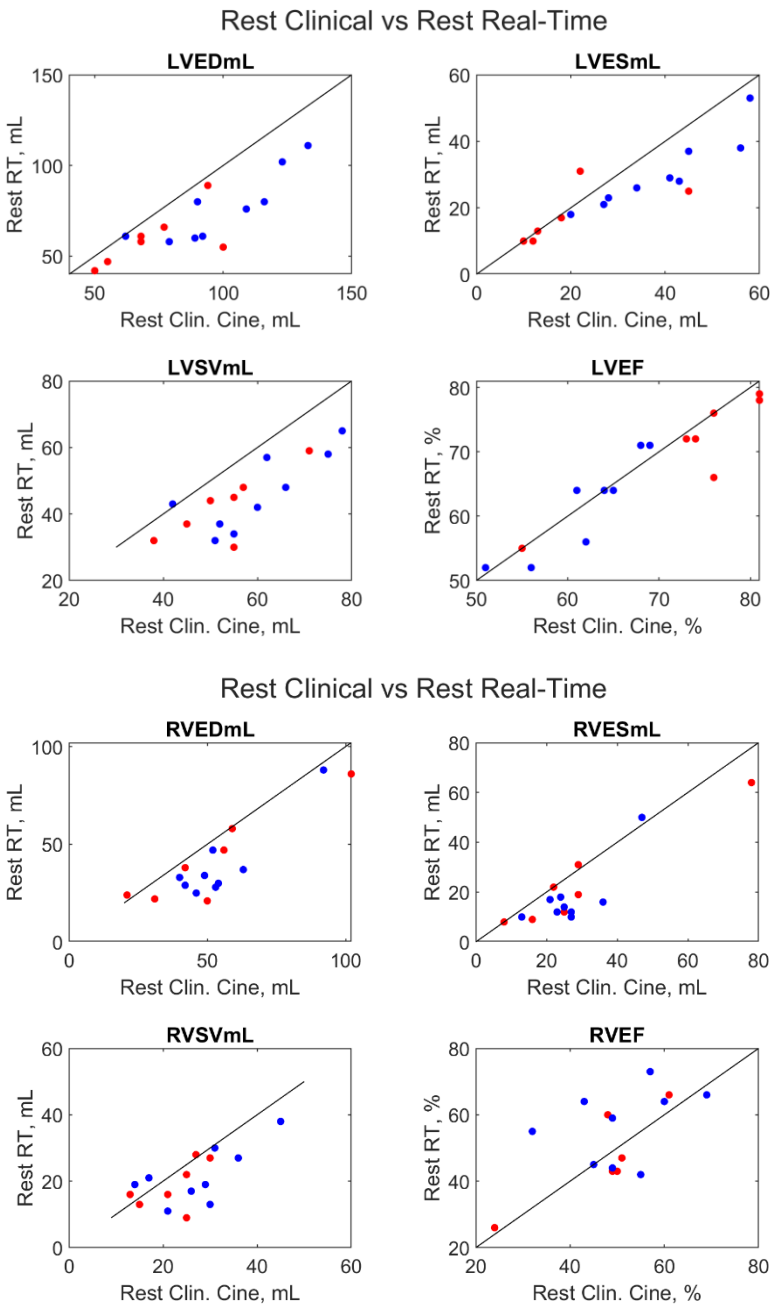

Figure 22 Correlation of rest real-time metrics with the rest clinical gold standard scan. Correlation was statistically significant for all metrics ($p<0.05$). Blue circles represent healthy controls, while red are clinical patients (PAH and HFpEF).

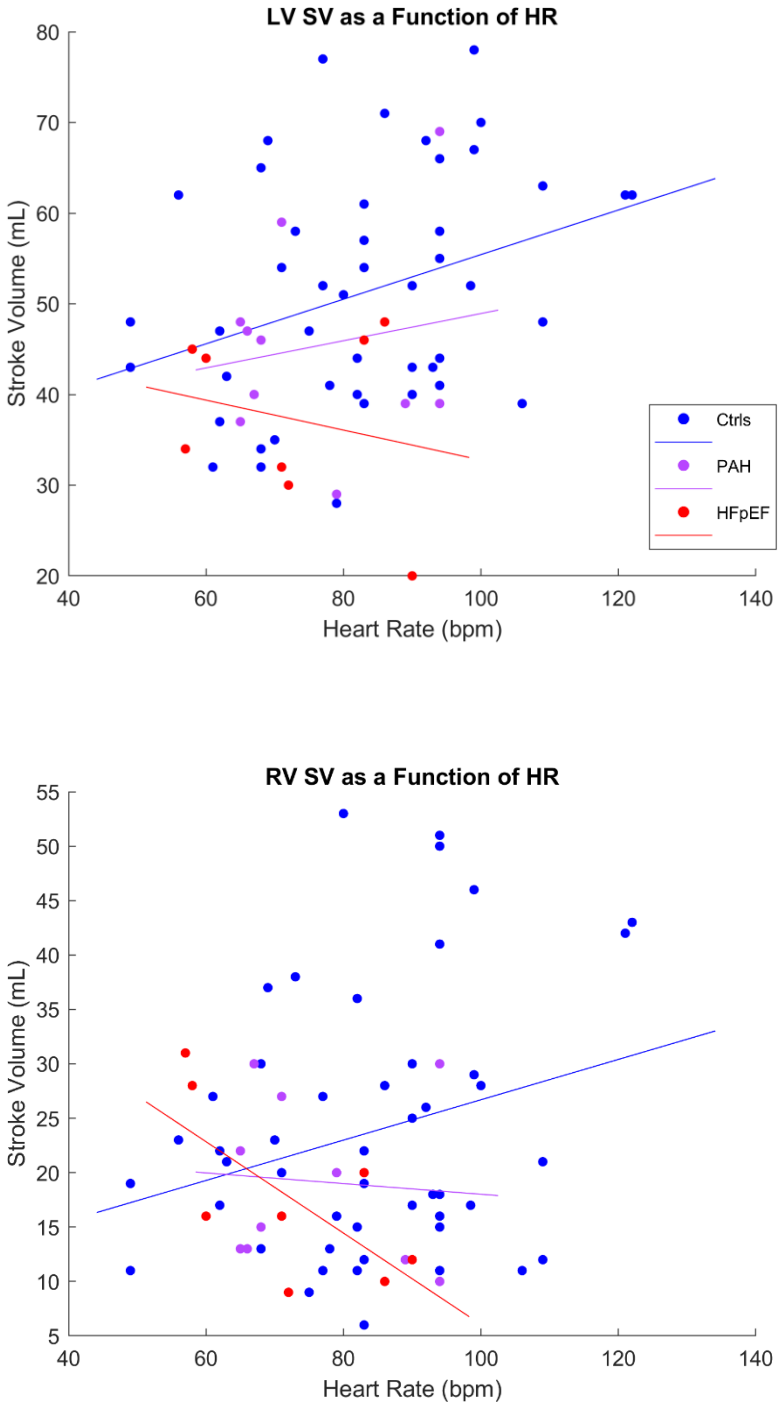

Figure 23 A) Statistical evidence for an increase in LV SV with HR in controls ($p<0.05$). A similar trend is not seen in the HFpEF or PAH group. B) Control RV LV may increase with HR, while the HFpEF or PAH group may decrease with HR, but p value was not significant.

Chapter 7: Summary

MRI has been established as a powerful diagnostic tool for noninvasively capturing disease-related changes in organ system form and function, but there are a variety of unexplored applications where technique development could result in a marked improvement on clinical standard of care. The work completed includes image acquisition, reconstruction, and post processing techniques. Specific advancements include:

- A method for placenta evaluation using ferumoxytol DCE perfusion imaging was applied to a Rhesus Macaque model of pregnancy exposed to zika virus. The dynamic contrast-enhanced MRI post processing technique described showed value in segmenting the fundamental units of placental organization, called cotyledons, as well as estimating their blood flow and volume. Comparisons with placental pathology from after delivery resulted in evidence for the technique's use in detecting virus-related changes early in pregnancy. Kai Ludwig developed the first implementation of the tool at UW, modeled after an approach developed for Gadolinium-based bolus injection by the Oregon Health & Science University group [22] I implemented an alternative method for estimating arrival time map from sigmoid fit to a thresholding approach. Their flow fit method seemed to dramatically overestimate possible values; I also implemented and tested several new methods for estimation of flow to the perfusion domains from the DCE data, choosing a linear fit of enhanced volume over time for its robustness to noise and eliminating the need to locate the spiral artery from early enhancing voxels.
- VS ASL perfusion measurements were conducted in a large pregnant human subject cohort. The sequence, reconstruction pipeline, and analysis techniques

described successfully quantified placental perfusion in a large cohort of normal and high BMI subjects. While the number of adverse outcomes in our subject pool of 97 singleton pregnancies was limited, we present evidence for an increase in placental perfusion with BMI. The novel heterogeneity analysis presented appears to detect obesity related changes. Kai Ludwig created the early version of the VS-ASL reconstruction at the UW for a human pilot study;[149] I corrected the quantification and reconstructed and analyzed all data in the human cohort study. I also developed and applied the workflow for data post processing and quantification, including the heterogeneity plots.

- Blood flow, velocity, and advanced hemodynamic parameters were assessed in a novel swine model designed to induce severe pulmonary hypertension while preserving the left heart. 4D Flow data were analyzed and visualized to assess the affected vessels and severity of the banding procedure. In addition, bi-ventricular flow compartments analysis was conducted and enhanced using registration of clinical cine SA images with 4D flow data for a better segmentation of the ventricular chambers than from 4D flow data alone. I reconstructed and analyzed all data using custom scripts, adopting a workflow that was initially implemented at UW by Phil Corrado. [115]
- A high temporal resolution imaging technique for CMR using radial sampling, parallel imaging, and compressed sensing was implemented and tested. Retrospective reconstruction allowed prioritization of image quality and temporal resolution: reconstructing with just 10 radial spokes per time frame was feasible and still allowed adequate segmentation of the ventricular volumes. This work

included testing the viability of a RT cardiac acquisition during exercise, implementing a compressed sensing [67] reconstruction pipeline using the Berkely Advanced Reconstruction Toolbox (BART) [141], and development of a workflow to automatically extract physiological gating data directly from the images. Phil Corrado had implemented a basic framework for radial cardiac acquisition and reconstruction. I developed and optimized the currently used workflow by extending the reconstruction code and adding custom algorithms to extract cardiac and respiratory motion directly from the images for segmentation, a crucial component for the proper sorting and analysis of free breathing, ungated acquisitions.

- The above real time CMR technique was used for a human study to enable the quantification of ventricle volumes in HFpEF/PH subjects and controls during exercise at varying work loads. Healthy controls were able to augment stroke volume with exercise, while HFpEF/PAH patients may have to rely on heart rate increase to achieve the necessary increase in cardiac output. I designed the study for the controls with the help of Farhan Raza and Oliver Wieben, applying the acquisition/reconstruction/post processing pipeline developed to the exercise steps accomplished and conducted all analysis.

7.1 **Innovations of this Work**

Notable innovations of this work include:

- This is the first published evidence of Ferumoxytol DCE MRI's value to detect placental pathology using automatic segmentation of functional domains. Previous work used contrast agents with gadolinium chelates, which is unlikely to ever be used in a clinical population since it can cross the placenta with unknown effects on the fetus. Meanwhile. Ferumoxytol, an iron-based contrast agent, is clinically approved to treat anemia during pregnancy and is currently used at some sites, including the UW, for MRI studies of the mother that are clinically required during pregnancy.
- We are the first to use Fe DCE to validate the number of perfusion domains against the number of cotyledons at delivery. This comparison gives us confidence in another novel result – the possible increasing trend in number of perfusion domains with gestation. This is the first noninvasive longitudinal assessment of possible cotyledon growth and development during gestation.
- The novel VS-ASL pulse sequence was used to obtain perfusion data in one of the largest published patient cohorts undergoing ASL imaging to date. This acquisition allowed novel placental heterogeneity analysis that has significant advantages over other published methods, including whole placenta coverage and ease of prescription.
- To our knowledge, this is the first measurements of flow in a swine model of pulmonary hypertension with banding. While LV direct flow has previously been reported in a swine stress model, [117] we report the first RV flow compartment analysis in a PH model.
- A unique 'real-time' acquisition, reconstruction, and post-processing workflow was developed to allow ventricle volume and function assessment during exercise in the bore of the MRI. The measured ventricular metrics correlate with the clinical gold standard in

both the left and right ventricle, and we found statistical evidence that real time metrics are repeatable at rest.

- Statistical evidence is shown for an increase in LVSV with HR in controls. A similar trend is shown in the control RV, but it is not significant. While the number of PAH and HFpEF data points is low, the SV in both ventricles seems to trend differently from controls. We report the first analysis of HFpEF and PAH stroke volume trends with HR as a metric of exercise intensity.

7.2 **Recommendations for Future Work**

The work presented in this dissertation provided evidence for the value of the techniques and their applications, but there were limitations that warrant further investigation.

Placental evaluation using Ferumoxytol DCE MRI may have great value in human pregnancy, but use of Fe as a contrast agent is currently an off-label procedure. Despite publications showing the safety of Ferumoxytol [79,80] and its use as an iron supplement already taken during pregnancy, it is unlikely to be approved in healthy subjects without extensive study. If clinical value outweighs perceived risks, however, use may be approved. Placental ferumoxytol DCE MRI in pregnant patients diagnosed with fetal growth restriction has been approved for a small study being conducted at UW-Madison. These scans do not use the bolus injection required for the tool developed and applied in this work out of additional caution. Instead, a slow infusion is administered in triage and not in the scanner. As a result, the dynamic changes required to segment cotyledons in the current work flow is not available. Until safety studies support the method's safety and value with dynamic imaging, T1 mapping and blood volume analysis as introduced by our group is a promising choice for analysis of the changes introduced by the

contrast and may allow estimation of structure and heterogeneity related to the arrangement of cotyledons.

Non-contrast options such as VS-ASL, on the other hand, are low risk and simple to prescribe from the scanner. While more expensive and time consuming than ultrasound, MRI offers a much broader range of metrics that can be recorded within a single scan session. The advantages of volumetric coverage and the potential to noninvasively probe the placenta's function with VS-ASL is promising. The availability of such 3D ASL data also enables more detailed analysis of the spatial organization beyond means and histograms and comparison of high flow zones with DCE MRI, which remains greatly unexplored to date. On the other hand, recent studies establish the dependence of VS-ASL on several acquisition parameters including the velocity sensitivity, encoding direction, and others .[106] Further work is needed to evaluate these factors and to develop protocols that generate consistent data across scanners. Such quantitative perfusion measurements also need to be validated against a "gold-standard" perfusion measurement technique such as xenon computed tomography [39], or [^{15}O]water positron emission tomography [110], likely only possible in animal models. Repeatability of the perfusion patterns analyzed and quantified using the heterogeneity analysis should also be tested by scanning the same subject multiple times. For placental MRI to find widespread clinical use, normative data must be obtained in multi-center studies and the clinical value of these measures must be prospectively established. Future clinical trials comparing prospectively acquired VS-ASL perfusion measures against clinical outcomes should be conducted to this end.

Pulmonary hypertension is a challenging disease to study since it is usually detected late in development and its causes and paths of development are uncertain. A swine model offers a compelling and controlled way to longitudinally test methods for evaluation of PH during disease

development and study the underlying physiological changes and adptations. While 4D Flow MRI confirmed the surgical success and measured blood flow, velocity, and ventricle flow compartments, the number of swine was too small to establish statistical evidence for differences between the banded and sham animals. This study is ongoing, and the number of swine scanned will continue to increased in future work. The plane placement of 4D Flow MRI is subjective and may introduce variability into the measured data. An approach to automatically placing analysis cut planes in 4D Flow datasets may improve processing time and decrease variation. [150] While swine anatomy differs from humans, the network could be 'cross trained' on the existing data and tested on future scans, but that requires a decent sizes training pool of cases. Our group is fortunate to have fiber optic MR-compatible pressure wires, and future comparison of invasive 'ground truth' pressures acquired at the same time as the flow data could offer interesting insights into the dynamics of the disease development and the physiological states between data obtained during MRI and in the catheter lab could be better compared.

Exercise is an important part of HFpEF and PH diagnosis but challenging to implement in the bore of the MRI. The acquisition, reconstruction, and postprocessing pipeline developed in this work focused on ventricular volumes. End systolic/diastolic measures are rudimentary CMR measures by clinical standards, and the tools built should be extended by

1) Principle component analysis (PCA) shows promise for respiratory motion extraction from real time rest images and could remove the need for manual 'synthetic navigator' placement. These methods may also offer automated extraction of cardiac signal but have not been thoroughly tested. [151,152]

2) Improving the post processing by training or adapting a neural network to automatically segment the ventricles. Even if the segmentation was not perfect, a starting estimation would allow the viewer to tweak the results and complete analysis more quickly.[153]
3) Explore dynamics of the cardiac cycle by segmenting the ventricles through time. This is currently very time consuming but would be a potentially valuable tool to study the cardiac changes at all time points acquired. Unfortunately, the current acquisition acquires a set number of projections before progressing to the next slice, so the heart rate may change between the base and apex. A method to estimate ventricle volume from fewer slices could be investigated.
4) Imaging at lower field strengths would result in fewer field inhomogeneities, thereby producing fewer bSSFP banding artifacts. It also offer opportunities for longer readouts, thereby further increasing the efficiency of the acquisition and possibly the frame rate and/or image quality.
5) The compressed sensing reconstruction was time consuming, and the regularization terms were qualitatively chosen. Automatic determination of the regularization weighting for wavelet- based compressed sensing MRI reconstructions may result in further improved image quality. [154]
6) Automated gating extraction such as PCA discussed above could be incorporated into the reconstruction pipeline: first using a high temporal resolution reconstruction for extracting self-gating parameters, then binning or motion correcting all data for use in cine reconstructions. The resulting images would be much higher quality, allowing segmentation of ventricles with less uncertainty.

7) Recent work demonstrates the value of a single long axis slice to obtain a crude measure of strain from ventricle shortening. The change in length of lines drawn from apex to the valve plane and then to the base of the atrium were recently presented as the best predictor of HFpEF. [127] Feature tracking directly from the bSSFP images has emerged as a compelling method to estimate strain since no additional scan time is needed. [155] However, feature tracking relies on good image quality to identify features in the images. High frame rate realtime MRI currently lacks the image quality and spatial resolution to support such analysis. Simpler estimations will be much easier to process and may offer valuable insight into disease etiology.

References

[1] Brown RW, Cheng YCN, Haacke EM, Thompson MR, Venkatesan R. Magnetic Resonance Imaging: Physical Principles and Sequence Design: Second Edition. Magnetic Resonance Imaging: Physical Principles and Sequence Design: Second Edition 2014; 9780471720850:1–944.

[2] Luypaert R, Boujraf S, Sourbron S, Osteaux M. Diffusion and perfusion MRI: basic physics. Eur J Radiol 2001; 38:19–27.

[3] Nayak KS, Nielsen JF, Bernstein MA, Markl M, Gatehouse PD, Botnar RM, Saloner D, Lorenz C, Wen H, Hu BS, Epstein FH, Oshinski JN, et al. Cardiovascular magnetic resonance phase contrast imaging. J Cardiovasc Magn Reson 2015; 17.

[4] Guttmacher AE, Maddox YT, Spong CY. The Human Placenta Project: Placental structure, development, and function in real time. Placenta 2014; 35:303–304.

[5] Guttmacher AE, Spong CY. The human placenta project: it's time for real time. Am J Obstet Gynecol 2015; 213:S3–S5.

[6] Gagnon R. Placental insufficiency and its consequences. Eur J Obstet Gynecol Reprod Biol 2003; 110 Suppl 1.

[7] Lang U, Baker RS, Braems G, Zygmunt M, Künzel W, Clark KE. Uterine blood flow--a determinant of fetal growth. Eur J Obstet Gynecol Reprod Biol 2003; 110 Suppl 1.

[8] Brosens I, Pijnenborg R, Vercruysse L, Romero R. The 'great Obstetrical Syndromes' are associated with disorders of deep placentation. American Journal of Obstetrics and Gynecology, vol. 204. Am J Obstet Gynecol; 2011:193–201.

[9] BEWLEY S, COOPER D, CAMPBELL S. Doppler investigation of uteroplacental blood flow resistance in the second trimester: a screening study for pre-eclampsia and intrauterine growth retardation. Br J Obstet Gynaecol 1991; 98:871–879.

[10] Goldenberg RL, Culhane JF, Iams JD, Romero R. Epidemiology and causes of preterm birth. Lancet 2008; 371:75–84.

[11] Habara T, Nakatsuka M, Konishi H, Asagiri K, Noguchi S, Kudo T. Elevated blood flow resistance in uterine arteries of women with unexplained recurrent pregnancy loss. Hum Reprod 2002; 17:190–194.

[12] NEWNHAM JP, O'DEA MR, REID KP, DIEPEVEEN DA. Doppler flow velocity waveform analysis in high risk pregnancies: a randomized controlled trial. BJOG 1991; 98:956–963.

[13] Kofinas AD, Penry M, Nelson LH, Meis PJ, Swain M. Uterine and umbilical artery flow velocity waveform analysis in pregnancies complicated by chronic hypertension or preeclampsia. South Med J 1990; 83:150–155.

[14] Fadl S, Moshiri M, Fligner CL, Katz DS, Dighe M. Placental imaging: Normal appearance with review of pathologic findings1. Radiographics 2017; 37:979–998.

[15] Hashem LB, Salem DS, Hamed ST, Hussein AM. Role of MRI versus ultras ound in the assessment of placental abnormalities and diseases. Egyptian Journal of Radiology and Nuclear Medicine 2016; 47:641–658.

[16] Vázquez-Boland JA, Krypotou E, Scortti M. Listeria Placental Infection. MBio 2017; 8.

[17] Tabata T, Petitt M, Fang-Hoover J, Zydek M, Pereira L. Persistent Cytomegalovirus Infection in Amniotic Membranes of the Human Placenta. Am J Pathol 2016; 186:2970–2986.

[18] McDonagh S, Maidji E, Ma W, Chang HT, Fisher S, Pereira L. Viral and bacterial pathogens at the maternal-fetal interface. J Infect Dis 2004; 190:826–834.

[19] Hirsch AJ, Roberts VHJ, Grigsby PL, Haese N, Schabel MC, Wang X, Lo JO, Liu Z, Kroenke CD, Smith JL, Kelleher M, Broeckel R, et al. Zika virus infection in pregnant rhesus macaques causes placental dysfunction and immunopathology n.d.

[20] Millischer AE, Deloison B, Silvera S, Ville Y, Boddaert N, Balvay D, Siauve N, Cuenod CA, Ttsatsaris V, Sentilhes L, Salomon LJ. Dynamic contrast enhanced MRI of the placenta: A tool for prenatal diagnosis of placenta accreta? Placenta 2017; 53:40–47.

[21] Deloison B, Arthuis C, Benchimol G, Balvay D, Bussieres L, Millischer A-EE, Grévent D, Butor C, Chalouhi G, Mahallati H, Hélénon O, Tavitian B, et al. Human placental perfusion measured using dynamic contrast enhancement MRI. PLoS One 2021; 16:e0256769.

[22] Frias AE, Schabel MC, Roberts VHJ, Tudorica A, Grigsby PL, Oh KY, Kroenke CD. Using dynamic contrast-enhanced MRI to quantitatively characterize maternal vascular organization in the primate placenta. Magn Reson Med 2015; 73:1570–1578.

[23] Chalouhi GE, Deloison B, Siauve N, Aimot S, Balvay D, Cuenod CA, Ville Y, Clément O, Salomon LJ. Dynamic contrast-enhanced magnetic resonance imaging: Definitive imaging of placental function? Semin Fetal Neonatal Med 2011; 16:22–28.

[24] Deloison B, Siauve N, Aimot S, Balvay D, Thiam R, Cuenod CA, Ville Y, Clement O, Salomon LJ. SPIO-enhanced magnetic resonance imaging study of placental perfusion in a rat model of intrauterine growth restriction. BJOG 2012; 119:626–633.

[25] Prola-Netto J, Woods M, Roberts VHJ, Sullivan EL, Miller CA, Frias AE, Oh KY. Gadolinium Chelate Safety in Pregnancy: Barely Detectable Gadolinium Levels in the Juvenile Nonhuman Primate after in Utero Exposure. Radiology 2018; 286:122–128.

[26] Rogosnitzky M, Branch S. Gadolinium-based contrast agent toxicity: a review of known and proposed mechanisms. BioMetals 2016; 29:365–376.

[27] Oh KY, Roberts VHJ, Schabel MC, Grove KL, Woods M, Frias AE. gadolinium chelate contrast Material in Pregnancy: Fetal Biodistribution in the Nonhuman Primate 1. RadiologyRsnaOrg n Radiology 2015; 276.

[28] Ray JG, Vermeulen MJ, Bharatha A, Montanera WJ, Park AL. Association Between MRI Exposure During Pregnancy and Fetal and Childhood Outcomes. JAMA 2016; 316:952–961.

[29] Siauve N, Chalouhi GE, Deloison B, Alison M, Clement O, Ville Y, Salomon LJ. Functional imaging of the human placenta with magnetic resonance. Am J Obstet Gynecol 2015; 213:S103–S114.

[30] Derwig I, Lythgoe DJ, Barker GJ, Poon L, Gowland P, Yeung R, Zelaya F, Nicolaides K. Association of placental perfusion, as assessed by magnetic resonance imaging and uterine artery Doppler ultrasound, and its relationship to pregnancy outcome. Placenta 2013; 34:885–891.

[31] Zun Z, Zaharchuk G, Andescavage NN, Donofrio MT, Limperopoulos C. Non-Invasive Placental Perfusion Imaging in Pregnancies Complicated by Fetal Heart Disease Using Velocity-Selective Arterial Spin Labeled MRI. Sci Rep 2017; 7.

[32] Hutter J, Harteveld AA, Jackson LH, Franklin S, Bos C, van Osch MJP, O'Muircheartaigh J, Ho A, Chappell L, Hajnal J V., Rutherford M, De Vita E. Perfusion and apparent oxygenation in the human placenta (PERFOX). Magn Reson Med 2020; 83:549–560.

[33] Liu D, Shao X, Danyalov A, Chanlaw T, Masamed R, Wang DJJ, Janzen C, Devaskar SU, Sung K. Human Placenta Blood Flow During Early Gestation With Pseudocontinuous Arterial Spin Labeling MRI. Journal of Magnetic Resonance Imaging 2019:jmri.26944.

[34] Duncan KR, Gowland P, Francis S, Moore R, Baker PN, Johnson IR. The investigation of placental relaxation and estimation of placental perfusion using echo-planar magnetic resonance imaging. Placenta 1998; 19:539–543.

[35] Gowland PA, Francis ST, Duncan KR, Freeman AJ, Issa B, Moore RJ, Bowtell RW, Baker PN, Johnson IR, Worthington BS. In vivo perfusion measurements in the human placenta using echo planar imaging at 0.5 T. Magn Reson Med 1998; 40:467–473.

[36] Shao X, Liu D, Martin T, Chanlaw T, Devaskar SU, Janzen C, Murphy AM, Margolis D, Sung K, Wang DJJ. Measuring human placental blood flow with multidelay 3D GRASE pseudocontinuous arterial spin labeling at 3T. Journal of Magnetic Resonance Imaging 2018; 47:1667–1676.

[37] Zun Z, Limperopoulos C. Placental perfusion imaging using velocity-selective arterial spin labeling. Magn Reson Med 2018; 80:1036–1047.

[38] Wong EC, Cronin M, Wu W-C, Inglis B, Frank LR, Liu TT. Velocity-selective arterial spin labeling. Magn Reson Med 2006; 55:1334–1341.

[39] Qiu D, Straka M, Zun Z, Bammer R, Moseley ME, Zaharchuk G. CBF measurements using multidelay pseudocontinuous and velocity-selective arterial spin labeling in patients with long arterial transit delays: Comparison with xenon CT CBF. Journal of Magnetic Resonance Imaging 2012; 36:110–119.

[40] Ludwig KD, Fain SB, Nguyen SM, Golos TG, Reeder SB, Bird IM, Shah DM, Wieben OE, Johnson KM. Perfusion of the placenta assessed using arterial spin labeling and ferumoxytol dynamic contrast enhanced magnetic resonance imaging in the rhesus macaque. Magn Reson Med 2019; 81:1964–1978.

[41] Zun Z, Hargreaves BA, Rosenberg J, Zaharchuk G. Improved multislice perfusion imaging with velocity-selective arterial spin labeling. Journal of Magnetic Resonance Imaging 2015; 41:1422–1431.

[42] Huis In 't Veld AE, De Man · F S, Van Rossum · A C, Handoko · M L. How to diagnose heart failure with preserved ejection fraction: the value of invasive stress testing 2016.

[43] Gladden JD, Linke WA, Redfield MM. Heart failure with preserved ejection fraction n.d.

[44] Oktay AA, Rich JD, Shah SJ. The Emerging Epidemic of Heart Failure with Preserved Ejection Fraction. Curr Heart Fail Rep 2013; 10:401–410.

[45] Borlaug BA, Nishimura RA, Sorajja P, Lam CSP, Redfield MM. Exercise hemodynamics enhance diagnosis of early heart failure with preserved ejection fraction. Circ Heart Fail 2010; 3:588–595.

[46] T Lau EM, Giannoulatou E, Celermajer DS, Humbert M. Epidemiology and treatment of pulmonary arterial hypertension. Nature Publishing Group 2017; 14.

[47] Humbert M, Kovacs G, Hoeper MM, Badagliacca R, Berger RMF, Brida M, Carlsen J, Coats AJS, Escribano-Subias P, Ferrari P, Ferreira DS, Ghofrani HA, et al. 2022 ESC/ERS Guidelines for the diagnosis and treatment of pulmonary hypertension. Eur Heart J 2022; 43:3618–3731.

[48] Broncano J, Bhalla S, Gutierrez FR, Vargas D, Williamson EE, Makan M, Luna A. Cardiac MRI in Pulmonary Hypertension: From Magnet to Bedside. Radiographics 2020; 40:982–1002.

[49] Badesch DB, Champion HC, Gomez Sanchez MA, Hoeper MM, Loyd JE, Manes A, McGoon M, Naeije R, Olschewski H, Oudiz RJ, Torbicki A. Diagnosis and assessment of pulmonary arterial hypertension. J Am Coll Cardiol 2009; 54.

[50] McGlothlin D. Classification of pulmonary hypertension. Heart Fail Clin 2012; 8:301–317.

[51] Tseng W-YI, Su M-YM, Tseng Y-HE. Introduction to Cardiovascular Magnetic Resonance: Technical Principles and Clinical Applications 1. BASIC PRINCIPLES OF MAGNETIC RESONANCE IMAGING (MRI) 1.1 Magnetic resonance n.d.

[52] Haddad F, Hunt SA, Rosenthal DN, Murphy DJ. Right Ventricular Function in Cardiovascular Disease, Part I. Circulation 2008; 117:1436–1448.

[53] Lotz J, Meier C, Leppert A, Galanski M. Cardiovascular flow measurement with phase-contrast MR imaging: Basic facts and implementation. Radiographics 2002; 22:651–671.

[54] Bluemke DA, Boxerman JL, Atalar E, Mcveigh ER, Morgan RH. Segmented K-Space Cine Breath-Hold Cardiovascular MR Imaging: Part 1. Principles and Technique n.d.

[55] Dyverfeldt P, Bissell M, Barker AJ, Bolger AF, Carlhäll CJ, Ebbers T, Francios CJ, Frydrychowicz A, Geiger J, Giese D, Hope MD, Kilner PJ, et al. 4D flow cardiovascular magnetic resonance consensus statement. Journal of Cardiovascular Magnetic Resonance 2015; 17:72.

[56] Markl M, Frydrychowicz A, Kozerke S, Hope M, Wieben O. 4D flow MRI. Journal of Magnetic Resonance Imaging 2012; 36:1015–1036.

[57] Fihn SD, Gardin JM, Abrams J, Berra K, Blankenship JC, Dallas AP, Douglas PS, Foody JM, Gerber TC, Hinderliter AL, King SB, Kligfield PD, et al. 2012 ACCF/AHA/ACP/AATS/PCNA/SCAI/STS guideline for the diagnosis and management of patients with stable ischemic heart disease: a report of the American College of Cardiology Foundation/American Heart Association task force on practice guidelines, and the American College of Physicians, American Association for Thoracic Surgery, Preventive Cardiovascular Nurses Association, Society for Cardiovascular Angiography and Interventions, and Society of Thoracic Surgeons. Circulation 2012; 126.

[58] Thadani U, West RO, Mathew TM, Parker JO. Hemodynamics at rest and during supine and sitting bicycle exercise in patients with coronary artery disease. Am J Cardiol 1977; 39:776–783.

[59] Proctor DN, Sinning WE, Bredle DL, Joyner MJ. Cardiovascular and peak VO2 responses to supine exercise: effects of age and training status. Med Sci Sports Exerc 1996; 28:892–899.

[60] Takata T, Yamabe H, Fukuzaki H. The hemodynamic and metabolic basis for decreased aerobic capacity in the supine exercise compared with the upright exercise in coronary artery disease. Jpn Circ J 1988; 52:495–502.

[61] Beaudry RI, Samuel TJ, Wang J, Tucker WJ, Haykowsky MJ, Nelson MD. Exercise cardiac magnetic resonance imaging: a feasibility study and meta-analysis. Am J Physiol Regul Integr Comp Physiol 2018; 315:R638–R645.

[62] Trankle CR, Canada JM, Jordan JH, Truong U, Hundley WG. Exercise Cardiovascular Magnetic Resonance: A Review. J Magn Reson Imaging 2022; 55:720–754.

[63] Roest AAW, Helbing WA, Kunz P, Van den Aardweg JG, Lamb HJ, Vliegen HW, Van der Wall EE, De Roos A. Exercise MR imaging in the assessment of pulmonary regurgitation and biventricular function in patients after tetralogy of fallot repair. Radiology 2002; 223:204–211.

[64] Roest AAW, De Roos A, Lamb HJ, Helbing WA, Van den Aardweg JG, Doornbos J, Van der Wall EE, Kunz P. Tetralogy of Fallot: postoperative delayed recovery of left ventricular stroke volume after physical exercise assessment with fast MR imaging. Radiology 2003; 226:278–284.

[65] Pruessmann KP, Weiger M, Scheidegger MB, Boesiger P. SENSE: Sensitivity encoding for fast MRI. Magn Reson Med 1999; 42:952–962.

[66] Uecker M, Lai P, Murphy MJ, Virtue P, Elad M, Pauly JM, Vasanawala SS, Lustig M. ESPIRiT - An eigenvalue approach to autocalibrating parallel MRI: Where SENSE meets GRAPPA. Magn Reson Med 2014; 71:990–1001.

[67] Lustig M, Donoho D, Pauly JM. Sparse MRI: The application of compressed sensing for rapid MR imaging. Magn Reson Med 2007; 58:1182–1195.

[68] Feng L, Axel L, Chandarana H, Block KT, Sodickson DK, Otazo R. XD-GRASP: Golden-Angle Radial MRI with Reconstruction of Extra Motion-State Dimensions Using Compressed Sensing. Magn Reson Med 2016; 75:775.

[69] Feng L, Grimm R, Block KT, Chandarana H, Kim S, Xu J, Axel L, Sodickson DK, Otazo R. Golden-Angle Radial Sparse Parallel MRI: Combination of Compressed Sensing, Parallel Imaging, and Golden-Angle Radial Sampling for Fast and Flexible Dynamic Volumetric MRI 2014.

[70] Usman M, Atkinson D, Odille F, Kolbitsch C, Vaillant G, Schaeffter T, Batchelor PG, Prieto C. Motion corrected compressed sensing for free-breathing dynamic cardiac MRI. Magn Reson Med 2013; 70:504–516.

[71] Wundrak S, Paul J, Ulrici J, Hell E, Geibel MA, Bernhardt P, Rottbauer W, Rasche V. Golden ratio sparse MRI using tiny golden angles. Magn Reson Med 2016; 75:2372–2378.

[72] Li YY, Zhang P, Rashid S, Cheng YJ, Li W, Schapiro W, Gliganic K, Yamashita AM, Grgas M, Haag E, Cao JJ. Real-time exercise stress cardiac MRI with Fourier-series reconstruction from golden-angle radial data. Magn Reson Imaging 2021; 75:89–99.

[73] Alexander BT. Placental insufficiency leads to development of hypertension in growth-restricted offspring. Hypertension 2003; 41:457–462.

[74] Krishna U, Bhalerao S. Placental insufficiency and fetal growth restriction. Journal of Obstetrics and Gynecology of India 2011; 61:505–511.

[75] Roberts DJ, Post MD. The placenta in pre-eclampsia and intrauterine growth restriction. J Clin Pathol 2008; 61:1254–1260.

[76] Naeye RL. Pregnancy hypertension, placental evidences of low uteroplacental blood flow, and spontaneous premature delivery. Hum Pathol 1989; 20:441–444.

[77] Fox H. The histopathology of placental insufficiency. J Clin Pathol 1976; 29:1–8.

[78] Roberts DJ. Placental pathology, a survival guide. Arch Pathol Lab Med 2008; 132:641–651.

[79] Ahmad F, Treanor L, Mcgrath TA, Walker D, Mcinnes MDF, Schieda N. Safety of Off-Label Use of Ferumoxtyol as a Contrast Agent for MRI: A Systematic Review and Meta-Analysis of Adverse Events 2020.

[80] Vasanawala SS, Nguyen KL, Hope MD, Bridges MD, Hope TA, Reeder SB, Bashir MR. Safety and technique of ferumoxytol administration for MRI. Magn Reson Med 2016; 75:2107–2111.

[81] Toth GB, Varallyay CG, Horvath A, Bashir MR, Choyke PL, Daldrup-Link HE, Dosa E, Finn JP, Gahramanov S, Harisinghani M, Macdougall I, Neuwelt A, et al. Current and potential imaging applications of ferumoxytol for magnetic resonance imaging. Kidney Int 2017; 92:47–66.

[82] Gerb J, Strauss W, Derman R, Short V, Mendelson B, Bahrain H, Auerbach M. Ferumoxytol for the treatment of iron deficiency and iron-deficiency anemia of pregnancy. Ther Adv Hematol 2021; 12.

[83] Nguyen SM, Wiepz GJ, Schotzko M, Simmons HA, Mejia A, Ludwig KD, Zhu A, Brunner K, Hernando D, Reeder SB, Wieben O, Johnson K, et al. Impact of ferumoxytol magnetic resonance imaging on the rhesus macaque maternal-fetal interface†. Biol Reprod 2020; 102:434–444.

[84] Macdonald JA, Corrado PA, Nguyen SM, Johnson KM, Francois CJ, Magness RR, Shah DM, Golos TG, Wieben O. Uteroplacental and Fetal 4D Flow MRI in the Pregnant Rhesus Macaque. Journal of Magnetic Resonance Imaging 2019; 49:534–545.

[85] Zhu A, Reeder SB, Johnson KM, Nguyen SM, Golos TG, Shimakawa A, Muehler MR, Francois CJ, Bird IM, Fain SB, Shah DM, Wieben O, et al. Evaluation of a Motion-Robust 2D Chemical Shift-Encoded Technique for R2* and Field Map Quantification in Ferumoxytol-Enhanced MRI of the Placenta in Pregnant Rhesus Macaques 2019.

[86] Zhu A, Reeder SB, Johnson KM, Nguyen SM, Fain SB, Bird IM, Golos TG, Wieben O, Shah DM, Hernando D. z. Magn Reson Imaging 2019.

[87] de Rijk EPCT, Van Esch E. The Macaque Placenta—A Mini-Review. Toxicol Pathol 2008; 36:108S-118S.

[88] Stouffer RL, Woodruff TK. Nonhuman primates: A vital model for basic and applied research on female reproduction, prenatal development, and women's health. ILAR J 2017; 58:281–294.

[89] Barry PA, Lockridge KM, Salamat S, Tinling SP, Yue Y, Zhou SS, Gospe SM, Britt WJ, Tarantal AF. Nonhuman primate models of intrauterine cytomegalovirus infection. ILAR J 2006; 47:49–64.

[90] Khong TY, Mooney EE, Ariel I, Balmus NCM, Boyd TK, Brundler MA, Derricott H, Evans MJ, Faye-Petersen OM, Gillan JE, Heazell AEP, Heller DS, et al. Sampling and definitions of placental lesions Amsterdam placental workshop group consensus statement. Archives of Pathology and Laboratory Medicine, vol. 140. College of American Pathologists; 2016:698–713.

[91] Schabel MC, Roberts VHJ, Lo JO, Platt S, Grant KA, Frias AE, Kroenke CD. Functional imaging of the nonhuman primate Placenta with endogenous blood oxygen level–dependent contrast. Magn Reson Med 2016; 76:1551–1562.

[92] Lo JO, Schabel MC, Roberts VHJ, Morgan TK, Fei SS, Gao L, Ray KG, Lewandowski KS, Newman NP, Bohn JA, Grant KA, Frias AE, et al. Effects of early daily alcohol exposure on placental function and fetal growth in a rhesus macaque model. Am J Obstet Gynecol 2021.

[93] Dimasuay KG, Boeuf P, Powell TL, Jansson T. Placental Responses to Changes in the Maternal Environment Determine Fetal Growth. Front Physiol 2016; 7.

[94] Roland MCP, Friis CM, Godang K, Bollerslev J, Haugen G, Henriksen T. Maternal factors associated with fetal growth and birthweight are independent determinants of placental weight and exhibit differential effects by fetal sex. PLoS One 2014; 9.

[95] Degner K, Magness RR, Shah DM. Establishment of the Human Uteroplacental Circulation: A Historical Perspective. Reproductive Sciences 2017; 24:753–761.

[96] Cnossen JS, Morris RK, Ter Riet G, Mol BWJ, Van Der Post JAM, Coomarasamy A, Zwinderman AH, Robson SC, Bindels PJE, Kleijnen J, Khan KS. Use of uterine artery Doppler ultrasonography to predict pre-eclampsia and intrauterine growth restriction: a

systematic review and bivariable meta-analysis. CMAJ : Canadian Medical Association Journal 2008; 178:701.

[97] Mourier E, Tarrade A, Duan J, Richard C, Bertholdt C, Beaumont M, Morel O, Chavatte-Palmer P. Non-invasive evaluation of placental blood flow: lessons from animal models. Reproduction 2017; 153:R85–R96.

[98] Francis ST, Duncan KR, Moore RJ, Baker PN, Johnson IR, Gowland PA. Non-invasive mapping of placental perfusion. Lancet 1998; 351:1397–1399.

[99] Mutsaerts MAQ, Groen H, Buiter-Van Der Meer A, Sijtsma A, Sauer PJJ, Land JA, Mol BW, Corpeleijn E, Hoek A. Effects of paternal and maternal lifestyle factors on pregnancy complications and perinatal outcome. A population-based birth-cohort study: the GECKO Drenthe cohort. Human Reproduction 2014; 29:824–834.

[100] Vinturache A, Moledina N, McDonald S, Slater D, Tough S. Pre-pregnancy Body Mass Index (BMI) and delivery outcomes in a Canadian population. BMC Pregnancy Childbirth 2014; 14.

[101] Catalano PM. Management of Obesity in Pregnancy. Obstetrics & Gynecology 2007; 109:419–433.

[102] Guo J, Meakin JA, Jezzard P, Wong EC. An optimized design to reduce eddy current sensitivity in velocity-selective arterial spin labeling using symmetric BIR-8 pulses. Magn Reson Med 2015; 73:1085–1094.

[103] Klein S, Staring M, Murphy K, Viergever MA, Pluim JPW. elastix: a toolbox for intensity-based medical image registration. IEEE Trans Med Imaging 2010; 29:196–205.

[104] Buxton RB, Frank LR, Wong EC, Siewert B, Warach S, Edelman RR. A general kinetic model for quantitative perfusion imaging with arterial spin labeling. Magn Reson Med 1998; 40:383–396.

[105] Schindelin J, Arganda-Carreras I, Frise E, Kaynig V, Longair M, Pietzsch T, Preibisch S, Rueden C, Saalfeld S, Schmid B, Tinevez JY, White DJ, et al. Fiji: an open-source platform for biological-image analysis. Nature Methods 2012 9:7 2012; 9:676–682.

[106] Harteveld AA, Hutter J, Franklin SL, Jackson LH, Rutherford M, Hajnal J V., Osch MJP, Bos C, De Vita E. Systematic evaluation of velocity-selective arterial spin labeling settings for placental perfusion measurement. Magn Reson Med 2020; 84:1828–1843.

[107] Hutter J, Slator PJ, Jackson L, Gomes ADS, Ho A, Story L, O'Muircheartaigh J, Teixeira RPAG, Chappell LC, Alexander DC, Rutherford MA, Hajnal J V. Multi-modal functional MRI to explore placental function over gestation. Magn Reson Med 2019; 81:1191–1204.

[108] Liu D, Xu F, Li W, van Zijl PC, Lin DD, Qin Q. Improved velocity-selective-inversion arterial spin labeling for cerebral blood flow mapping with 3D acquisition. Magn Reson Med 2020; 84:2512–2522.

[109] Janzen C, Lei MY, Lee BR, Vangala S, DelRosario I, Meng Q, Ritz B, Liu J, Jerrett M, Chanlaw T, Choi S, Aliabadi A, et al. American Journal of Perinatology A Description of the Imaging Innovations for Placental Assessment in Res-ponse to Environmental Pollution study (PARENTs) n.d.

[110] Fan AP, Jahanian H, Holdsworth SJ, Zaharchuk G. Comparison of cerebral blood flow measurement with [15O]-water positron emission tomography and arterial spin labeling

magnetic resonance imaging: A systematic review. J Cereb Blood Flow Metab 2016; 36:842–861.

[111] Pereda D, García-Alvarez A, Sánchez-Quintana D, Nuño M, Fernández-Friera L, Fernández-Jiménez R, García-Ruíz JM, Sandoval E, Aguero J, Castellá M, Hajjar RJ, Fuster V, et al. Swine model of chronic postcapillary pulmonary hypertension with right ventricular remodeling: Long-term characterization by cardiac catheterization, magnetic resonance, and pathology. J Cardiovasc Transl Res 2014; 7:494–506.

[112] Assad TR, Hemnes AR, Larkin EK, Glazer AM, Xu M, Wells QS, Farber-Eger EH, Sheng Q, Shyr Y, Harrell FE, Newman JH, Brittain EL. Clinical and Biological Insights Into Combined Post- and Pre-Capillary Pulmonary Hypertension. J Am Coll Cardiol 2016; 68:2525–2536.

[113] Vonk Noordegraaf A, Groeneveldt JA, Bogaard HJ. Pulmonary hypertension. Eur Respir Rev 2016; 25:4–11.

[114] Johnson KM, Lum DP, Turski PA, Block WF, Mistretta CA, Wieben O. Improved 3D phase contrast MRI with off-resonance corrected dual echo VIPR. Magn Reson Med 2008; 60:1329–1336.

[115] Corrado PA, Barton GP, Francois CJ, Wieben O, Goss KN. Sildenafil administration improves right ventricular function on 4D flow MRI in young adults born premature 2021.

[116] Eriksson J, Carlhäll CJ, Dyverfeldt P, Engvall J, Bolger AF, Ebbers T. Semi-automatic quantification of 4D left ventricular blood flow. Journal of Cardiovascular Magnetic Resonance 2010 12:1 2010; 12:1–10.

[117] Cesarovic N, Busch J, Lipiski M, Fuetterer M, Fleischmann T, Born S, von Deuster C, Sauer M, Maisano F, Kozerke S, Stoeck CT. Left ventricular blood flow patterns at rest and under dobutamine stress in healthy pigs. NMR Biomed 2019; 32.

[118] Hsu S, Houston BA, Tampakakis E, Bacher AC, Rhodes PS, Mathai SC, Damico RL, Kolb TM, Hummers LK, Shah AA, McMahan Z, Corona-Villalobos CP, et al. Right Ventricular Functional Reserve in Pulmonary Arterial Hypertension. Circulation 2016; 133:2413–2422.

[119] Borlaug BA, Olson TP, Lam CSP, Flood KS, Lerman A, Johnson BD, Redfield MM. Global cardiovascular reserve dysfunction in heart failure with preserved ejection fraction. J Am Coll Cardiol 2010; 56:845–854.

[120] Dunlay SM, Roger VL, Redfield MM. Epidemiology of heart failure with preserved ejection fraction. Nat Rev Cardiol 2017; 14:591–602.

[121] Lam CSP, Ho JE. Do we need dedicated heart failure with preserved ejection fraction clinics? n.d.

[122] Gorter TM, van Veldhuisen DJ, Bauersachs J, Borlaug BA, Celutkiene J, Coats AJS, Crespo-Leiro MG, Guazzi M, Harjola VP, Heymans S, Hill L, Lainscak M, et al. Right heart dysfunction and failure in heart failure with preserved ejection fraction: mechanisms and management. Position statement on behalf of the Heart Failure Association of the European Society of Cardiology. Eur J Heart Fail 2018; 20:16–37.

[123] Obokata M, Kane GC, Reddy YNV, Olson TP, Melenovsky V, Borlaug BA. Role of Diastolic Stress Testing in the Evaluation for Heart Failure With Preserved Ejection Fraction: A Simultaneous Invasive-Echocardiographic Study. Circulation 2017; 135:825–838.

[124] Solomon CG, Redfield MM. Clinical Practice Heart Failure with Preserved Ejection Fraction. The New England Journal of Medicine Downloaded from NejmOrg at UW-Madison 2016; 375:1868–77.

[125] Raza F, Dharmavaram N, Hess T, Dhingra R, Runo J, Chybowski A, Kozitza C, Batra S, Horn EM, Chesler N, Eldridge M. Distinguishing exercise intolerance in early-stage pulmonary hypertension with invasive exercise hemodynamics: Rest VE /VCO2 and ETCO2 identify pulmonary vascular disease. Clin Cardiol 2022; 45:742–751.

[126] Bogaert J (Jan). Clinical cardiac MRI 2012:709.

[127] Backhaus SJ, Lange T, George EF, Hellenkamp K, Gertz RJ, Billing M, Wachter R, Steinmetz M, Kutty S, Raaz U, Lotz J, Friede T, et al. Exercise Stress Real-Time Cardiac Magnetic Resonance Imaging for Noninvasive Characterization of Heart Failure With Preserved Ejection Fraction: The HFpEF-Stress Trial. Circulation 2021; 143:1484–1498.

[128] Vonk Noordegraaf A, Westerhof BE, Westerhof N. The Relationship Between the Right Ventricle and its Load in Pulmonary Hypertension. J Am Coll Cardiol 2017; 69:236–243.

[129] Pandey A, Shah SJ, Butler J, Kellogg DL, Lewis GD, Forman DE, Mentz RJ, Borlaug BA, Simon MA, Chirinos JA, Fielding RA, Volpi E, et al. Exercise Intolerance in Older Adults with Heart Failure with Preserved Ejection Fraction: JACC State-of-the-art Review. J Am Coll Cardiol 2021; 78:1166.

[130] Voit D, Zhang S, Unterberg-Buchwald C, Sohns JM, Lotz J, Frahm J. Real-time cardiovascular magnetic resonance at 1.5 T using balanced SSFP and 40 ms resolution. Journal of Cardiovascular Magnetic Resonance 2013; 15.

[131] Beer M, Stamm H, MacHann W, Weng A, Goltz JP, Breunig F, Weidemann F, Hahn D, Köstler H. Free breathing cardiac real-time cine MR without ECG triggering. Int J Cardiol 2010; 145:380–382.

[132] Katoh M, Kühl HP, Spuentrup E, Lipke CSA, Günther RW, Buecker A. Reliable 5-min real-time MR technique for left-ventricular-wall motion analysis. Eur Radiol 2007; 17:1836–1841.

[133] Kühl HP, Spuentrup E, Wall A, Franke A, Schröder J, Heussen N, Hanrath P, Günther RW, Buecker A. Assessment of Myocardial Function with Interactive Non-Breath-hold Real-time MR Imaging: Comparison with Echocardiography and Breath-hold Cine MR Imaging. Radiology 2004; 231:198–207.

[134] Yamamuro M, Tadamura E, Kanao S, Okayama S, Okamoto J, Urayama S, Kimura T, Komeda M, Kita T, Togashi K. Cardiac functional analysis by free-breath real-time cine CMR with a spatiotemporal filtering method, TSENSE: Comparison with breath-hold cine CMR. Journal of Cardiovascular Magnetic Resonance 2006; 8:801–807.

[135] Wintersperger BJ, Nikolaou K, Dietrich O, Rieber J, Nittka M, Reiser MF, Schoenberg SO. Single breath-hold real-time cine MR imaging: Improved temporal resolution using generalized autocalibrating partially parallel acquisition (GRAPPA) algorithm. Eur Radiol 2003; 13:1931–1936.

[136] Francone M, Dymarkowski S, Kalantzi M, Bogaert J. Real-time cine MRI of ventricular motion: A novel approach to assess ventricular coupling. Journal of Magnetic Resonance Imaging 2005; 21:305–309.

[137] Beaudry RI, Samuel TJ, Wang J, Tucker WJ, Haykowsky MJ, Nelson MD. Exercise cardiac magnetic resonance imaging: A feasibility study and meta-analysis. Am J Physiol Regul Integr Comp Physiol 2018; 315:R638–R645.

[138] Kozitza CJ, Dharmavaram N, Tao R, Tabima DM, Chesler NC, Raza F. Pulmonary vascular distensibility with passive leg raise is comparable to exercise and predictive of clinical outcomes in pulmonary hypertension. Pulm Circ 2022; 12.

[139] Raza F, Kozitza C, Lechuga C, Seiter D, Corrado P, Merchant M, Dharmavaram N, Korcarz C, Eldridge M, Francois C, Wieben O, Chesler N. Multimodality Deep Phenotyping Methods to Assess Mechanisms of Poor Right Ventricular-Pulmonary Artery Coupling. FUNCTION 2022; 3.

[140] Bellofiore A, Vanderpool R, Brewis MJ, Peacock AJ, Chesler NC. A novel single-beat approach to assess right ventricular systolic function. J Appl Physiol 2018; 124:283–290.

[141] Ueker et. al. BART Toolbox. https://mrirecon.github.io/bart/. Accessed 17 December 2020.

[142] Otsu N. THRESHOLD SELECTION METHOD FROM GRAY-LEVEL HISTOGRAMS. IEEE Trans Syst Man Cybern 1979; SMC-9:62–66.

[143] Heiberg E, Sjögren J, Ugander M, Carlsson M, Engblom H, Arheden H. Design and validation of Segment-freely available software for cardiovascular image analysis 2010.

[144] Rueden CT, Schindelin J, Hiner MC, DeZonia BE, Walter AE, Arena ET, Eliceiri KW. ImageJ2: ImageJ for the next generation of scientific image data. BMC Bioinformatics 2017; 18:1–26.

[145] Le JN, Zhou R, Tao R, Dharmavaram N, Dhingra R, Runo J, Forfia P, Raza F. Recumbent Ergometer vs Treadmill Cardiopulmonary Exercise Test in HFpEF: Implications for Chronotropic Response and Exercise Capacity 2022.

[146] Wu Y, Wan Q, Zhao J, Liu X, Zheng H, Chung YC, Chen Y. Improved workflow for quantifying left ventricular function via cardiorespiratory-resolved analysis of free-breathing MR real-time cines. J Magn Reson Imaging 2017; 46:905–914.

[147] Abi-Abdallah D, Robin V, Drochon A, Fokapu O. Alterations in human ECG due to the MagnetoHydroDynamic effect: a method for accurate R peak detection in the presence of high MHD artifacts. Annu Int Conf IEEE Eng Med Biol Soc 2007; 2007:1842–1845.

[148] LE JN, ZHOU R, TAO RAN, DHARMAVARAM NAGA, DHINGRA RAVI, RUNO J, FORFIA PAUL, RAZA F. Recumbent Ergometer vs Treadmill Cardiopulmonary Exercise Test in HFpEF: Implications for Chronotropic Response and Exercise Capacity. J Card Fail 2023; 29:407–413.

[149] Ludwig KD, Adamson EB, Fain SB, Reeder SB, Bird IM, Wieben OE, Shah DM, Johnson KM. Comparison of FAIR and Velocity-Selective ASL Perfusion MRI in the Human Placenta. n.d.

[150] Corrado PA, Daniel ·, Seiter P, Wieben · Oliver. Automatic measurement plane placement for 4D Flow MRI of the great vessels using deep learning 2021.

[151] Chen C, Chandrasekaran P, Liu Y, Simonetti OP, Tong M, Ahmad R. Ensuring Respiratory Phase Consistency to Improve Cardiac Function Quantification in Real-Time CMR. Magn Reson Med 2022; 87:1595.

[152] Novillo F, Van Eyndhoven S, Moeyersons J, Bogaert J, Claessen G, La Gerche A, Van Huffel S, Claus P. Unsupervised respiratory signal extraction from ungated cardiac magnetic resonance imaging at rest and during exercise. Phys Med Biol 2019; 64.

[153] Bai W, Sinclair M, Tarroni G, Oktay O, Rajchl M, Vaillant G, Lee AM, Aung N, Lukaschuk E, Sanghvi MM, Zemrak F, Fung K, et al. Automated cardiovascular magnetic resonance image analysis with fully convolutional networks. ArXiv 2017; 20:65.

[154] Varela-Mattatall G, Baron CA, Menon RS. Automatic determination of the regularization weighting for wavelet-based compressed sensing MRI reconstructions. Magn Reson Med 2021; 86:1403–1419.

[155] Lin ACW, Seale H, Hamilton-Craig C, Morris NR, Strugnell W. Quantification of biventricular strain and assessment of ventriculo-ventricular interaction in pulmonary arterial hypertension using exercise cardiac magnetic resonance imaging and myocardial feature tracking. J Magn Reson Imaging 2019; 49:1427–1436.